

A CHARACTERIZATION OF THE IMPACT OF CLOUDS ON  
REMOTELY SENSED WATER QUALITY

by

Ronald R. Fairbanks

A dissertation submitted in partial fulfillment of the requirements  
for the degree of Ph.D. in the Chester F. Carlson Center for Imaging  
Science, College of Science, Rochester Institute of Technology

July 1999

Signature of Author \_\_\_\_\_

Accepted by \_\_\_\_\_  
Coordinator, Ph.D. Degree Program Date



CHESTER R. CARLSON  
CENTER FOR IMAGING SCIENCE  
COLLEGE OF SCIENCE  
ROCHESTER INSTITUTE OF TECHNOLOGY  
ROCHESTER, NEW YORK

**CERTIFICATE OF APPROVAL**

---

Ph. D. DEGREE DISSERTATION

---

The Ph.D. Degree Dissertation of Ronald R. Fairbanks  
has been examined and approved by the  
dissertation committee as satisfactory for the  
dissertation requirement for the  
Ph.D. degree in Imaging Science

---

Dr. John R. Schott, Thesis Advisor

---

Dr. Anthony Vodacek

---

Dr. Harvey Rhody

---

Dr. John Waud

---

Date



Date 25 July 1999

Rochester Institute of Technology

Abstract

A CHARACTERIZATION OF THE IMPACT OF  
CLOUDS ON REMOTELY SENSED WATER QUALITY

by Ronald R. Fairbanks

Atmospheric correction and subsequent chlorophyll detection algorithms via remote sensing means were designed for use over the world's oceans. The algorithms seem to fail when used on data taken over the Laurentian Great Lakes. Two primary reasons for the failure have been identified as higher suspended minerals in the Great Lakes than in the oceans and normally higher cloud cover over the Great Lakes. A characterization of the impact of clouds on the radiance reaching remote sensing platforms has been performed. From this characterization, the impact on the calculated chlorophyll content determined by current algorithms is derived. The work presented here describes the creation of an end-to-end radiative transfer model for the complete sun-air-water-air-detector system and the application of that model to perform the cloud impact characterization. The radiative transfer model is modular; the modules relate to each propagation/scattering regime. Existing radiative transfer computer codes were used when the required accuracy and resolution

could be met. The cloud module in particular represents an advance in the radiative transfer methods found in the literature.

## ACKNOWLEDGEMENTS

I wish to acknowledge the tremendous contributions that helped me complete this body of work. Specifically, Dr. John Schott is my principal advisor and the driving source behind the creation of both the end to end radiative transfer model and the cloud characterization. Both were his ideas and it was under his direction that the work took shape. Dr. Anthony Vodacek supplied many comments, goals, and advice for radiative transfer under water. Dr Vodacek also supplied the original Hydrolight 3.0 code that I started with. The rest of my dissertation committee, Dr. Harvey Rhody and Dr. John Waud, also supplied several meaningful comments and advice along the way.

Scott Brown supplied several MODTRAN tips and tricks and generously allowed me to bounce ideas and thoughts off of him before I implemented them. Capt Erich Hernandez-Baquero was a tremendous help in the code validation process. Erich always seemed to have the right question for me to attack and he helped exercise HydroMod in the early stages. 1Lt Niki Wilson and Mary Ellen Miller were also early participants and helped by asking challenging questions and probing for clarity and understanding.

It is safe to assert that I may not have finished this program had it not been for the efforts of Capt Charles Daly, Ph.D., in helping to prepare me for the comprehensive exams. Capt Daly went well above and beyond normal measures to tutor, lecture, and quiz me and I am in his debt.

I wish to thank Dr. Ian Gatley and the RIT Center for Imaging Science faculty for the excellent education and for allowing me to pursue the doctoral degree.

I wish to thank the United States Air Force for paying for the degree and generously allowing me the required time.

I also wish to thank Dr. Curtis Mobley for making Hydrolight 3.0 available for educational purposes.

The support and love from my wife, Tina, and my children, Alex and Joshua, were indispensable. The working weekends, long days, and many evenings take their toll. Families as loving and as strong as mine help each other survive and thrive and I am truly blessed.

**Dedicated to Tina, Alexandra, and Joshua**



# TABLE OF CONTENTS

<b>Table Of Contents</b> .....	ix
List Of Figures .....	xi
Glossary.....	xv
<b>Introduction</b> .....	1
<b>Defining The Problem</b> .....	9
GEOMETRY USED .....	14
RADIATION IN THE AIR.....	16
Sun Source Radiance .....	17
Sky Source Radiance.....	20
Radiance From Clouds.....	23
An Elegant And Simple Method .....	30
TRANSITION FROM AIR TO WATER.....	35
Some Anomalous Cases .....	45
UNDER WATER REFLECTION MODELS.....	51
What Is In The Water .....	55
TRANSITION FROM WATER TO AIR.....	65
PROPAGATION TO THE SENSOR.....	65
RADIATIVE TRANSFER MODEL SUMMARY .....	66
<b>SeaWiFS Derived Chlorophyll Content</b> .....	69
<b>SeaWiFS Cloud Study Scope</b> .....	79
<b>Results And Analysis</b> .....	87
Single Step-By-Step Analysis.....	87
Affect On The SeaWiFS Calculations .....	98
Cloud Location Affects .....	102
Introducing A Cloudbank .....	103
Cloud Density Level Impact .....	108
The Wind Speed Impact .....	111
The Impact With Respect To Water Quality .....	116
The Impact With Respect To Atmosphere Model.....	120
SM Or Clouds .....	125
Summary Of Results.....	128
Operational Impact Of Results .....	131
<b>CONCLUSIONS</b> .....	135
Summary Of Contributions .....	135
Recommendations .....	137
Appendix I .....	141
Appendix II.....	203
<b>Bibliography</b> .....	231



## LIST OF FIGURES

<i>Number</i>	<i>Page</i>
Figure 1: Apparent Reflectance As Measured By At Select Locations. ....	5
Figure 2: Light Pathways In The Atmosphere.....	11
Figure 3: Radiative Transfer Model Regimes.....	13
Figure 4: Angle Definitions For The Geometry Used. ....	15
Figure 5: Standard Polar View.....	16
Figure 6: Example Possible Output. ....	18
Figure 7 Exo-Atmospheric Solar Spectral Irradiance.....	21
Figure 8: Radiance To And From Clouds.....	25
Figure 9: Cloud Spectral Response Curves .....	32
Figure 10: Measured Cloud Spectral Data. ....	34
Figure 11: Geometry For A Wave Facet Defined By $\beta$ And $\zeta$ . ....	38
Figure 12: Geometry Of Reflection Off A Wave Facet. ....	40
Figure 13: Geometry Of Refraction Through A Wave Facet... ..	40
Figure 14: Refractive Index For Fresh Water .....	46
Figure 15: Facet-To-Facet Shadowing And Multiple Reflection. ....	48
Figure 16: Scattering Cross Sections.....	62
Figure 17: Absorption Cross Sections. ....	63
Figure 18: Absorption Coefficient For Water.. ....	64
Figure 19: Scattering Coefficient For Water. ....	64

Figure 20: Two Sample Empirical Relationships Scanned From Gordon (1994).....	71
Figure 21: Affect Of Changing The Reflectance Ratio On The Calculated Chlorophyll Content .....	77
Figure 22: Fresnel Reflection Coefficients At The Air/Water Interface.....	80
Figure 23: Two Quantized Spheres.....	84
Figure 24: Two Input Sky Radiance Data Sets. ....	88
Figure 25: The Direct Sun Radiance Term.....	89
Figure 26: Surface Reflected And Total Water Leaving Radiance.....	90
Figure 27: Two Nearly Identical Upwelled Radiance Data Sets.....	91
Figure 28: Total Sensor Reaching Radiance For The Clear Sky Case.....	92
Figure 29: Total Sensor Reaching Radiance For The Single Cloud Case .....	93
Figure 30: Error Caused By A Single Cloud In An Otherwise Clear Sky. ....	95
Figure 31: A 3-D View Of Figure 30 (D) .....	96
Figure 32: A Diameter Slice Through The Center Of Figure 30 (D).....	97
Figure 33: The Error In The Ratio Between $\rho_T(765)$ And $\rho_T(865)$ (A) And Between $\rho_W(490)$ And $\rho_W(555)$ (B) .....	100
Figure 34: Change In Peak Percent Error For Varying Cloud Brightness Levels....	101
Figure 35: Effect Of Changing The Cloud Declination Angle.....	102
Figure 36: Cloud Bank Input Sky Data.....	104
Figure 37: Percent Error For The Two Main Quality Parameters. ....	105
Figure 38: Peak Percent Error On The Chlorophyll. ....	106
Figure 39: Calculated Chlorophyll Levels .....	107

Figure 40: Calculated Chlorophyll Differences Between The Cloud Case And The No Cloud Case.....	108
Figure 41: Peak Error In The Sensor Reaching Reflectance Band 7/8 Ratio V.....	109
Figure 42: Peak Error In The Water Leaving Band 3/5 Ratio .....	110
Figure 43: Changes In The Chlorophyll Level For The Varying Cloud Brightness For Different Cloud Densities. ....	111
Figure 44: Changes In The Chlorophyll Level For The Varying Cloud Brightness For Different Cloud Densities. ....	112
Figure 45: Percent Error In Band 7/8 Ratio With Respect To Wind Speed For Different Brightness Factor Levels.....	113
Figure 46: Percent Error In The Band 3/5 Ratio As A Function Of Wind Speed At Different Cloud Brightness Factor Levels.....	114
Figure 47: Normalized Error Width Ratio.....	115
Figure 48: Calculated Chlorophyll Levels .....	116
Figure 49: Percent Error Both The Sensor Reaching Band 7/8 Ratio And The Water Leaving Band 3/5 Ratio For Pure Water, Semi-Clean Water, And More Turbid Water. ....	117
Figure 50: Calculated Chlorophyll Content For The Three Water Cases Used In Figure 49.....	119
Figure 51: Percent Error For The Band 7/8 Ratio (At The Sensor) And The Band 3/5 Ratio (At The Water Surface.).....	120

Figure 52: Calculated Chlorophyll Content Using The Original (A) And The New (B) SeaWiFS Algorithms. ....	121
Figure 53: The Sensor Reaching Band 7/8 Ratio Error And Water Leaving Band 3/5 Ratio Error.. ....	122
Figure 54: The Calculated Chlorophyll Content With Varying Atmospheres.....	124
Figure 55: SM And Cloud Changes At A Chlorophyll Level Of 1.0/L .....	124

## GLOSSARY

$\alpha$ .....	Spherical declination angle ranging from 0 to $\pi$ radians
$\beta$ .....	Wave facet slope which is equal to the declination angle of the normal to the wave facet
$\gamma$ .....	Spherical azimuthal angle ranging from 0 to $2\pi$ radians
$\zeta$ .....	Azimuthal angle from the wind speed direction, $\omega$ , to the direction of steepest slope, $\beta$ , for a wave facet. The angle is measured counter clockwise looking down on a “flat” water surface.
$\eta$ .....	
$\theta$ .....	Hemispherical declination angle normally ranging from 0 to $\pi/2$ radians; angles outside that range are handled as special cases
$^+\theta$ .....	Hemispherical declination angle above (+) the water’s surface ranging from 0 to $\pi/2$ radians measured from the +z axis
$^-\theta$ .....	Hemispherical declination angle below (-) the water’s surface ranging from 0 to $\pi/2$ radians measured from the -z axis
$\theta_i$ .....	A specific hemispherical declination angle. This variable could be superscripted with a + or – to indicate above or below the water surface. The subscript, i, may be replaced with a prime, ‘, in some cases to indicate specific $\theta$ ’s
$\theta_d$ .....	Specific declination angle between the pixel of interest and the detector
$\lambda$ .....	Wavelength. Subscripted $\lambda$ ’s indicate a particular wavelength
$^+v_i$ .....	Angle between a wave facet normal and an incoming or reflected radiance vector above the water surface
$^-v_i$ .....	Angle between a wave facet normal and a refracted radiance vector below the water surface
$\rho$ .....	Reflection coefficient which is a function of wave facet orientation, incoming radiance direction, wavelength, and index of refraction
$\sigma$ .....	Specific sun hemispherical declination angle
$\sigma_c$ .....	Cross Wind RMS slope component = $(0.003+0.00192W)^{1/2}$
$\sigma_u$ .....	Upwind RMS slope component = $0.056214W^{1/2}$
$\tau$ .....	Transmission coefficient equal to $1-\rho$ with zero absorption

$\phi$ .....	Hemispherical azimuthal angle ranging from 0 to $2\pi$ radians; may be subscripted ( $\phi_i$ ) or primed ( $\phi'$ ) to indicate specific azimuthal angles or superscripted with a + or – to indicate above or below the water surface or a combination.
$\phi_d$ .....	Specific azimuthal angle indicating the direction of the detector
$\phi_s$ .....	Specific azimuthal angle indicating the direction of the sun
$\omega$ .....	Azimuthal angle of the wind direction measured from due north positively west
$\varepsilon$ .....	Ratio between the single scattering aerosol reflectance at 765nm and the single scattering aerosol reflectance at 865nm; the ratio is assumed constant when an arbitrary $\lambda$ is substituted for 765nm
$\varepsilon_{Peak}$ .....	Peak of the error whether a minimum or a maximum
$\varepsilon_{WR}$ .....	Normalized Error Width Ratio defined by dividing the full solid angle with error values at or above half the maximum error value (analogous to a full width at half max parameter) by the solid angle of the cloud that caused the error.
CZCS .....	Coastal Zone Color Scanner
$E_{Sun}$ .....	Exoatmospheric Solar Irradiance
$+L_{\lambda}^{\downarrow}(\theta, \phi)$ .....	Radiance with a wavelength dependence above the water surface heading down as a function of the $\theta, \phi$ direction angles. The $\theta, \phi$ angles may be subscripted to indicated a specific direction for a specific vector radiance.
$+L_{\lambda}^{\uparrow}(\theta_d, \phi_d)$ .....	Radiance with a wavelength dependence above the water surface heading up in the specific $\theta_d, \phi_d$ direction. An absence of the “d” subscript would indicate that the radiance is a function of the $\theta, \phi$ direction angles.
$-L_{\lambda}^{\downarrow}(\theta, \phi)$ .....	Radiance with a wavelength dependence below the water surface heading down as a function of the $\theta, \phi$ direction angles. The $\theta, \phi$ angles may be subscripted to indicated a specific direction for a specific vector radiance.
$-L_{\lambda}^{\uparrow}(\theta, \phi)$ .....	Radiance with a wavelength dependence below the water surface heading up as a function of the $\theta, \phi$ direction angles. The $\theta, \phi$ angles may be subscripted to indicated a specific direction for a specific vector radiance.
$n$ .....	Index of refraction usually subscripted to indicate which medium it relates to ( $n_{water}$ or $n_{air}$ or $n_1 \dots$ )



$p(\beta, \zeta)$  ..... Probability Density Function for a wave facet with slope  $\beta$  in the  $\zeta$  direction  
 $R(a, b; c, d)$  .... Bi-directional Reflectance Factor from (a, b) direction to (c, d) direction  
 SeaWiFS ..... Sea Viewing Wide Field-of-view Sensor  
 $W$  ..... Wind Speed



## *Chapter 1*

### **INTRODUCTION**

The importance of the world's oceans combined with their vastness has prompted their study via remote sensing. Many orbiting sensors view the earth's oceans, but two in particular were specifically design for that purpose: the Coastal Zone Color Scanner (CZCS) and the Sea-viewing Wide Field of View Sensor (SeaWiFS).

Both the CZCS and SeaWiFS systems address remote sensing difficulties that are intrinsic to large bodies of water. Specifically, differences in the optical properties of land based versus aquatic phenomenon create challenging problems when attempting to remotely sense water properties. Two obvious differences are the penetrability of water and the temporally and spatially varying nature of surface waves. Not so obvious differences include the more difficult acquisition of ground truth and the relative importance for atmospheric subtraction. These challenges and others are frequently addressed in the literature and were specifically addressed for both CZCS and SeaWiFS. (Gordon, 1994 and Bukata, 1995)

However, the CZCS and SeaWiFS solutions are optimized for the world's open oceans (and specifically for Case I waters) (Gordon, 1994) and are not always applicable to the coastal ocean regions and other large bodies of water such as the

Laurentian Great Lakes. The atmospheric correction algorithms used for the CZCS data relied on three main assumptions: the water was clear (except for a small amount of phytoplankton-pigment less than 0.25  $\mu\text{g/l}$ ); the atmospheric aerosols absorbed and scattered the same at all wavelengths; and multiple scattering within the atmosphere was negligible (Gordon, 1994). The CZCS atmospheric correction algorithms were based on “knowing” the top-of-the-atmosphere reflectance<sup>1</sup> component due to the atmosphere for at least two wavelengths ( $\rho_{a1}$  and  $\rho_{a2}$  for  $\lambda_1$  and  $\lambda_2$  respectively). A constant,  $n$ , was obtained by assuming a power law relationship:  $(\rho_{a1}/\rho_{a2}) = (\lambda_1/\lambda_2)^n$ . The atmospheric reflectance component,  $\rho_{a3}$  at some other  $\lambda_3$  is simply a matter of extrapolating the same power law to the unknown reflectance at  $\lambda_3$ .

For many open ocean scenes, these assumptions produced reasonable results. However, in areas with spectrally variant aerosols, clouds, and/or non-clear waters the atmospheric correction algorithms used for the CZCS data were far from accurate (Gordon, 1994). Better solutions were developed for SeaWiFS.

The SeaWiFS atmospheric subtraction routines are improved over the CZCS due to the introduction of additional data acquisition bands and the abandonment of the CZCS based power-law-reflectance extrapolation. In particular, the SeaWiFS sensor includes two infrared wavelengths that were not included in the CZCS sensor. These were included to make the “clear water” assumption more accurate.

---

<sup>1</sup> Top-of-the-atmosphere reflectance values,  $\rho$ , are favored in the CZCS and SeaWiFS literature over the top-of-the-atmosphere radiance,  $L$ . The two are related by  $\rho = \pi L / E_0 \cos(\sigma)$  where  $E_0$  is the exo-atmospheric irradiance and  $\sigma$  is the solar declination angle.

Atmospheric models were introduced to bound the aerosol response for the two known wavelengths ( $\lambda_1=765$  nm and  $\lambda_2=865$  nm) and assume that the response in the same ratio would apply for the reflectance at wavelengths in the visible region. A more precise description of the SeaWiFS algorithms will appear later in this report.

With the atmosphere corrected (and a few additional adjustments for masked or flagged data due to ice, direct-path clouds, coccolithophores, etc., as described by McClain, 1995) chlorophyll content and dissolved organic carbon (DOC) are derived from the reflectance values calculated in the visible wavelengths. Yet two anomalies remain: the affect of clouds in the vicinity is unknown and suspended minerals tend to amplify the derived chlorophyll content (Bukata, 1995). Therefore, the SeaWiFS algorithms tend to work well for Case I waters (open ocean and clear) and moderately well for Case II waters (oceanic and higher levels of DOC and chlorophyll) but fail with Case III<sup>2</sup> waters and for waters where cloud cover predominates.

Unfortunately, the Laurentian Great Lakes are primarily Case II and III waters with a high probability of cloud contamination. Robert Bukata and colleagues at Canada's National Water Research Institute, NWRI, in Ontario have characterized the failures for Case III waters (Bukata, 1995, 1997, and 1998 and Jerome, 1996) and are involved with working toward algorithm adjustments. However, the effect of nearby clouds has not been well characterized until now.

---

<sup>2</sup> The term "Case III" applies to contaminated oceanic waters as defined by Jerlov 1976 or, more meaningfully here, as any waters with suspended minerals and/or suspended inorganic matter as defined by Bukata, 1998.

Nearby clouds may contaminate the data in two ways: by changing the magnitude of the spectral radiance into and reflected from the water from the direction of the cloud and by changing the spectral shape of the radiance into and reflected from the water from the direction of the cloud.

Figure 1 is used as motivation to indicate that clouds may indeed be a major source of error in current data and algorithms. This figure shows simulated spectral data of the apparent reflectance that may be measured just below the water surface (3), just above the water surface (2) and in orbit (1) for both a clear sky (solid lines) and single cloud bank sky (-----dashed lines). Just below the water surface, the “measurement” uses the hemisphere above the sensor but below the water surface as the source radiance. The calculations integrated these values to get the total irradiance below the water surface heading down. With this total and the radiance from the direction that will exit the water in the cloud specular direction, the apparent reflectance is easily determined. The n-squared law is also used to equate the above and below water data sets. The two plotted lines below the surface (3) in Figure 1 show that including a cloud will reduce the measured apparent reflectance due to the increased source radiance. As the light exits the water at (2) the cloudless sky apparent reflectance increases slightly over the same measurement below the surface. However, introducing the cloudbank greatly increases the apparent reflectance in the specular direction (2a). The same is true at a sensor in orbit (1). The final plot in the figure (2b) is not measurable and is used for analysis only. It shows the component

arriving at the orbiting sensor due to the water leaving component after atmospheric transmittance is accounted for but without the upwelling radiance.

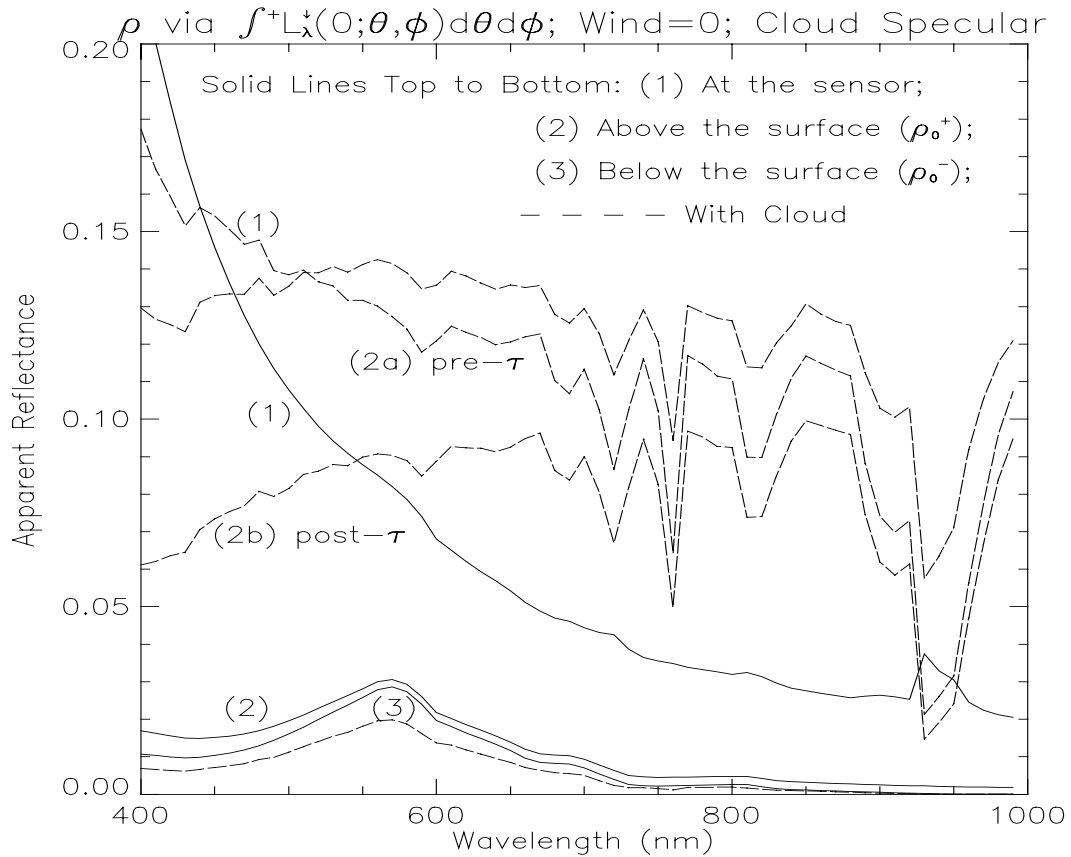


Figure 1: Apparent Reflectance as Measured by at Select Locations. This figure shows simulated spectral data of the apparent reflectance that may be measured just below the water surface (3), just above the water surface (2) and in orbit (1) for both a clear sky (solid lines) and single cloud bank sky (----dashed lines). Just below the water surface, the “measurement” uses the hemisphere above the sensor but below the water surface as the source radiance and the radiance from the direction that will exit the water in the cloud specular direction to determine the apparent reflectance. The n-squared law is also used to equate the above and below water data sets. The two plotted lines below the surface (3) show that including a cloud will reduce the measured apparent reflectance due to the increased source radiance. As the light exits the water at (2) the cloudless sky apparent reflectance increases slightly over the same measurement below the surface. However, introducing the cloudbank greatly increases the apparent reflectance in the specular direction (2a). The same is true at a sensor in orbit (1). The final plot in the figure (2b) is not measurable and is used for analysis only. It shows the component arriving at the orbiting sensor due to the water leaving component after atmospheric transmittance is accounted for but without the upwelling radiance. The simulation used a zero wind speed and the cloud’s specular direction.

The first step in determining the impact of each of these contamination methods is to build a computer model capable of accurately predicting the radiance

reaching an orbiting sensor. Key elements of the model include accurate predictions of radiance transfer in the atmosphere (including clouds), between the atmosphere and water, and in the water. Such a radiance transfer solution program was created as part of this effort. The computer code is called HydroMod and a full description of the program and its use can be found in Appendix I of this report.

Chapter 2 covers the important radiative transfer regimes and describes the solution methods used in the cloud impact study. Included in Chapter 2 is the separation of the problem into modules that provide natural impact analysis areas, creation of the geometrical equations to be used, and descriptions of most of the key elements that are modeled in HydroMod. As the problem is broken into manageable modules, a review of the key literature concerning that module and associated radiative transfer is also included.

The derivation of the error in SeaWiFS derived chlorophyll-a content is covered in Chapter 3. Specifically, the methods of atmospheric correction and the empirically derived formulas pertaining to atmospheric correction and chlorophyll-a concentrations are reviewed.

A discussion of the specific parameters used in the SeaWiFS/Great Lakes cloud impact study is contained in Chapter 4. The actual values that were used and the reasons for using them are provided in Chapter 4.



The results of the study are reported in Chapter 5. Discussions of the data and the expectations and surprises are also included there. However, much of the study was concerned with validating the operation of HydroMod through a series of data acquisitions designed to confirm expected results. This “confirmation of expectations” analysis is not presented in the body of this report. Most of the confirmation of expectations can be found in Appendix II.

Finally, the conclusions and recommendations are included as Chapter 6.



## *Chapter 2*

### **DEFINING THE PROBLEM**

This chapter describes the key elements of an end-to-end hyperspectral radiative transfer model that incorporates all pertinent aspects of a realistic water scene with a broad range of sensitivity parameters. One goal for the creation of the model is that it is flexible enough to be used for many water remote-sensing applications beyond the cloud impact characterization. The problem is defined with this in mind (although the primary concern of this effort is to characterize the affect of circuitous clouds on the radiance at the sensor and the impact to the derived chlorophyll content for the SeaWiFS system.) The specific model parameters used and the cloud impact characterization are covered in later chapters. The path used for the creation of the end-to-end radiative transfer model is also followed in this chapter:

- (1) separation of the radiative transfer into manageable regimes;
- (2) review of the pertinent literature and established solutions for those regimes;
- (3) selection of methods and/or solutions of choice;
- (4) creation of missing components; and

(5) linking the components together.

Radiative transfer through the multiple scattering regimes in a realistic water scene has many challenges (see Figure 2). Including clouds in the vicinity only serves to further complicate the challenges. The individual components (atmosphere, clouds, air-water interface, water, wind roughened surface,...) have been studied to varying degrees and the literature contains several examples of possible individual and partial solutions to the some of the challenges.

At times, the problems are mitigated by assuming a smooth surface (Gordon, 1975), a clear or homogeneous sky (Gordon, 1997), or similar simplifications within the water. At other times, one or more of the problems are directly considered and solutions are sought as the thrust of the research. For instance, several models have been generated for propagation of light in the underwater light field (Gordon, 1975; Kirk, 1984; Kirk, 1991; Morel, 1993; Bukata, 1981; Mobley, 1994; and Jerome, 1988) or for modeling more complex atmospheric phenomenon (Plass, 1968 and Plass, 1969).

Yet even those studies have only pursued one or two parts of the overall water remote-sensing problem. The challenge is to construct a comprehensive model utilizing the best available methods to date in each of the problem areas.

Specifically, a comprehensive model will incorporate a standard radiative transfer code (such as MODTRAN) that allows for user modifications of the

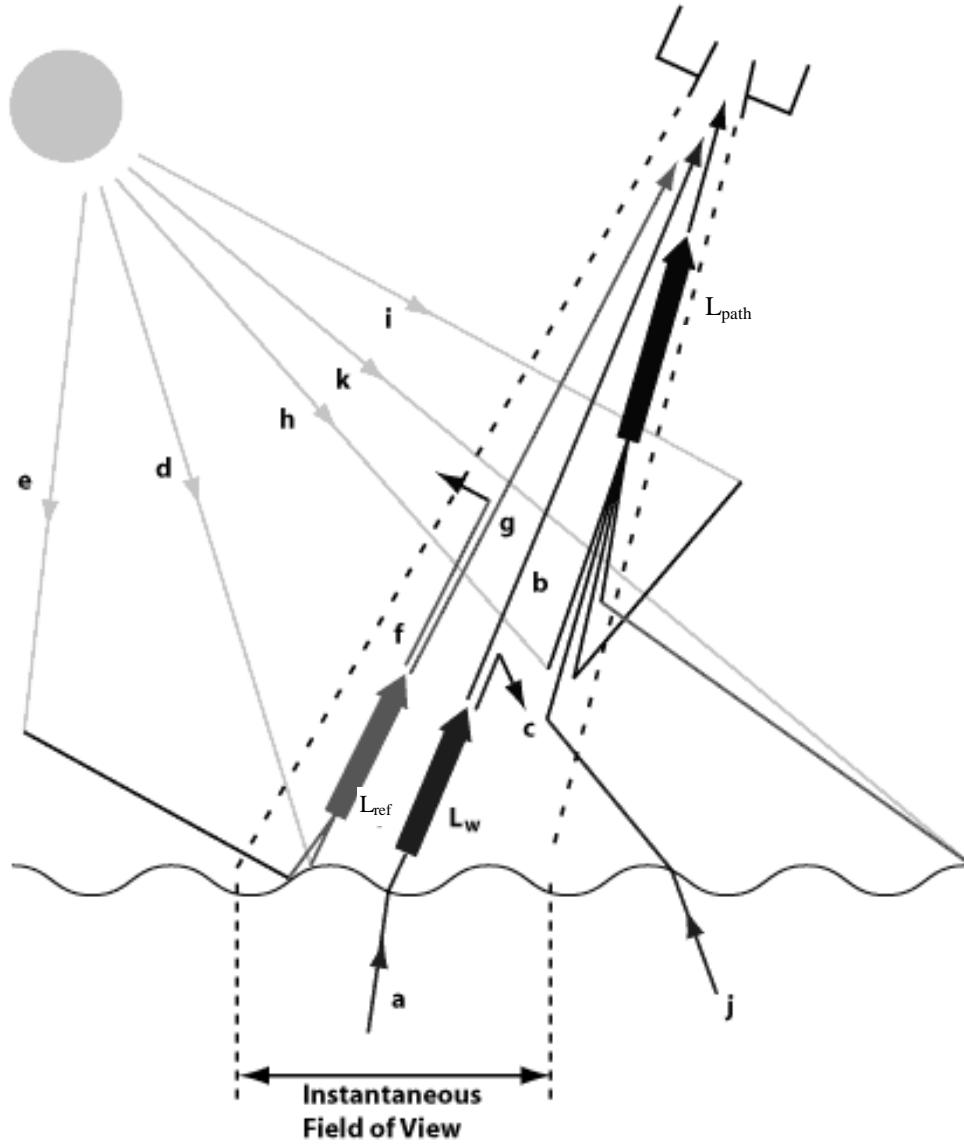


Figure 2: Light Pathways in the Atmosphere: a) The light path of the water-leaving radiance. b) Shows the attenuation of the water-leaving radiance. c) Scattering of the water-leaving radiance out of the sensor's FOV. d) Sun glint (reflection from the water surface). e) Sky glint (scattered light reflecting from the surface). f) Scattering of reflected light out of the sensor's FOV. g) Reflected light is also attenuated towards the sensor. h) Scattered light from the sun which is directed toward the sensor. i) Light which has already been scattered by the atmosphere which is then scattered toward the sensor. j) Water-leaving radiance originating out of the sensor FOV, but scattered toward the sensor. k) Surface reflection out of the sensor FOV which is then scattered toward the sensor.  $L_w$  = Total water-leaving radiance.  $L_{ref}$  = Radiance above the sea surface due to all surface reflection effects within the IFOV.  $L_{path}$  = Atmospheric path radiance. (This figure is adapted from Robinson, I.S., 1983: Satellite observations of ocean colour, Philo. Trans. Royal Soc. of London, Series A, Volume 309, 338-347 and obtained from URL [http://phyvax.ir.miami.edu:8001/chris/envr\\_optics.html](http://phyvax.ir.miami.edu:8001/chris/envr_optics.html))

atmospheric constituents. It will allow the introduction of clouds (varying type, location, and percent coverage) to the standard atmospheres. At the air water interface an accurate wind roughened surface will form the boundary. Below the water, the radiative transfer must include the absorption and scattering of the water constituents as well as the water itself. Many existing methods discussed by Bukata (1995) and Mobley (1994) allow for changing the materials within the water to generate the volume spectral reflectance. Mobley's HYDROLIGHT (Mobley 1995) code in particular, also generates three dimensional radiance distributions within and exiting the water. Most other codes, including the Monte Carlo codes discussed and used by Bukata, require modifications to obtain a three dimensional radiance distribution exiting the water.

To obtain radiance at the sensor, the end-to end model will propagate the underwater-scattered field back through the wind roughened air/water interface, add the radiance reflected off the water surface, and propagate the sum back through the atmosphere to the sensor.

To facilitate impact analyses, a method by which the radiative field can be viewed and studied is also required. Preferably, the radiative field in each regime can be viewed and studied and separated to allow in-depth impact analyses.

In the discussion to follow, I refer to any photons that reach the target (i.e. the water's surface) as source photons. If they enter the water and end up exiting the water toward the sensor, they become the "a" type photons in **Figure 2**; if they exit in



## GEOMETRY USED

I used the world coordinate system geometry found in *Remote Sensing The Image Chain Approach* (Schott, 1997) with one modification. Referring to Figure 4, the X, Y, and Z axes are North, West, and vertical respectively. The declination angle between the sun and the normal to the earth,  $\sigma$ ; and the declination angle between the sensor and the normal to the earth<sup>3</sup>,  $\theta_d$ , are bounded by  $0^\circ$  and  $90^\circ$ ; the sun directly vertical has a declination angle of  $\sigma = 0^\circ$ . The azimuthal angles between the X-axis (North) and the projection of the sun,  $\phi_s$ , and the detector,  $\phi_d$ , are positive counter-clockwise looking down. These are the fixed coordinates. Wave orientation, wind direction, and cloud positions, will be referenced to the fixed coordinates of Figure 4.

The geometry defined in Figure 4 is used in calculations and the identification of directional information associated with incoming and outgoing radiance. However, for viewing the magnitude of the radiance in all (hemispherical) directions simultaneously, other means are required. The method used in this work is a polar view representing the directional information and a gray scale that represents the magnitude information. The polar view is demonstrated in Figure 5. With this view, the center of the circular section would be straight up (or down as the case may be)

---

<sup>3</sup> This is the aforementioned modification; Schott uses  $\theta$  for the detector angle. I will use the more generic  $\theta$  to represent an arbitrary declination angle in describing the hemisphere in terms of  $\theta$  and  $\phi$ .



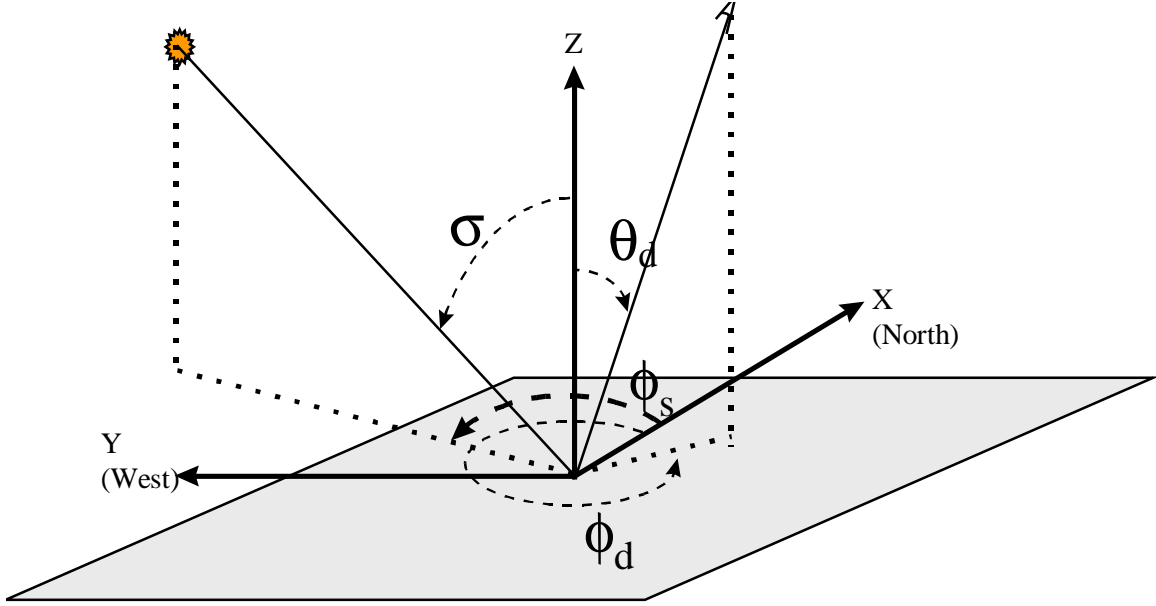


Figure 4: Angle Definitions For The Geometry Used. The X, Y, and Z axes are North, West, and vertical respectively. The declination angle between the sun and the normal to the earth,  $\sigma$ ; and the declination angle between the sensor and the normal to the earth,  $\theta_d$ , are bounded by  $0^\circ$  and  $90^\circ$ ; the sun directly vertical has a declination angle of  $\sigma = 0^\circ$ . The azimuthal angles between the X axis (North) and the projection of the sun,  $\phi_s$ , and the detector,  $\phi_d$ , are positive counter-clockwise looking down

and the outer edges of the outer-most circle is the horizon. The declination angle,  $\theta$ , increases from  $0^\circ$  at the center to  $90^\circ$  around the outer edge. I define the azimuth angle,  $\phi$ , to be North =  $0^\circ$  at the top of the graph and positive West of North. However, an advantage of these polar plots is that the azimuthal angle reference perspective is completely arbitrary as long as it remains consistent. (That is, having North as the top or not and positive East or West of North is completely arbitrary as long as we are consistent once defined. I will refer to my defined reference of North =  $0^\circ$  at the top and positive West of North throughout this report.)

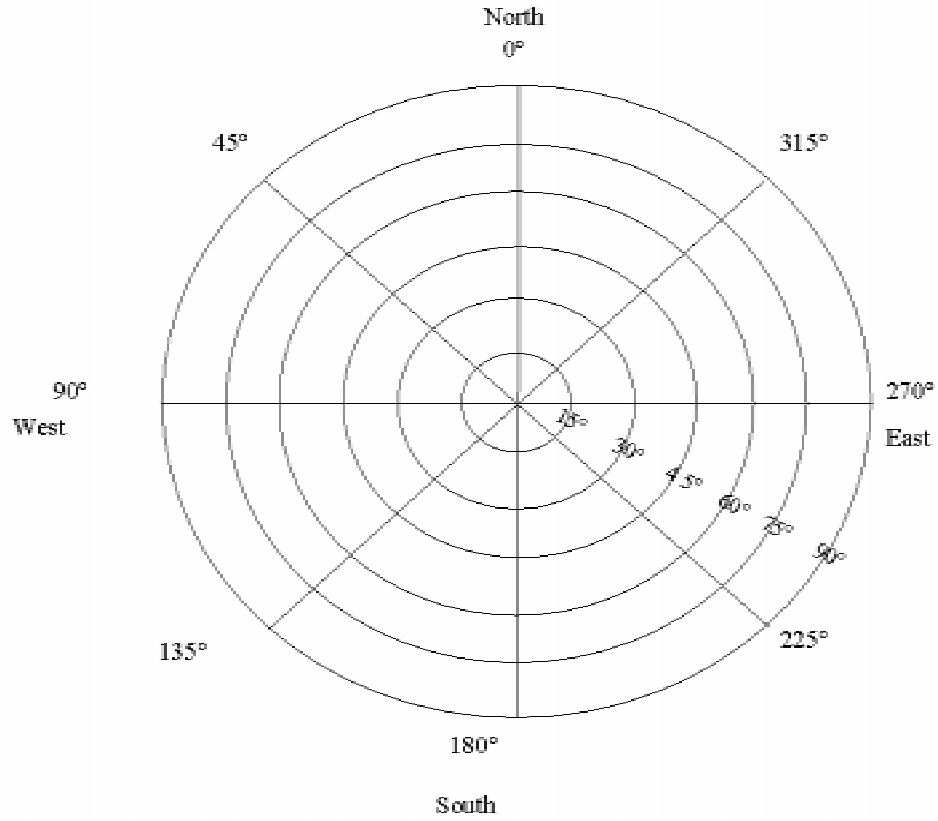


Figure 5: Standard Polar View. With this view, the center of the circular section would be straight up (or down as the case may be) and the outer edges of the outer-most circle is the horizon. The declination angle,  $\theta$ , increases from  $0^\circ$  at the center to  $90^\circ$  around the outer edge. Reference Figure 4 for the geometry definitions and Figure 6 for an example of the polar plot style with radiance levels inserted using gray scale values.

## RADIATION IN THE AIR

The source radiation propagation is the direct sunlight source irradiance, the downwelled radiance from a clear sky (Rayleigh scattered), downwelled radiance from aerosols and water vapor, and the affect of clouds. Each of these are considered to be a radiance source to the surface of the water and they sum to  $L_\lambda(\theta, \phi)$ :

$$L_{\lambda}(\theta, \phi) = L_{\lambda}(\sigma, \phi_s) + L_{\lambda R}(\theta, \phi) + L_{\lambda a}(\theta, \phi) + L_{\lambda C}(\theta, \phi)$$

EQ 1

Where  $L_{\lambda}(\sigma, \phi_s)$  = Radiance directly from the sun

$L_{\lambda R}(\theta, \phi)$  = Rayleigh scattered radiance

$L_{\lambda a}(\theta, \phi)$  = Aerosol/water vapor scattered radiance (including Rayleigh/Aerosol Interaction)

$L_{\lambda C}(\theta, \phi)$  = Radiance scattered from clouds

Light scattering in the atmosphere and off the surface of the water ( $L_{\text{path}}$  and  $L_{\text{ref}}$  in **Figure 2**) will also reach the sensor and contaminate the data.

The standard output from this stage is a two-dimensional radiance magnitude and direction for a point on the sea surface at each wavelength of interest. For instance, combining a large source irradiance from the sun with typical atmospheric scatter (Schott, 1997 and Bukata, 1995 derived from Moon, 1942) and a cloud reflection component with the geometry found in Figure 5 may produce the distribution found in Figure 6. Though this section seems to be straight forward, the task is large when the full radiation pattern at each wavelength is considered. Note that Figure 6 is only a sample of one possible output. By using the Interactive Data Language (IDL) from Research Systems Incorporated, multiple surface and plotting routines are available.

### **Sun Source Radiance**

Sun source radiation in remote sensing is normally viewed as an exo-atmospheric irradiance,  $E_{\text{sun}}$ , attenuated by the atmosphere and impinging on a point on the earth's surface. However, irradiance does not provide the directional

information of the sun,  $\sigma$  and  $\phi_s$ , nor can it provide  $L_\lambda(\theta, \phi)$  for the hemisphere above the water's surface. A radiative transfer code such as MODTRAN can be used to obtain the required hemispherical radiance (see the next section), but the direct solar radiance must come from some other means. A less spectrally accurate, but

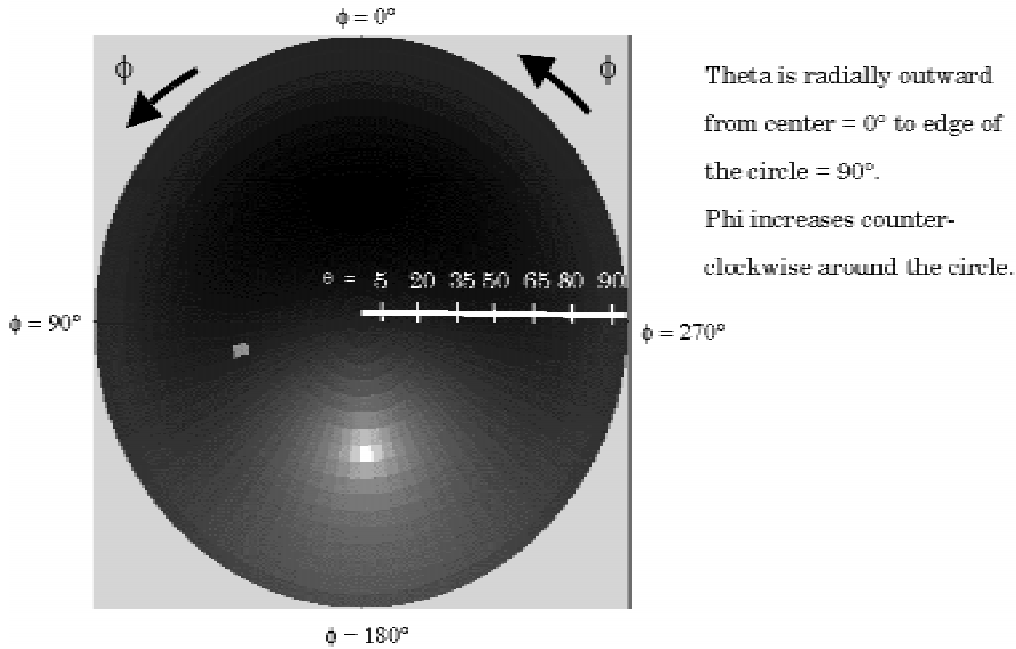


Figure 6: Example Possible Output. One hardcopy output style is illustrated here. The declination angle,  $\theta$ , runs radially outward from the center of the plotted circle. The azimuthal angle,  $\phi$ , runs counter-clockwise around the circle. The bright spot just below and left of center would represent, here, the input radiance from a cloud at roughly  $\theta = 35^\circ$  and  $\phi = 110^\circ$ . The brightest spot below the center of the circle represents the sun forward scattering. Most of the sky radiance is diffuse with the non-uniform illumination clearly visible.

intuitively pleasing remedy is found following the developments of Schott (1997) and Maul (1985) by assuming the sun is a blackbody radiator between 5800 Kelvin (Schott, 1997) and 5900 Kelvin (Maul, 1985). Using Planck's radiation equation for radiant exitance,  $M_\lambda$ , and then noting that  $L_\lambda$  is essentially zero for directions other than  $(\sigma, \phi_s)$ , we can obtain an equation for  $L_\lambda(\sigma, \phi_s)$ . The blackbody radiant exitance is given as

$$M_\lambda = \frac{2\pi hc^2}{\left[ e^{\frac{hc}{\lambda kT}} - 1 \right] \lambda^5}$$

EQ 2

with

$h$  = Planck's Constant  
 $= 6.6256 \times 10^{-34}$  Joule•Sec  
 $c$  = Speed of Light  
 $= 3 \times 10^8$  m/sec  
 $k$  = Boltzman's Constant  
 $= 1.38 \times 10^{-23}$  Joules/Kelvin  
 $T$  = Temperature (Kelvin)  
 $\lambda$  = Wavelength

With the sun radiating the same in all directions (at  $T=5800K$  or  $5900K$ ), the sun's source radiance can be calculated as  $L_\lambda(\sigma, \phi_s) = M_\lambda/\pi$ . Relating the earth's exo-atmospheric sun source irradiance,  $E_{\text{sun}\lambda}$ , to  $L_\lambda(\sigma, \phi_s)$  is simply a matter of integrating a constant  $L_\lambda(\sigma, \phi_s)$  over the solid angle subtended by the sun at the earth. Using the

mean sun-earth distance of  $1.497 \times 10^{11}$  meters and a sun radius of  $6.96 \times 10^8$  meters gives a solid angle of  $6.791 \times 10^{-5}$  sr which means that  $E_{\text{sun}\lambda} = L_{\lambda}(\sigma, \phi_s)(6.791 \times 10^{-5} \text{ sr})$ .

At the eight specific wavelengths detected by SeaWiFS this approximation may be adequate. However, the sun is not a true blackbody and the exo-atmospheric irradiance has more spectral variation than predicted by the Planck blackbody radiation (EQ 2). This development for  $L_{\lambda}(\sigma, \phi_s)$  can be used for relative reference to the true exo-atmospheric solar irradiance as in Figure 7. In Figure 7, the measured exo-atmospheric solar irradiance (obtained from the Air Force Research Laboratory) is compared to the Planck blackbody calculated radiance from the above analysis. The two smooth curves in Figure 7 are for a 5900 Kelvin (upper curve) and a 5800 Kelvin (lower curve) blackbody sun. We may conclude from Figure 7 that a more accurate  $L_{\lambda}(\sigma, \phi_s)$  than that found using the above development is obtained by attenuating the measured  $E_{\text{sun}\lambda}$  with the atmospheric transmission coefficient,  $\tau$ , (to get the irradiance at the water surface) and dividing by the solid angle subtended by the sun,  $6.791 \times 10^{-5}$  sr. It is also reasonable to assume a constant radiance over that solid angle.

### **Sky Source Radiance**

The direct solar irradiance is by far the largest contributor to the source illumination. As such, some of the early work in underwater illumination studies (including some of the Monte Carlo codes previously mentioned) considered only a

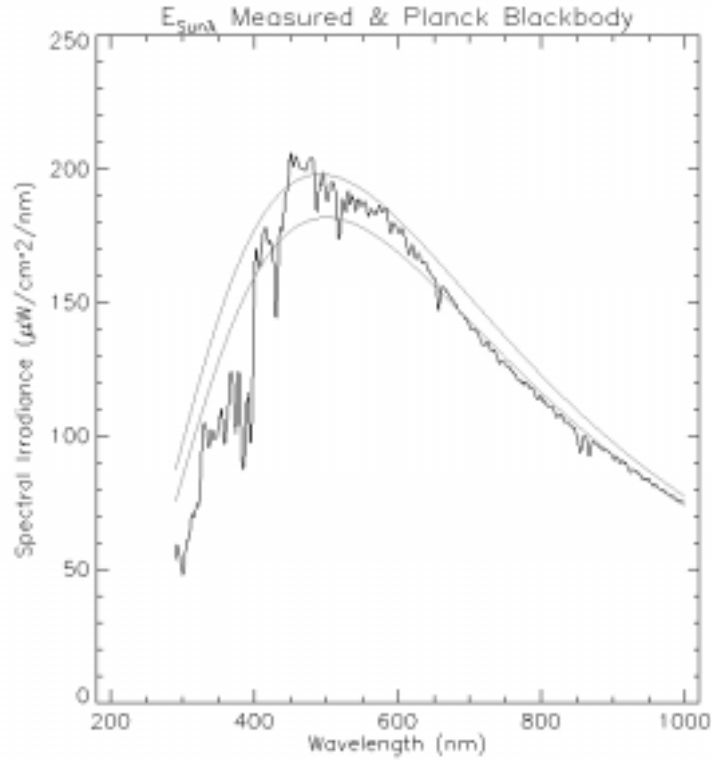


Figure 7 Exo-atmospheric Solar Spectral Irradiance for measured data and calculated from Planck's radiation law using the sun as a blackbody disk at 5800 Kelvin (lower smooth curve) and 5900 Kelvin (upper smooth curve).

single source (Bukata, 1995 and Kirk, 1991). (To be fair, all of the Monte Carlo codes could be employed using several runs of a single source and their output combined using superposition. This would give the same result as a multiple source input run would produce.) The single source method loses credibility when the water leaving radiance in all directions is the primary objective.

Since the water leaving radiance in all directions is indeed one of the primary objectives of this work, accurate source radiance  $L_{\lambda}(\theta, \phi)$  from all  $(\theta, \phi)$  directions is required. There are several avenues available to determine  $L_{\lambda}(\theta, \phi)$  from all  $(\theta, \phi)$

directions. An obvious next approximation is to use uniform sky illumination. However, even in the early 1940's, uniform sky illumination models were replaced with measurement derived cardioidal illumination formulas (Moon and Spencer, 1942). The sky illumination models continued to improve and become more and more complex. The Air Force released the low-resolution atmospheric transmission model, LOWTRAN 2 in 1972 (Selby, 1972). The sole purpose of LOWTRAN 2 was to compute the transmittance through a user-defined atmosphere. Calculation of radiance was added to LOWTRAN 4 in 1978 (Kneizys, 1980). LOWTRAN eventually gave way to MODTRAN (moderate resolution atmospheric transmission code) and the current version is MODTRAN 4.0 (Acharya, 1998).

Though promisingly accurate, the LOWTRAN and MODTRAN family of codes were considered cumbersome to use and somewhat time consuming in the calculations (Gregg, 1990). Closed form type solutions along the lines of the original Moon and Spencer (1942) work were and are still being pursued. One promising line of development progressed from Leckner (1978) through Bird and Riordan (1986) to Gregg and Carder (1990). The Gregg and Carder model is specifically for clear maritime atmospheres and compares quite well to measured irradiance values (Gregg, 1990); the previous versions were only intended for use over non-maritime conditions (Bird, 1986).

However easy these models are, they have neither the flexibility nor the industry acceptance of MODTRAN (not to mention the endorsement by the United



States Air Force). Combine those advantages with the MODTRAN experience level at RIT (which minimizes the “cumbersome” argument previously stated) and MODTRAN is a very attractive method for computing the sky components of  $L_\lambda(\theta, \phi)$  from all  $(\theta, \phi)$  directions. Another MODTRAN advantage is that atmospheric attenuation of the  $L_\lambda$  component from the  $\sigma, \phi_s$  direction can also be obtained in addition to both the Rayleigh scatter component,  $L_{\lambda R}(\theta, \phi)$ , and the aerosol/water vapor component,  $L_{\lambda a}(\theta, \phi)$ . Using repeated runs of MODTRAN with the “sensor” located at the water surface can produce  $L_{\lambda R}(\theta, \phi) + L_{\lambda a}(\theta, \phi)$  for the entire hemisphere above the water surface.

Yet another MODTRAN advantage is that the amount and type of atmospheric constituents can be variable and may come from standard aerosol models built in to MODTRAN, radiosonde data, or tabular self-generated form. Virtually any atmosphere can be modeled using MODTRAN and  $L_\lambda(\theta, \phi)$  from any and all  $(\theta, \phi)$  directions can be calculated. This functionality means that the atmosphere for a given day can be modeled very accurately. In fact, algorithms that rely on inverting radiance at the sensor by correcting for the atmosphere can be tested with “ground-truth” measured data.

### **Radiance from Clouds**

To build realistic atmospheres, we need the ability to add variable clouds at select locations that would, in turn, modify the  $L_\lambda(\theta, \phi)$  from the pertinent  $(\theta, \phi)$  directions to give  $L_{\lambda C}(\theta, \phi)$ . The literature has many cloud models that range from a built-in module in MODTRAN to stand alone Monte Carlo style codes that calculate

bi-directional reflectance factors (BDRF) for a given cloud with variable extinction coefficient,  $\beta$ , in three dimensions. One of the latter models was written and used by the University of Arizona's Institute of Atmospheric Physics (Várnai, 1998). The Monte Carlo code was specifically designed to compute the BDRF using the sun as an input source and multiple directions as the output reflectance angles. If this or similar Monte Carlo based codes were used in this effort, a geometry inversion would be required along with the use of reciprocity to speed the computations. That is, we would use the  $(\theta, \phi)$  direction as the single source input and calculate BDRF. The true multiple source input to the cloud (direct sun plus scattered skylight) would then be used, assuming reciprocity holds, to calculate  $L_{\lambda C}(\theta, \phi)$ . The process is illustrated in Figure 8.

In the next few paragraphs I will derive a method for calculating the radiance into the point of interest on the water surface due to a cloud,  $L_{\lambda C}(\theta, \phi)$ , in the  $(\theta, \phi)$  direction. In the quest of accuracy in the development, more and more uncertainty is added until the final calculated  $L_{\lambda C}(\theta, \phi)$  is quite questionable. That high uncertainty will lead to an elegant and simple solution for determining  $L_{\lambda C}(\theta, \phi)$  that applies quite well to almost any atmosphere. The first step is to derive a method of calculating  $L_{\lambda C}(\theta, \phi)$ .

The contribution to  $L_{\lambda}(\theta, \phi)$  from clouds,  $L_{\lambda C}(\theta, \phi)$ , in EQ 1 is fairly complex if the full impact is used. Referring to Figure 8, the cloud contribution to  $L_{\lambda}(\theta, \phi)$  can be calculated as

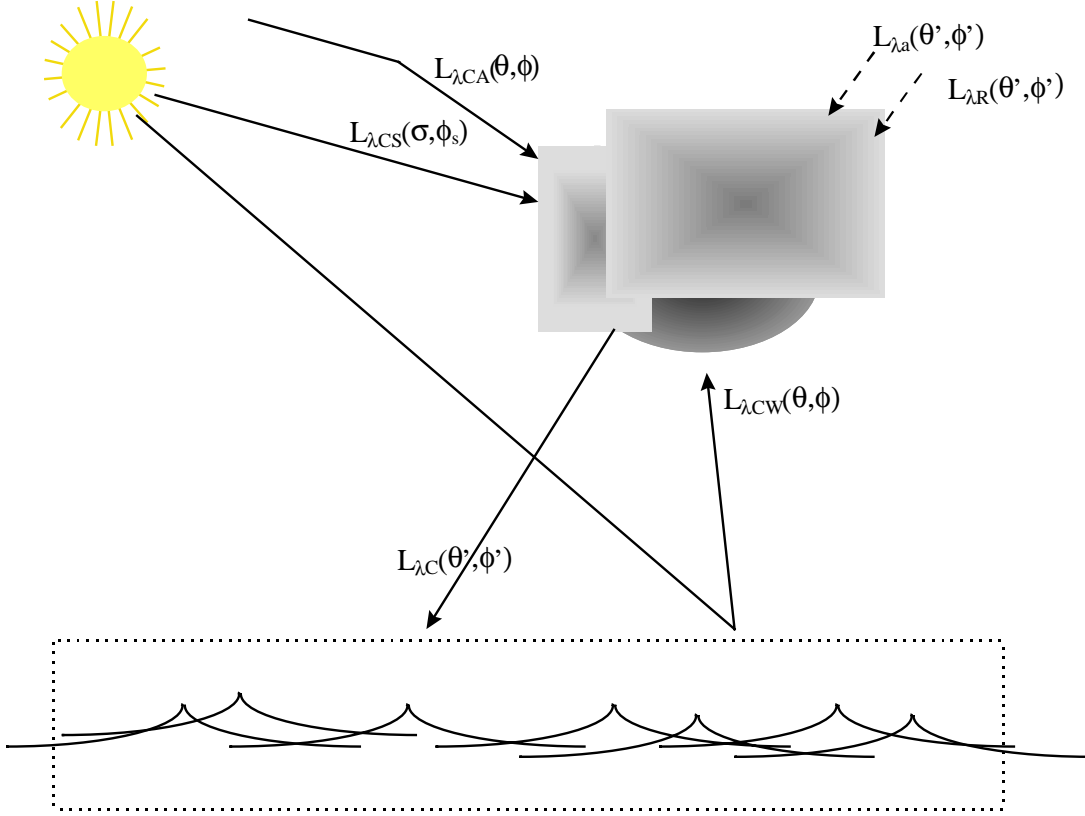


Figure 8: Radiance To and From Clouds. Obtaining the cloud contribution,  $L_{\lambda C}(\theta', \phi')$  to the total input radiance term,  $L_{\lambda}(\theta, \phi)$ , requires knowing the radiance from the sun to the cloud,  $L_{\lambda CS}(\sigma, \phi_s)$ ; the radiance reflected off the water to the cloud,  $L_{\lambda CW}(\theta, \phi)$ ; the radiance from the atmosphere to the cloud,  $L_{\lambda CA}(\theta, \phi)$ ; and the removal of the Rayleigh and aerosol/water vapor components from the  $(\theta', \phi')$  direction. The last step is required because the  $L_{\lambda CA}(\theta, \phi)R(\alpha, \gamma; \theta', \phi')$  term in EQ 3 includes the Rayleigh and aerosol components attenuated by the cloud EQ 1 also includes the terms un-attenuated by the cloud.

$$L_{\lambda C}(\theta, \phi) = L_{\lambda C}(\theta', \phi') = [L_{\lambda CS}(\sigma, \phi_s)R(\sigma, \phi_s; \theta', \phi') + L_{\lambda CW}(\alpha, \gamma)R(\alpha, \gamma; \theta', \phi') + L_{\lambda CA}(\alpha, \gamma)R(\alpha, \gamma; \theta', \phi')] \tau_c - L_{\lambda R}(\theta', \phi') - L_{\lambda a}(\theta', \phi') \quad \text{EQ 3}$$

where

$L_{\lambda C}(\theta', \phi')$  = Cloud contribution from the specific  $\theta', \phi'$  direction

$L_{\lambda CS}(\sigma, \phi_s)$  = Radiance Input to the cloud from the sun

$R(a, b; c, d)$  = Bi-directional Reflectance Factor from (a, b) direction to (c, d) direction

$L_{\lambda CW}(\alpha, \gamma)$  = Radiance Reflected off the water to the cloud

$L_{\lambda CA}(\alpha, \gamma)$  = Combined Rayleigh and aerosol scattering to the cloud  
 $\tau_c$  = transmission coefficient from the cloud to the point on the water  
 $(\alpha, \gamma)$  = input angles for radiance to the cloud over the entire input sphere

EQ 3 would need to be solved for each set of  $(\theta', \phi')$  for which a cloud would impact the  $L_{\lambda}(\theta, \phi)$  input radiance. Some of the components of  $L_{\lambda C}(\theta', \phi')$  are straightforward:  $L_{\lambda CS}(\sigma, \phi_s) = L_{\lambda}(\sigma, \phi_s)$  with, perhaps, a different attenuation factor due to atmospheric propagation for instance. However, the sky radiance term,  $L_{\lambda CA}(\alpha, \gamma)$ , is much more difficult and the water radiance term,  $L_{\lambda CW}(\alpha, \gamma)$  is even worse. (Subtracting out  $L_{\lambda R}$  and  $L_{\lambda a}$  in the  $(\theta', \phi')$  direction is straightforward and those components already are calculated with MODTRAN.)

The largest expected input radiance component to the cloud is the direct sunlight component,  $L_{\lambda CS}(\sigma, \phi_s)$ . With some preliminary analysis, it may be sufficient to neglect the other components. (Certainly if nearby clouds are found to greatly affect the SeaWiFS algorithms using only the  $L_{\lambda CS}(\sigma, \phi_s)$  term as input to the clouds, then using the rest of the components would only add to the impact.)

The radiance component coming from the atmosphere,  $L_{\lambda CA}(\alpha, \gamma)$ , may require many more runs of MODTRAN for the “sensor” located at the cloud position and varying  $\alpha$  and  $\gamma$ . This method would assume, for input purposes only, that the cloud is a point located at the “sensor” location. Other possibilities are to simplify  $L_{\lambda CA}(\alpha, \gamma)$  somehow with, perhaps, averaging or with the models previously discussed (Moon and Spencer, 1942; Gregg, 1990; and Bird, 1986).

The input to the clouds coming from the water surface is another challenge. Radiance coming from the water's surface is either reflected sun light or sky light or light that penetrates the surface, scatters off of something below the surface, and exits again. Further complications come from the spatial extent of both the water and the cloud so that radiance from the input angles,  $\alpha$  and  $\gamma$ , direction arrive at each spatial location on the cloud which means that cloud shadowing may be important. Two simplifications are possible: one is to only use the reflected component from the water's surface and the other is to treat the cloud as a point.

Using only the reflected component would simplify the problem, but it would slightly underestimate  $L_{\lambda CW}(\alpha, \gamma)$ . Since the goal is to look into the water we would tend towards times when the reflected component is minimized. Water has high penetrability at sun zenith angles of  $\sigma < 70^\circ$  or so (Bukata, 1995). Only these small sun zenith angles would be used which would lower the sun-water-cloud reflected component.

Treating the cloud as a point has some advantages in that the spatial extent of the cloud is ignored. That means that no shading occurs on the water surface and only one set of radiances from the  $(\alpha, \gamma)$  directions,  $L_{\lambda CW}(\alpha, \gamma)$ , is needed. Proceeding with this method, the water leaving radiance in all directions would be calculated assuming a cloudless sky ( $L_{\lambda C}(\theta, \phi) = 0$ ) and set equal to  $L_{\lambda CW}(\alpha, \gamma)$ . The water leaving radiance would then be re-calculated with the new input  $L_{\lambda}(\theta, \phi)$  (in which  $L_{\lambda C}(\theta, \phi) \neq 0$ ) and only the component toward the sensor is used. Obviously, this method requires

many more computations than simply using the reflected component or ignoring the water component altogether. We must also keep in mind the accuracy obtained by the extra calculations with respect to the accuracy of the reflectance from the cloud.

The above discussion and all of the associated uncertainty provides only one portion of the calculation of  $L_{\lambda C}(\theta, \phi)$ . We also need to define the cloud itself and that is where most of the uncertainty lies (Várnai, 1996).

It is difficult to define what is a cloud and what is not a cloud (Várnai, 1996). Determining the bi-directional reflectance from this ill-defined phenomenon is even more difficult. There are large uncertainties in the actual cloud definition which somewhat alleviates the accuracy requirements of the input radiance to the cloud itself. Therefore, ignoring the radiance from the water as an input to the cloud should not greatly affect the overall uncertainty. I'll use this same simplification later in the aforementioned elegant and simple  $L_{\lambda C}(\theta, \phi)$  determination method.

Several models can be found in the literature that can help determine  $L_{\lambda C}(\theta, \phi)$  once the cloud is defined and the radiance into the cloud is known. One promising existing and available code called *Streamer* was written by Jeffery Key at Boston University (Key, 1998). An advantage of *Streamer* is its mirror to MODTRAN for several input parameters including the surrounding atmospheric makeup and the geometry. (That is an advantage to those who use MODTRAN extensively; it may be a disadvantage to some.) However, a disadvantage of using *Streamer* is the complexity of running the code and of the actual code itself.

The Institute of Atmospheric Physics' cloud model previously mentioned is a Monte Carlo based code that calculates the bi-directional reflectance factor for a given input direction and a defined set of output directions. The data set that constitutes the cloud is a three-dimensional set of extinction coefficients and a three dimensional scattering phase function. The code can use simple model geometry (such as plain parallel clouds) to complex inhomogeneous 3-D varying models. (Várnai, 1998)

As previously stated, if the Monte Carlo based code is used, the “input” direction for the bi-directional reflectance factor calculations will be the reciprocal to the  $(\theta', \phi')$  direction and  $R(\theta', \phi'; \alpha, \gamma)$  is set equal to  $R(\alpha, \gamma; \theta', \phi')$  via reciprocity. The  $L_{\lambda C}(\theta', \phi')$  component to  $L_{\lambda}(\theta, \phi)$  is then found by summing the radiance reflected by the cloud to the point on the water surface from each cloud input direction.

$$L_{\lambda C}(\theta', \phi') = \left[ \sum_i \sum_j L_{\lambda CS/A}(\alpha_i, \gamma_j) R(\alpha_i, \gamma_j; \theta', \phi') \right] \tau_c - L_{\lambda a}(\theta', \phi') - L_{\lambda R}(\theta', \phi') \quad \text{EQ 4}$$

That is a lot of work with a lot of uncertainty in the cloud definition and a lot of uncertainty in the radiance into the cloud which equates to even more uncertainty in  $L_{\lambda C}(\theta', \phi')$ . Further, all of these calculations are for that one cloud in that one location and that one moment in time (since the atmosphere and the cloud will change as a function of time).

## **An Elegant and Simple Method**

A few paragraphs back we concluded that since the uncertainties in the cloud definition were expected to be large, ignoring the water leaving radiance component should not appreciably impact the total radiance coming from the direction of the cloud. This same argument may be taken further: since large uncertainties exist for ANY cloud size, shape, elemental particles, scattering functions,..., why not simply use representative radiances for  $L_{\lambda C}(\theta', \phi')$  and let that define the cloud? The impact analysis could surely be performed using radiance values. This greatly simplified and elegant method would rely solely on finding representative radiance values to use for  $L_{\lambda C}(\theta', \phi')$  in the impact analysis. Four methods jump immediately to mind for finding the representative radiances: we could use the two codes and the associated methods previously discussed; we could use values gleaned from the literature; we could use the cloud models built in to MODTRAN; or we could use measured data from representative clouds.

Literature reviews yielded little help below  $1\mu\text{m}$  for either reflectance values or cloud leaving radiance values. Both of the cloud prediction codes were highly dependent on the cloud definition data and virtually any spectral response can be generated with the “right” cloud definitions. The MODTRAN method and measurements both produced better results.

Using MODTRAN provided excellent results easily and quickly. I set up MODTRAN by putting my sensor just above the clouds and looked down at several



different look angles and an earth surface of zero reflectance. I used several clouds built in to MODTRAN. I ran the same scenario with the sensor just below the clouds and looking up at several angles. With the output from these runs I was able to generate a family of curves for the spectral radiance exiting the MODTRAN modeled clouds.

The family of cloud spectral response curves generated with this method all had very similar spectral shapes. The relative magnitudes, however, varied by more than a factor of 15 from the brightest clouds to the darkest clouds that I was able to generate. Figure 9 shows some of the cloud spectral response data. The shape of the cloud spectral response was found by averaging representative bright, medium, and dark cloud spectral responses. In Figure 9(a) the cloud spectral response in radiance ( $\mu\text{W}/\text{cm}^2 \cdot \text{sr} \cdot \text{nm}$ ) is plotted along with the sun's forward scattering radiance after equating the total integrated radiance of the two spectral files. This is the cloud reference spectral radiance data used in most of the study. The third plot in Figure 9(a) is the cloud reference spectral radiance scaled by a factor of 0.3 and represents one of the brightest clouds found using the MODTRAN method discussed. In Figure 9(b), the cloud spectral response from Figure 9(a) was scaled by a factor of 0.065 and plotted along with the average sky radiance using the entire hemisphere. In both Figure 9(a) and Figure 9(b) the cloud spectral response is certainly less blue and more green and red (which yields a visually white cloud) than either the sun forward scatter or the average sky component.

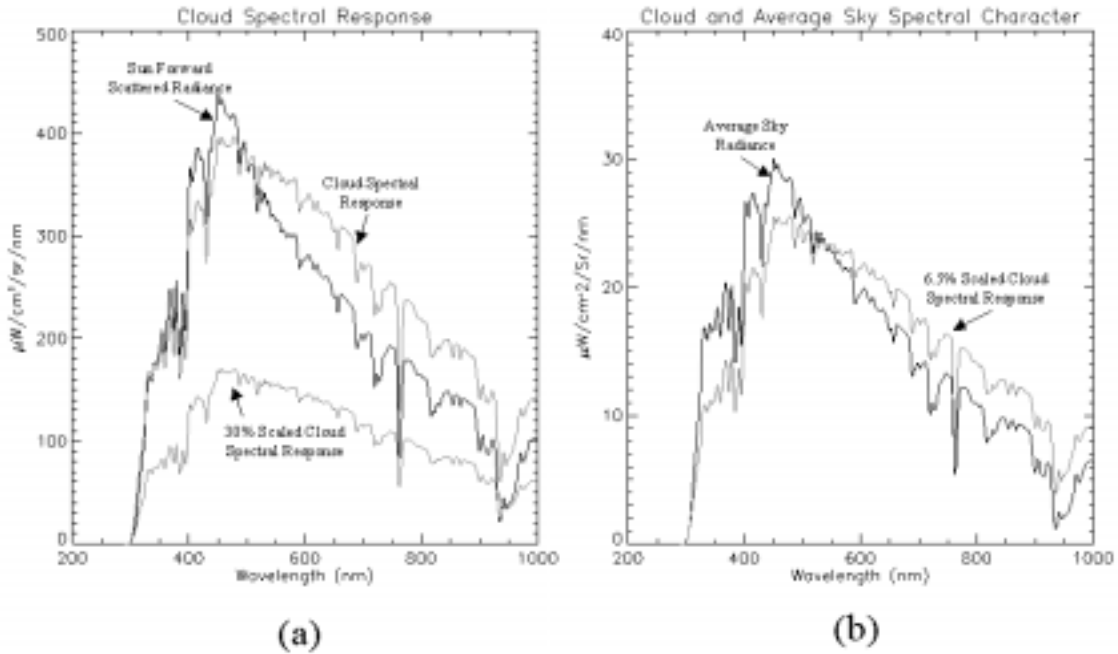


Figure 9: Cloud Spectral Response Curves compared to (a) the sun forward scattering term and (b) the average sky term. In (a) the cloud spectral response in radiance ( $\mu\text{W}/\text{cm}^2 \cdot \text{sr} \cdot \text{nm}$ ) is plotted along with the sun's forward scattering radiance after equating the total integrated radiance of the two spectral files. The third plot is the cloud spectral radiance scaled by a factor of 0.3 and represents one of the brightest clouds found using the MODTRAN method discussed. In (b), the cloud spectral response from (a) was scaled by a factor of 0.065 and plotted along with the average sky radiance using the entire hemisphere. In both (a) and (b) the cloud spectral response is certainly less blue and more green and red than either the sun forward scatter or the average sky component.

The family of cloud spectral curves generated with the MODTRAN method also provides the range of representative values for “bright” clouds to “dark” clouds. Using the larger cloud spectral response from Figure 9(a) as the normalizing curve, the cloud family ranged from scale factors of 0.35 to 0.015 with a very bright cloud having a scale factor above 0.25 and a very dark cloud having a scale factor below 0.03.

Similar data were obtained by spectrally measuring the radiance from representative clouds using an Analytical Spectral Devices, Incorporated, (ASD) Full Range (FR) Spectroradiometer. Some of these data are shown in Figure 10. The

spectral radiance from several clouds is plotted in Figure 10(a); obviously, the spectral character of these real clouds is not as well behaved as the MODTRAN family of clouds. Some of the clouds show a flatter spectrum and some show a less flat spectrum. The average of 70 cloud data sets is plotted along with the average of 40 blue sky data sets in Figure 10(b). These data show many similarities with the data in Figure 9. The biggest differences between the ASD measurements and the MODTRAN predictions include the variability in the measured cloud spectral data (from cloud to cloud as shown in Figure 10) and the overall flatness of the measured data is less than the MODTRAN data. That is, the measured clouds and the measured sky were both more blue and less red than the MODTRAN predictions. The ratios of sky to cloud, however, were very similar.

The data in Figure 10 are all normalized to have the same total integrated radiance from 350nm to 1000nm. Some clouds obviously have much more blue content and much less red content than other clouds. This variability between clouds is much more than the MODTRAN method would lead us to believe. However, spectral character similar to the MODTRAN predictions does seem to exist in real clouds. Therefore, it is reasonable to use the MODTRAN predictions as the cloud spectral response data.

This simple and elegant method has a minor flaw in that there is no accounting for the cloud's impact to its surroundings. That is, a true cloud would actually shadow a portion of the atmosphere from direct sunlight and I do not account

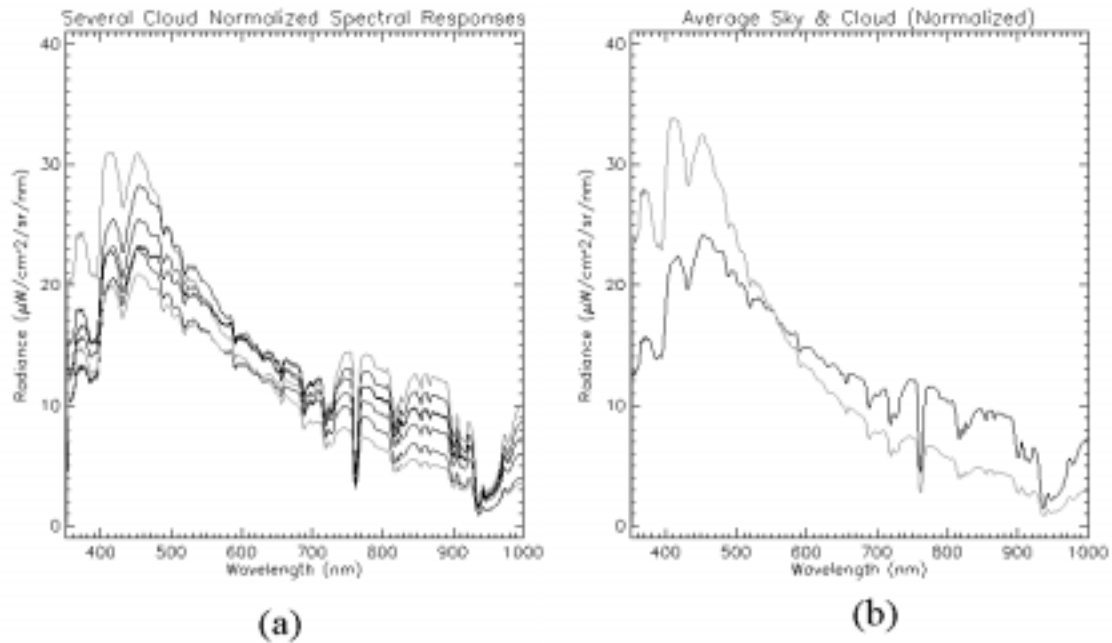


Figure 10: Measured Cloud Spectral Data. These data show several cloud spectral responses (a) and the average cloud along with an average sky spectral response (b). An Analytical Spectral Devices, Incorporated, Full Range Spectralradiometer was used to collect the data. In (a) we can see that the spectral character of clouds has much more variability than the MODTRAN predictions would imply. The data were normalized to have the same integrated radiance in both (a) and (b) which means that some clouds in (a) have less blue and more red than other clouds and vice versa. Averaging all of these yields the darker curve in (b) the represents the average spectral character from the measured clouds.

for that. Also, true clouds would reflect light to the atmosphere causing it to be brighter. I do not account for that either. Finally, the light reflected off of clouds and then off of the atmosphere increases the upwelled radiance as well.

Fortunately, this last interaction may not be a problem. If clouds are far from the line between the sensor and the point on the water surface, they will not attenuate the water leaving radiance nor greatly enhance it (i.e. the “i” type photons in **Figure 2** reflecting off of clouds are negligible). Further, if clouds are in between the point on the surface and the sensor, then the radiance exiting the point may not be important

at all because the cloud contamination is too large and even the current SeaWiFS algorithms flag the data with direct path clouds (Barnes, 1994). However, if a highly reflecting cloud is close to the line between the detector and the point on the water surface then the upwelling radiance along that line *may* be augmented significantly. However, a quick review of the results section will show that the clouds tend to contaminate the remotely sensed data due primarily to reflected light off the water surface. That means that the sensor's line of sight for most of the contaminated data is far from the actual cloud itself.

Summarizing the **RADIATION IN AIR** section, the input radiance to the water's surface,  $L_{\lambda}(\theta, \phi)$ , is calculated using the measured exo-atmospheric solar irradiance along with the MODTRAN generated atmospheric transmittance for the direct sun ( $L_{\lambda}(\sigma, \phi_s)$ ) and MODTRAN for Rayleigh and aerosol components ( $L_{\lambda R}(\theta, \phi)$  and  $L_{\lambda a}(\theta, \phi)$  respectively). The cloud component,  $L_{\lambda C}(\theta, \phi)$ , comes from scaling the MODTRAN generated cloud spectral response by a factor representative of the particular cloud we're trying to model. (If we're modeling a bright cloud, the scale factor would be above 0.25 and if we're modeling a very dark cloud it would be below 0.03.)

## TRANSITION FROM AIR TO WATER

The input to the air-water interface is the magnitude of the radiance entering the water in all directions,  $L_{\lambda}(\theta, \phi)$ , at the point of interest on the surface. To maintain

consistency with the rest of the development,  $L_{\lambda}(\theta, \phi)$  will be renamed to  ${}^+L_{\lambda}^{\downarrow}(\theta, \phi)$  to indicate above the surface (+) heading down ( $\downarrow$ ) at many angles ( $\theta, \phi$ ) with a wavelength dependence ( $\lambda$ ). The output will be the magnitude of the down directed radiance just below the surface in all directions,  ${}^-L_{\lambda}^{\downarrow}(\theta, \phi)$ . The transition through the water relies on the shape of the surface waves and the refractive index of the water. Multiple reflections in the water (between waves) are also considered. Visualizing the output from this module will be a key component to understanding the underwater light field. Methods similar to Figure 6 will be used.

The work of Cox and Munk (1954, 1955, 1956) provides a model of the sea surface for varying wind speeds that is the consistent choice used in the literature. A more recent study by Khristoforov (1992) using a laser inclinometer agrees with the classical Cox and Munk work.

The Cox and Munk work was completed in open ocean waters. A review of the literature to search for a similar model for surface roughness of large lakes and for near shore conditions was not productive. One small study performed by Duntley around the same time as the original Cox and Munk work indicates good agreement with their findings (Duntley, 1954). The other works that were found all refer to the original work by Cox and Munk.

Due to the continuously varying nature of the surface, the underwater light field,  ${}^-L_{\lambda}^{\downarrow}(\theta, \phi)$ , and the reflected light field,  ${}^+L_{\text{ref}}^{\uparrow}{}_{\lambda}(\theta, \phi)$ , are scaled probability density functions (PDFs) in two dimensions. These 2-D PDFs are the result of passing each

input vector,  ${}^+L_{\lambda}^{\downarrow}(\theta_i, \phi_i)$ , through the faceted wave surfaces with orientation and slope defined by the Cox and Munk equations (EQ 5). The probability distribution function for a surface wave to have a slope  $\beta$  with a direction of steepest descent  $\zeta$  (from the downwind direction) was empirically derived by Cox and Munk to be given by EQ 5.

$$p(\beta, \zeta) = (2\pi\sigma_c\sigma_u)^{-1} e^{-\frac{1}{2}(a^2+b^2)} \left[ 1 - \frac{1}{2}c_{21}(a^2-1)b - \frac{1}{6}c_{03}(b^3-3b) + \frac{1}{60}(a^4-6a^2+3) + 0.03(a^2-1)(b^2-1) + \frac{23}{2400}(b^4-6b^2+3) + \dots \right]$$

EQ 5

where  $\sigma_c$  = Cross Wind RMS slope component =  $(0.003 + 0.00192W)^{1/2}$

$\sigma_u$  = Upwind RMS slope component =  $0.056214W^{1/2}$

W = Wind speed

a =  $-\tan(\beta)\sin(\zeta)/\sigma_c$

b =  $-\tan(\beta)\cos(\zeta)/\sigma_u$

$C_{21} = 0.01 - 0.0086W$

$C_{03} = 0.04 - 0.033W$

To get the probability for a specific wave orientation, EQ 5 is quantized in equal  $d\beta$  and  $d\zeta$  steps so that an approximate probability is easily obtained. A full set of  $\beta, \zeta$  orientations combined with the input radiance distribution,  ${}^+L_{\lambda}^{\downarrow}(\theta, \phi)$  and Snell's law,

$$n_1 \sin(\theta_1) = n_2 \sin(\theta_2)$$

EQ 6

yields the PDF of the radiance below the surface heading down,  ${}^-L_{\lambda}^{\downarrow}(\theta, \phi)$ ; replacing Snell's Law with the law of reflection yields the reflected radiance above the surface heading up,  ${}^+L_{\text{ref}}^{\uparrow}(\theta, \phi)$ . However, we must be careful in applying the laws of refraction and reflection for the three dimensional geometry under consideration.

Referring to Figure 11 which illustrates a wave facet defined by  $\beta, \zeta$  oriented within the geometry

defined by Figure 4, the objective is to find the distribution angles above and below

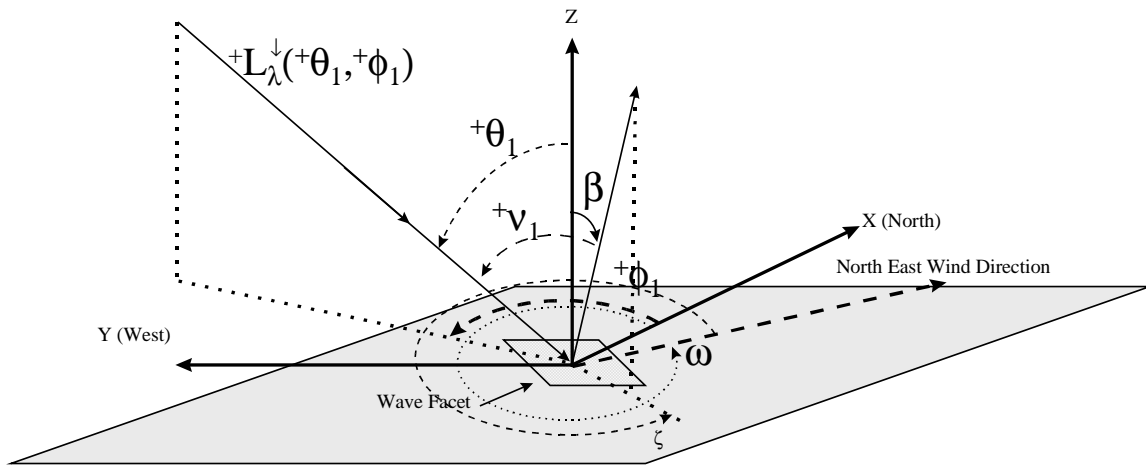


Figure 11: Geometry For A Wave Facet Defined By  $\beta$  And  $\zeta$ . The wind direction from North is defined here as  $\omega$ . A particular input radiance at  $+\theta_1$  and  $+\phi_1$  is illustrated. The objective is to find  $+L_{\lambda}^{\downarrow}(+\theta_1, +\phi_1)$  and  $+L_{\lambda}^{\uparrow}(+\theta_{1ref}, +\phi_{1ref})$  or more directly,  $-\theta_1, -\phi_1, +\theta_{1ref}$ , and  $+\phi_{1ref}$ . Refer to the next two figures.

the surface,  $(+\theta_{1ref}, +\phi_{1ref})$  and  $(-\theta_1, -\phi_1)$ , corresponding to the input radiance angles above the surface  $(+\theta_1, +\phi_1)$  (see Figure 12 and Figure 13). If we define the wind direction from due North as  $\omega$  and the angle between facet normal and the input radiance  $+L_{\lambda}^{\downarrow}(+\theta_1, +\phi_1)$  as  $+v_1$ , then  $+v_1$  and  $-v_1$  can be found using spherical trigonometry and Snell's Law from



$${}^+v_1 = \cos^{-1} \left\{ (\cos({}^+\theta_1) \cos(\beta) + \sin({}^+\theta_1) \sin(\beta) \cos({}^+\phi_1 - \omega - \zeta)) \right\}$$

EQ 7

$${}^-v_1 = \sin^{-1} \left( \frac{n_{air}}{n_{water}} \sin({}^+v_1) \right)$$

EQ 8

To derive the equations for reflection in three dimensions I use the fact that the vector difference between the incident radiance and the reflected radiance must lie on the surface normal with a magnitude given by the law of reflection as  $2\cos(v)$ . This yields three equations (for the three dimensions) and two unknowns ( $\theta_{ref}$  and  $\phi_{ref}$ ) with the angle ambiguity removed using the third equation. Specifically, the reflected declination angle is given by

$${}^+\theta_{1ref} = \cos^{-1} \{ 2 \cos({}^+v_1) \cos(\beta) - \cos({}^+\theta_1) \}$$

EQ 9

and the reflected azimuthal angle is given by either

$${}^+\phi_{1ref} = \cos^{-1} \left\{ \frac{2 \cos({}^+v_1) \sin(\beta) \cos(\zeta + \omega) + \sin({}^+\theta_1) \cos(180^\circ + {}^+\phi_1)}{\sin({}^+\theta_{1ref})} \right\}$$

EQ 10

or

$${}^+\phi_{1ref} = \sin^{-1} \left\{ \frac{2 \cos({}^+v_1) \sin(\beta) \sin(\zeta + \omega) + \sin({}^+\theta_1) \sin(180^\circ + {}^+\phi_1)}{\sin({}^+\theta_{1ref})} \right\}$$

EQ 11

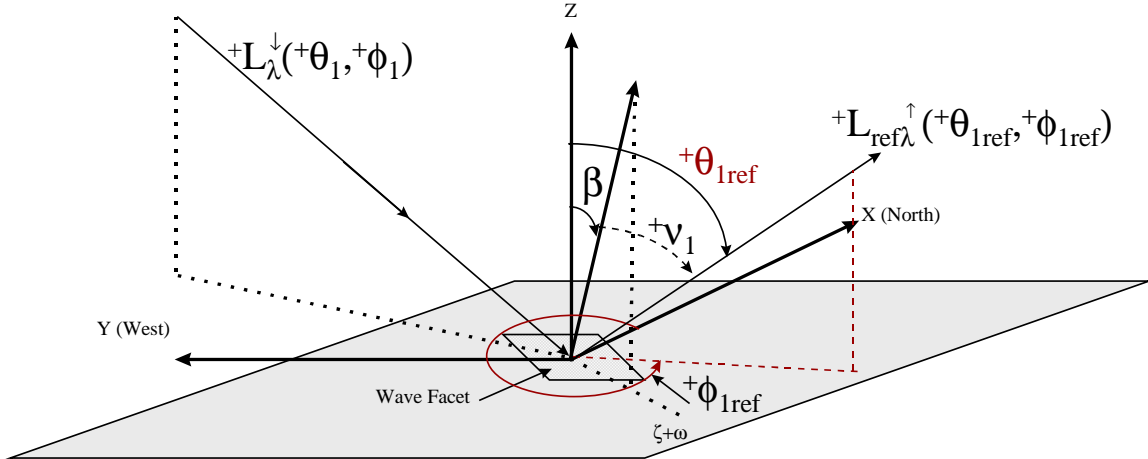


Figure 12: Geometry of Reflection off a Wave Facet. Here the reflection angles,  $+\theta_{1ref}$  and  $+\phi_{1ref}$ , correspond to the specific input angles,  $+\theta_1$  and  $+\phi_1$ , and the wave facet slope and direction angles,  $\beta$  and  $\omega + \zeta$  according to the development in the text. The magnitude of the reflected radiance,  $+L_{ref\lambda}^{\uparrow}(+\theta_{1ref}, +\phi_{1ref})$ , is obtained by multiplying the input radiance magnitude by the reflection coefficient to get  $|+L_{ref\lambda}^{\uparrow}(+\theta_{1ref}, +\phi_{1ref})| = \rho |+L_{\lambda}^{\downarrow}(\theta_1, \phi_1)|$  where  $\rho$  is a function of  $+v_1$ .

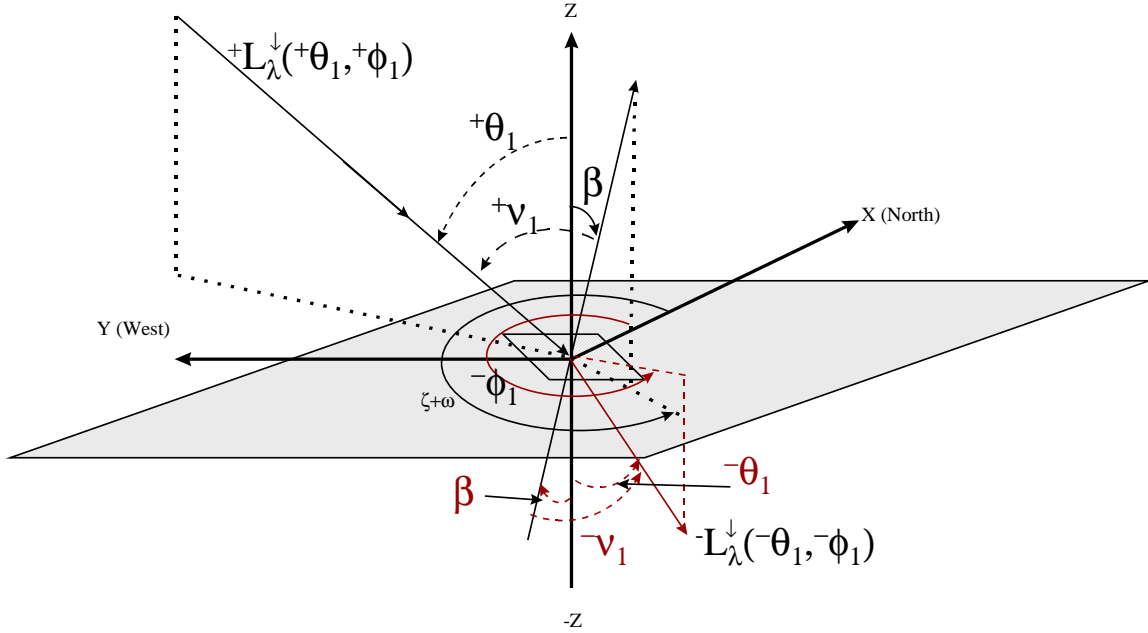


Figure 13: Geometry Of Refraction Through A Wave Facet.. Here the refraction angles,  $-\theta_1$  and  $-\phi_1$ , correspond to the specific input angles,  $+\theta_1$  and  $+\phi_1$ , and the wave facet slope and direction angles,  $\beta$  and  $\zeta + \omega$  according to the development in the text. The magnitude of the refracted radiance,  $-L_{\lambda}^{\downarrow}(\theta, \phi)$ , is obtained by multiplying the input radiance magnitude by one minus the reflection coefficient to get  $-L_{\lambda}^{\downarrow}(\theta, \phi) = (1 - \rho) +L_{\lambda}^{\downarrow}(\theta, \phi)$  where  $\rho$  is a function of  $+\theta_1$ .

Due to the ambiguity associated with the arccosine and arcsine, both EQ 10 and EQ 11 are used to determine the particular  $+\phi_{1\text{ref}}$  required. (By using the arguments of EQ 10 and EQ 11 the correct quadrant can be easily determined. Given the correct quadrant, the ambiguity is removed.)

The magnitude of the reflected radiance is simply a matter of multiplying the magnitude of the input radiance by the reflection coefficient in the  $+v_1$  direction. The reflectance of the air/water interface can be readily computed from the Fresnel Reflectance formulae

$$\rho_{\perp} = \frac{\sin^2(\theta_i - \theta_r)}{\sin^2(\theta_i + \theta_r)}$$

EQ 12

$$\rho_{||} = \frac{\tan^2(\theta_i - \theta_r)}{\tan^2(\theta_i + \theta_r)}$$

EQ 13

and

$$\rho = 0.5 \frac{\sin^2(\theta_i - \theta_r)}{\sin^2(\theta_i + \theta_r)} + 0.5 \frac{\tan^2(\theta_i - \theta_r)}{\tan^2(\theta_i + \theta_r)}$$

EQ 14

The three reflection coefficients represent perpendicular polarization ( $\rho_{\perp}$ ), parallel polarization ( $\rho_{||}$ ), and random polarization ( $\rho$ ). Random polarization is assumed throughout the development of the model. The angles in EQ 12 through EQ

14 are for the incident ( $\theta_i$ ) and refracted ( $\theta_r$ ) angles, which correspond to  ${}^+v_1$  and  ${}^-v_1$  respectively.

With the above development, we can compute the magnitude and the direction of the reflected radiance from the air/water interface for each input radiance vector and for each input wave facet. Further, we can compute the probability of each wave facet orientation with the added input of wind speed and direction. Therefore, each input radiance vector will produce a probability distribution of reflected radiance vectors. Summing the distributed reflected radiance vectors derived from each input radiance vector and each wave facet will yield the total reflected radiance vector distribution. A similar development is required for the refracted radiance.

The magnitude of the refracted radiance through a given wave facet is found using  $(1-\rho)$  times the magnitude of the input radiance for the  ${}^+v_1$  incident angle. That is the easy part. I derived the refraction angles,  ${}^-\theta_1$  and  ${}^-\phi_1$ , using a three-dimensional form of the law of refraction and similar logic as with the reflection equations. Specifically, using the fact that the vector difference between the incident radiance and the product of the index of refraction and the refracted radiance must lie on the facet normal, I derived the following relationships:

$${}^-\theta_1 = \cos^{-1} \left\{ \frac{k_w \cos(\beta) - \cos({}^+\theta_1)}{-n_w} \right\}$$

EQ 15

and

$$^{-}\phi_1 = \cos^{-1} \left\{ \frac{k_w \sin(\beta) \cos(\zeta + \omega) + \sin(^{+}\theta_1) \cos(180^\circ + ^{+}\phi_1)}{n_w \sin(^{-}\theta_1)} \right\}$$

EQ 16

and to again remove the ambiguity,

$$^{-}\phi_1 = \sin^{-1} \left\{ \frac{k_w \sin(\beta) \sin(\zeta + \omega) + \sin(^{+}\theta_1) \sin(180^\circ + ^{+}\phi_1)}{n_w \sin(^{-}\theta_1)} \right\}$$

EQ 17

In the above equations,  $n_w$  is the index of refraction in the water normalized to the index of refraction of the air (which is assumed to be 1) and  $k_w$  is the magnitude of the unitized difference vector along the facet normal and is found from

$$k_w = \cos(^{+}\nu_1) - n_w \cos \left( \sin^{-1} \left( \frac{\sin(^{+}\nu_1)}{n_w} \right) \right)$$

EQ 18

Similar to the reflected radiance distribution,  $^{+}L_{\text{ref}}^{\uparrow}(\theta, \phi)$ , the below the surface downward radiance distribution,  $^{-}L_{\lambda}^{\downarrow}(\theta, \phi)$ , becomes a matter of summing all contribution combinations from the above water downward distribution,  $^{+}L_{\lambda}^{\downarrow}(\theta, \phi)$ , and the probability of wave orientation,  $p(\beta, \zeta)$  scaled by one minus the reflection coefficient

(refracted) or by the reflection coefficient (reflected) and the square of the index of refraction<sup>4</sup>:

$$^{-}L_{\lambda}^{\downarrow}(\theta, \phi) \Big|_{binned} = \sum_i \sum_j \sum_k \sum_l {}^{+}L_{\lambda}^{\downarrow}(\theta_i, \phi_j) p(\beta_k, \zeta_l) (1 - \rho_{ijkl}) n_w^2$$

EQ 19

and

$$^{+}L_{ref\lambda}^{\uparrow}(\theta, \phi) \Big|_{binned} = \sum_i \sum_j \sum_k \sum_l {}^{+}L_{\lambda}^{\downarrow}(\theta_i, \phi_j) p(\beta_k, \zeta_l) (\rho_{ijkl})$$

EQ 20

Note that each set of i, j, k, and l will correspond to a particular ( $^{-}\theta, ^{-}\phi$ ) and ( $^{+}\theta_{ref}, ^{+}\phi_{ref}$ ) but the total contribution to each ( $^{-}\theta, ^{-}\phi$ ) and ( $^{+}\theta_{ref}, ^{+}\phi_{ref}$ ) direction will come from several sets of i, j, k, and l combinations. The  $|_{binned}$  nomenclature results. Note also that EQ 19 and EQ 20 refer only to the source radiance to the water coming from the sky, sun, and clouds and hitting the water surface. (The full radiative transfer equations are discussed later.)

For this development, the wind speed and direction are the only inputs that effect the facet model. One tacit assumption in the literature is that the surface wave distribution is the same temporally and spatially. In fact, the Cox and Munk work would not apply if the ergodic assumption is not true; however, the assumption is

---

<sup>4</sup> The  $n^2$  comes from the fundamental theorem of radiometry: “the radiance divided by the square of the index of refraction is constant along any path”. See Wyatt (1978) or Mobley (1994).

most likely correct. In Duntley's measurements that agree with Cox and Munk, he used an electrical measurement system of closely spaced wires to directly measure the wave slopes versus wind speed over time (Duntley, 1954). Agreement between Duntley's measurements and Cox and Munk makes the ergodic assumptions very plausible.

The index of refraction could also be a variable input to the model. I do not expect the index of refraction to greatly affect the overall radiance reaching the sensor for "normal" values of  $\sim 1.33$  or so. Though the index of refraction for natural waters is both known and a function of wavelength as in Figure 12, the affects of added chlorophyll, suspended minerals and dissolved organic material is unknown. Therefore, a nominal value of  $n=1.33$  is used in the simulations performed here.

### **Some Anomalous Cases**

Now that the geometry is defined for both reflected and refracted radiance, shadowing and multiple reflections can be addressed. These cases can best be visualized using the defined and derived geometry while highlighting some anomalous points.

For instance, when the reflection declination angle,  $\theta_{\text{ref}}$ , is greater than  $90^\circ$ , the reflected radiance MUST reflect back into the air/water interface. The reflected radiance in that case is added to the input radiance at  $\theta = (\theta_{\text{ref}} - 90^\circ)$  and  $\phi = \phi_{\text{ref}}$  to arrive at a new input radiance from that direction.

# Water Refractive Index

No Salt; T = 0 to 30 C

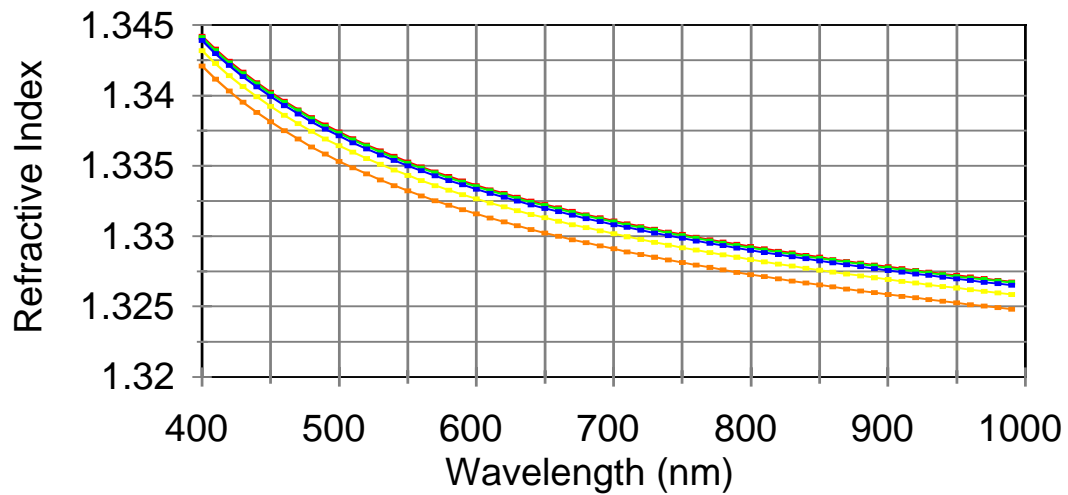


Figure 14: Refractive index for fresh water as a function of wavelength for temperatures ranging between 0°C and 30°C. Data generated using Quattro Pro 7 with equations of Quan and Fry (1995).

Another anomaly occurs when  $\theta_{v1}$  is greater than  $90^\circ$ . For  $\theta_{v1} > 90^\circ$ , the input radiance is more than  $90^\circ$  away from the normal to the wave facet for the radiance and wave facet under question. In other words, the wave facet is shadowed to that radiance vector. For that case, the input radiance vector is not used.



The next anomaly occurs when  $\theta_1$  is greater than  $90^\circ$ . This is an extremely rare condition. In words,  $\theta_1 > 90^\circ$  means that the refracted radiance enters that water at an angle that greatly increases the probability of exiting the water. This brings some difficult choices: the photons enter the water, travel some distance, and, if they don't scatter off anything, exit the water, but how far do they travel and what are the orientations of the exit facets? The distance and orientation of the exit facet require more information than provided by EQ 5.

One possible solution is to assume that all photons that produce  $\theta_1 > 90^\circ$  immediately impinge on the water/air interface (from the water side) for facets oriented with the same probabilities as given by EQ 5. This solution is reasonable considering the small number of photons for which it would apply. Note that to get  $\theta_1 > 90^\circ$  we need to have  $\beta > 90^\circ$  which immediately eliminates at least  $\frac{1}{2}$  the geometry due to shadowing alone. The probability of having a wave facet with  $\beta > 90^\circ$  is also very small (Cox and Munk, 1956) and, finally, the act of refraction further reduces the number of photons that would produce  $\theta_1 > 90^\circ$ . With all the caveats and reduced probabilities, it is safe to assert that the number of photons producing  $\theta_1 > 90^\circ$  is vanishingly small.

Two other anomalies occur that would normally be difficult to track. They are:

- (1) photons that fail to reach a wave facet due to shadowing by another wave facet and
- (2) reflected photons with  $\theta_{1ref} < 90^\circ$  that re-enter the air/water interface due to localized geometry (See Figure 15). For both of these cases, the number of photons

under consideration is relatively small. (Note that the geometry indicated in Figure 15 is greatly exaggerated to illustrate the anomalous conditions. In reality, such peaks do not normally exist in surface waves per Cox and Munk, 1956.)

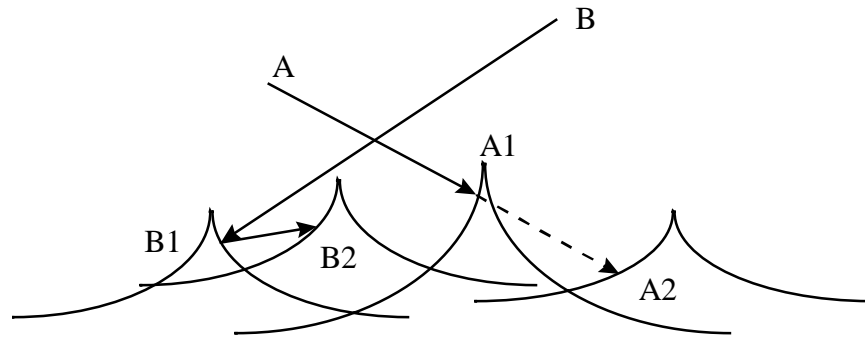


Figure 15: Facet-to-facet Shadowing and Multiple Reflection. Photons coming from direction of “A” fail to impinge on point A2 due to shadowing at A1 and photons that come from direction of “B” reflect at B1 and re-enter the water at B2 even though the reflection declination angle is less than  $90^\circ$ . The sea surface wave geometry is greatly exaggerated for illustration purposes.

The probability for wave orientation given in EQ 5 does not give the entire wave shapes, nor can the shapes be derived from the original Cox and Munk work (Cox and Munk, 1956). To accurately assess the numbers of photons that are facet-to-facet shadowed or reflected requires knowledge of the overall wave shape that we do not possess. We have a method empirically derived by Neumann and reported by Preisendorfer (1976, Vol. 4) to relate the wave elevation probabilities to wind speed, but we do not have any correlation data for the wave slopes. North (1990) provides a way (via multiple assumptions and simplifications) to estimate the shape of the

surface waves. However, North's purposes did not require the accuracy needed for radiance transfer and using his results would simply trade one set of unknown information for another.

If we examine the effects of ignoring facet-to-facet shadowing, we find that the resulting radiance at the sensor would be slightly over estimated because the radiance reaching point A2 in Figure 15 would be slightly over estimated. Further, we note that most of the facet-to-facet shadowing will occur for input radiance coming from very high declination angles ( $+\theta_1$  approaching  $90^\circ$ ). (Remember that self-shadowing is already addressed.) EQ 5 tells us that most of the surface waves have fairly low slopes (almost all are less than  $45^\circ$ ) which pushes the  $+\theta_1$  even closer to  $90^\circ$  for facet-to-facet shadowing. Combining this with the Fresnel reflectance formula we find that most of the radiance we neglect by neglecting facet-to-facet shadowing is reflected radiance and the reflection angles would be near the horizon. Therefore, I conclude that neglecting facet-to-facet shadowing slightly overestimates the radiance reaching the sensor, but the overestimate is extremely small for sensor angles away from the horizon.

Using the same development, we find that omitting photons that are facet-to-facet reflected with  $+\theta_{1ref} < 90^\circ$  will slightly underestimate and rearrange the radiance reaching the sensor. Not addressing this facet-to-facet reflection would give a reflected radiance in the  $+\theta_{1ref}$  that is slightly too large and slightly underestimate the radiance in some other  $+\theta_{7ref}$  direction due to the double reflection at point B2 in Figure

15. The radiance entering the water at point B2 would also be underestimated and, therefore, so is the radiance exiting the water. The directional information is difficult to even localize without more knowledge than is given in the studies by Cox and Munk, but it appears as though the underestimated radiance is most likely spread over a large angular sector that would tend to reduce the error in any one direction. The anomaly also occurs very rarely so the uncertainty is further reduced. Yet, the affect remains unknown and (via mental methods) seems to reach a maximum for mid-level incidence angles.

That conclusion seems to agree with a study completed by Preisendorfer and Mobley (1986). Their numerical study via Monte Carlo methods indicated that multiple reflections occur between 5 and 10 percent of the time for incident angles between about  $50^\circ$  and  $80^\circ$  and wind speeds above 10 m/sec. These multiple reflections act to redistribute the radiance (Mobley, 1994). However, the study did not delineate between  $+\theta_{1\text{ref}} > 90^\circ$  and  $+\theta_{1\text{ref}} < 90^\circ$ . Nor did it give probability distributions for reflection angles; it only gave probabilities for multiple reflections.

Repeating their work would get one step closer to the actual radiance distributions above and below the water. However, Preisendorfer and Mobley did not have any correlation data for wave slopes and they assumed complete randomness. Correlation data for wave slopes is not found in the literature to date. The completely random assumptions will certainly provide data, but the data may not be accurate.

Even so, the inaccuracies seem to be limited for the anomalous cases discussed above. Therefore, the work of Preisendorfer and Mobley (1986) as repeated and coded by Mobley (1995) as part of the Hydrolight computer code is used here to pass the light through the air/water interface.

## UNDER WATER REFLECTION MODELS

Several underwater reflection models have been reported in the literature including the works that were previously cited (Gordon, 1975; Kirk, 1984; Kirk, 1991; Morel, 1993; Bukata, 1981; Mobley, 1994; and Jerome, 1988). Bukata (1995) summarizes most of the referenced work and explains the problems and advantages associated with each. He goes further to address several areas of concern specifically related to the Laurentian Great Lakes. One Monte Carlo based code used by Jerome (1996) was seriously considered for the main underwater module in this study for two reasons. The reasons are: (1) it was used by Jerome and Bukata to help derive the suspended materials (SM) impact results previously discussed; and (2) it applies an easily understood method (Monte Carlo) in a straightforward manner. One drawback to Jerome's code is that it was designed for light entering the water from only one direction. I would have had to modify the code to take advantage of the three-dimensional radiance field below the water surface.

A second concern comes from the lack of good quality measurements in the literature for optical cross sections of suspended minerals, chlorophyll-a, and/or dissolved organic matter (DOM) for wavelengths outside the 400nm-750nm region.

Bukata (1981, #1) defines these three groups as generic components of natural waters and he and Jerome build their models using the three groups. At the May 1998 International Association of Great Lakes Research conference, one of the main points in the remote sensing unit was the lack of good optical cross sections (Bukata, 1998). Others in the field echo these statements (Pegau, 1995; Maffione, 1997).

A third concern comes from the fact that at each point (or “cell”) the input light is traveling in all directions. The size of the “point”, or cell, will depend on the eventual sensor in question (1.13 km x 1.13 km for SeaWiFS; Barnes, 1994). Adjacent cells will certainly impact the light under each cell; there will be more impact at the edges and deeper beneath the cells. For large cells such as SeaWiFS, the effect is probably negligible; for smaller cells such as our in-house MISI sensor (with spatial resolution on the order of a few feet) the effect could be major in a cell by cell basis. Since most remote sensing systems have resolutions much larger than a few feet, ignoring the adjacent cell effect should not be a problem. Also, even for small MISI type cells, we could assume that the radiance scattered in would be the same as the radiance scattered out and, thereby, ignore the cell size.

The essence of the underwater model is that light travels through the water until it reflects off of materials within the water or until it is totally absorbed. The further the light travels, the more it is absorbed. Reflection off of material will alter the direction of the light. Sometimes multiple reflections are required before the light exits the water; often the light does not exit the water before being totally absorbed.

With all of the reflecting and direction changes occurring, Monte Carlo methods certainly lend themselves to this environment and they are easy to understand.

Another promising technique (and the one eventually adopted) is the method of invariant imbedding detailed in Preisendorfer, 1976, (Vol. 4) and explained by Mobley (1994). Invariant imbedding's greatest assets are that the entire radiance field,  ${}^{\pm}L_{\lambda}^{\uparrow}(\theta, \phi)$ , can be calculated with one sweep using matrix methods and that statistical residual errors normally found with Monte Carlo methods are non-existent.

The invariant imbedding technique used in the Hydrolight code by Mobley (1995) is not as easy to understand as Monte Carlo methods. In fact, Mobley's textbook, "Light and Water", (1994) is almost entirely devoted to setting up and describing the invariant imbedding solution method for the radiative transfer equations under water. I will not repeat that here. The Hydrolight code is enough of an industry standard and its mathematical techniques are documented well enough to use it, with slight modifications, for the underwater module (Schott, 1998). The modifications that were required are covered in the appendices. Hydrolight numerically solves the radiance transfer equations given in EQ 21 through EQ 24 below.

$$\begin{aligned}
 {}^+L_{\lambda}^{\uparrow}(\theta, \phi) = & \int_{\Xi_+} {}^+L_{\lambda}^{\uparrow}(\theta', \phi') r((\theta', \phi') \rightarrow (\theta, \phi)) d\Omega(\theta', \phi') \\
 & + \int_{\Xi_-} {}^+L_{\lambda}^{\downarrow}(\theta', \phi') r((\theta', \phi') \rightarrow (\theta, \phi)) d\Omega(\theta', \phi') \quad \text{for } (\theta, \phi) \text{ in } \Xi_+
 \end{aligned}$$

EQ 21

$$\begin{aligned}
{}^{-}L_{\lambda}^{\downarrow}(\theta, \phi) &= \int_{\Xi_{-}} {}^{-}L_{\lambda}^{\uparrow}(\theta', \phi') r((\theta', \phi') \rightarrow (\theta, \phi)) d\Omega(\theta', \phi') \\
&\quad + \int_{\Xi_{+}} {}^{+}L_{\lambda}^{\downarrow}(\theta', \phi') t((\theta', \phi') \rightarrow (\theta, \phi)) d\Omega(\theta', \phi') \quad \text{for } (\theta, \phi) \text{ in } \Xi_{-}
\end{aligned}$$

EQ 22

$$\begin{aligned}
\cos(\theta) \frac{d {}^{-}L_{\lambda}^{\uparrow\downarrow}(z; \theta, \phi)}{dz} &= - {}^{-}L_{\lambda}^{\uparrow\downarrow}(z; \theta, \phi) + \tilde{S}(z; \theta, \phi) + \\
&\quad \varpi_o(z) \int_{\Xi_{\pm}} {}^{-}L_{\lambda}^{\uparrow\downarrow}(z; \theta', \phi') \tilde{\beta}(z; (\theta', \phi') \rightarrow (\theta, \phi)) d\Omega(\theta', \phi') \\
&\quad \text{for } (\theta, \phi) \text{ in } \Xi_{\pm}
\end{aligned}$$

EQ 23

$$\begin{aligned}
{}^{-}L_{\lambda}^{\uparrow}(bottom; \theta, \phi) &= \int_{\Xi_{-}} {}^{-}L_{\lambda}^{\downarrow}(\theta', \phi') r_{bottom}((\theta', \phi') \rightarrow (\theta, \phi)) d\Omega(\theta', \phi') \\
&\quad \text{for } (\theta, \phi) \text{ in } \Xi_{+}
\end{aligned}$$

EQ 24

With a little explanation, EQ 21 through EQ 24 seem obvious. EQ 21 and EQ 22 refer to the radiance at the water surface. In EQ 21, the spectral radiance above the surface heading up in all directions is equal to the radiance transmitted through the surface from below plus the radiance reflected off of the surface from above. EQ 22 refers to the radiance just below the water surface heading down. It says that the spectral radiance below the water surface heading down in all directions is equal to the radiance reflected off of the surface from below plus the radiance transmitted through the surface from above. The two integrals in each of EQ 21 and EQ 22 are over the associated hemispheres. The second integral in EQ 21 is analogous to EQ 20



and the second integral in EQ 22 is analogous to EQ 19. However, here they are included as part of the complete radiance transfer equations.

More nomenclature is required for EQ 23. It refers to the spectral radiance in all directions at a particular optical depth,  $z$ , below the water surface. EQ 23 equates the change in radiance at depth  $z$  with the total radiance into the depth plus the radiance generated at the depth from internal sources  $\tilde{S}$  less the radiance exiting the depth. Here all directions and both hemispheres  $\updownarrow$  (upward and downward) are used.

Finally, EQ 24 refers to the radiance coming from the bottom and equates the spectral radiance heading up in all directions to the radiance reflected off of the bottom. We assume that there are no sources at or below the bottom.

Hydrolight solves these equations numerically without the statistical residual left from Monte Carlo methods. As previously stated, Hydrolight is used in this study for the underwater module. Hydrolight also performs the radiance transfer through the water surface for both into and out of the water. However, Hydrolight employs a wind direction invariant form of Cox and Munk's probability distribution function found in EQ 5.

### **What is in the Water**

With the decision to use Hydrolight and its invariant imbedding technique for the underwater radiative transfer solution method, the next step is to determine what is in the water to absorb and scatter light. The following sections will describe the

substances found in many natural water bodies and give the concentrations reported in the literature. Together with the absorption and scattering cross sections, the concentrations will provide the absorption coefficient,  $a(\lambda)$ , and scattering coefficient,  $b(\lambda)$  via<sup>5</sup>

$$a(\lambda) = \sum_{i=1}^n C_i a_i(\lambda) = \text{Absorption Coefficient}$$

$$b(\lambda) = \sum_{i=1}^n C_i b_i(\lambda) = \text{Scattering Coefficient}$$

EQ 25

where the  $C_i$  are the concentration levels, the  $a_i$  are the absorption cross sections and the  $b_i$  are the scattering cross sections.

Natural water bodies are comprised of an innumerable amount of substances. Knowing how these substances absorb and scatter electromagnetic energy is paramount to solving radiative transfer within water bodies. Yet the sheer number of aquatic constituents requires a simplification. Bukata (and many others) categorize these substances into five groups: pure water, dissolved salts and gases, dissolved organic matter, chlorophyll-a, and suspended matter.

---

<sup>5</sup> In practice the absorption and scattering coefficients are actually measured along with the concentrations to derive the specific cross sections. Modeling changes in the absorption and scattering coefficients, however, is often done via changes in concentrations while maintaining the fixed specific cross sections.

Dissolved salts and gases most significantly absorb or scatter light in the ultraviolet region and are normally omitted from simulations at longer wavelengths. Thus, “n” in EQ 25 is simply 4.

Excluding pure water, we're left with three groups of substances: Dissolved Organic Matter; Suspended Matter; and Chlorophyll-a. Most of the following information (and all the numeric values) comes from Bukata (1995) or sources referenced there.

### **Dissolved Organic Matter**

Dissolved organic matter (DOM) comes from two primary sources: within the water and from outside the water. The indigenous DOM is primarily the byproduct of photosynthesis by phytoplankton and the remains of decomposing (or decomposed) phytoplankton. The decomposition of the aquatic life also results in humic and fulvic acids, which create a yellowish hue. This is sometimes referred to as gelbstoff or simply “yellow substance” in the literature. DOM in open oceans is primarily the indigenous variety. (Bukata, 1995)

Nearer to shore or for lakes, another source of DOM comes from the land. Surface run-off and river discharges introduce a wide variety of DOM into the water. Further, near shore and in lakes the nutrient levels tend to be higher which, in turn, increases the indigenous DOM due to higher metabolic rates for the phytoplankton. Both sources result in higher DOM concentrations in lakes and near shore than they are in the open ocean. For instance, the literature reports various concentrations in

different inland lakes from ~1-2 gC/m<sup>3</sup> to as high as 20-25 gC/m<sup>3</sup> while open ocean levels tend to be ~0.001-0.005 gC/m<sup>3</sup> (Bukata, 1995). (The DOM concentration is reported in grams of Carbon per volume; Carbon normally makes up approximately half the DOM by weight.) Lake Ontario levels have been determined by Bukata (1980) to be around 2 gC/m<sup>3</sup>.

Even these concentration levels are still much lower than dissolved salts. However, the DOM affects light in the visible spectrum and is, therefore, important. DOM absorbs light, but the scattering coefficient is generally accepted to be small enough to ignore. Studies have shown that the absorption coefficient follows an exponential decay with increasing wavelength with a decay slope,  $s$ , between 0.011 and 0.021 (Carder, 1989 via Bukata, 1995). (The decay is from a reference point generally at 400nm or 440nm.)

### **Suspended Matter**

Suspended matter is a mix of many types of organic and inorganic material. It ranges from living and dead phytoplankton, zooplankton, and other aquatic organisms to clay, sand, and silt from land-based sources. Also included are human wastes and byproducts (including pollution); precipitated atmospheric aerosols (including volcanic ash); and specific elements, usually in the form of oxides, hydroxide, or carbonates, such as iron, magnesium, silicon, calcium, and aluminum. (The hydroxides and carbonates tend to be localized phenomenon that only exist under specific circumstances.) (Bukata, 1995)

The specific form and composition of suspended matter is spatially, temporally, and geographically variable. We can simplify the variability somewhat by removing some of the components. In fact, to get Bukata's five groups, he already has essentially removed phytoplankton (and all algae) to form the chlorophyll-a group (see below).

It is believed that zooplankton do not contribute much to the overall absorption and scattering coefficients of the water volume due to their low concentrations. Also, since zooplankton consume phytoplankton, they may have absorption and scattering characteristics very similar to phytoplankton. It seems safe to ignore the zooplankton as a special category and account for their absorption and scattering contributions via phytoplankton (chlorophyll-a) or suspended minerals. (Bukata, 1995)

Bacterioplankton cannot be ignored. Bacterioplankton can be subdivided into two groups: those with color and those without color. The colorless bacterioplankton do not absorb visible energy, but they most likely scatter visible energy. The colored subgroup, however, are referred to as bacterial chlorophylls a, b, c, and d due to their resemblance to the pigments in phytoplankton (Bukata, 1995).

The suspended minerals (sand, silt, clay...) are the most important and most troublesome of the constituents in suspended matter. (The two terms are sometimes interchanged because of this.) They can range from (3-4)  $\mu\text{m}$  in diameter (clay) to (130-250)  $\mu\text{m}$  (sand) (Adamenko via Bukata, 1995). Concentrations range from (0.02-0.17)  $\text{g}/\text{m}^3$  in the open ocean (Jerlov, 1976) to as high as (0.1-12.0) $\text{g}/\text{m}^3$  in some lakes

(Bukata, 1995). Lake Ontario concentrations have been reported at  $(0.2-8.9)\text{g/m}^3$  (Bukata, 1981 #1) They are the most troublesome because of the high scattering coefficients for these particles.

### **Chlorophyll-a**

Chlorophylls, carotenoids, and phycobilins are the three basic types of photosynthesizing agents. They are present in varying degrees in all species of phytoplankton and, therefore, algae. (Algae can be seaweed or pond scum or any of several species in between.) They are also primary ocean color constituents.

Chlorophyll itself is separated into four varieties designated a, b, c, and d. Of these, chlorophyll-a is by far the most prominent. (All green algae contain chlorophyll-a, but not all contain b and c. Of those that do contain b or c, the a to b and a to c ratios are ~3:1.) Knowing the location and concentration of chlorophyll-a would lead to locations and concentrations of phytoplankton.

Knowing those concentrations over a wide scale could lead to more accurate worldwide energy budgets for tracking global warming and/or climate and seasonal changes. In a less global sense, we could also extrapolate fish school locations with the phytoplankton knowledge. For these reasons, chlorophyll-a concentrations and locations are some of the primary reasons for water quality measurements on a large scale. (Bukata, 1995)

Unfortunately, absorption and scattering cross-sections of chlorophyll-a vary along with the alga species in the region as well as the age and cell structure and even the previous amount of light absorbed by the algae. Fortunately, the spectral shape of the various species, ages, structure, and history absorption and scattering cross-sections tends to stay roughly the same with peaks at ~440nm and ~675nm. That means that we may be able to determine that chlorophyll-a is present, but we may error on the exact concentration. Data for the Great Lakes seems to point to slightly higher than average absorption cross-sections for algae species found there. (Bukata, 1995)

Now that we've covered the four main components of natural waters (Pure Water, DOM, SM, and Chlorophyll-a) and their typical concentration levels, EQ 25 can be re-written and simplified to

$$a(\lambda) = a_w(\lambda) + C_{DOM}a_{DOM}(\lambda) + C_{SM}a_{SM}(\lambda) + C_{chl}a_{chl}(\lambda)$$

$$b(\lambda) = b_w(\lambda) + C_{SM}b_{SM}(\lambda) + C_{chl}b_{chl}(\lambda)$$

EQ 26

The final step is to determine the optical cross sections,  $a_{DOM}(\lambda)$ ,  $a_{SM}(\lambda)$ ,  $a_{chl}(\lambda)$ ,  $b_{SM}(\lambda)$ , and  $b_{chl}(\lambda)$ . The literature contains several examples. The particular water body in question tends to have its own variety of chlorophyll-a and suspended matter so the optical cross sections tend to be different. Further, the values reported in the literature tend to range in wavelength from 400nm to 700nm because that is

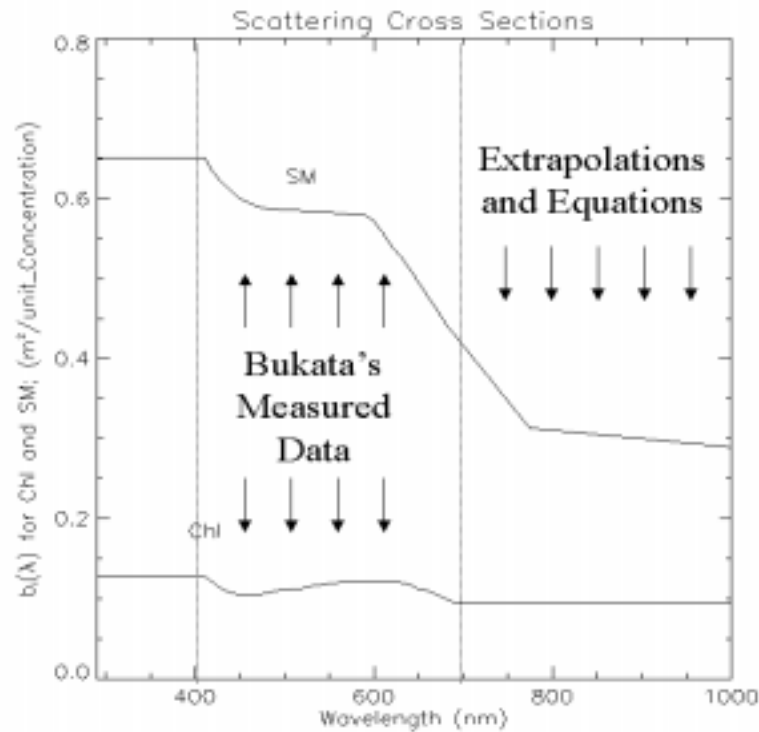


Figure 16: Scattering Cross Sections for Chlorophyll-a content and Suspended Mineral content. Curves are from Bukata (1995) using measured data (400nm to 690nm) and analytical equations (290nm to 400nm and 700nm to 1000nm)

typically where water-viewing sensors operate. For my purposes, I need data above 700nm and would like the range to run from 290nm to 1000nm. Bukata (1995) reports cross section curves for Lake Ontario waters in the 400nm to 690nm range and provides numerical equations for the key cross sections outside of that region. I used Bukata's cross section data in this study. The cross sectional curves used are given in Figure 16 through Figure 19.

These data comprise most of the input to the Hydrolight code to describe the water body. Other water parameters include internal sources such as



bioluminescence, fluorescence, and Raman scattering. These sources are modeled in Hydrolight (and modified in my version of Hydrolight), but they did not play a major role in the cloud impact analysis.

The output from the underwater module will be the upward traveling radiance in all directions,  $\bar{L}_\lambda^\uparrow(\theta, \phi)$ , at the point of interest re-entering the water/air interface. (Note that Jerome's code currently provides a volume reflectance factor for a single input angle and would need several changes to provide the  $\bar{L}_\lambda^\uparrow(\theta, \phi)$  required.) This output is then the input to the light traveling back through the water/air interface.

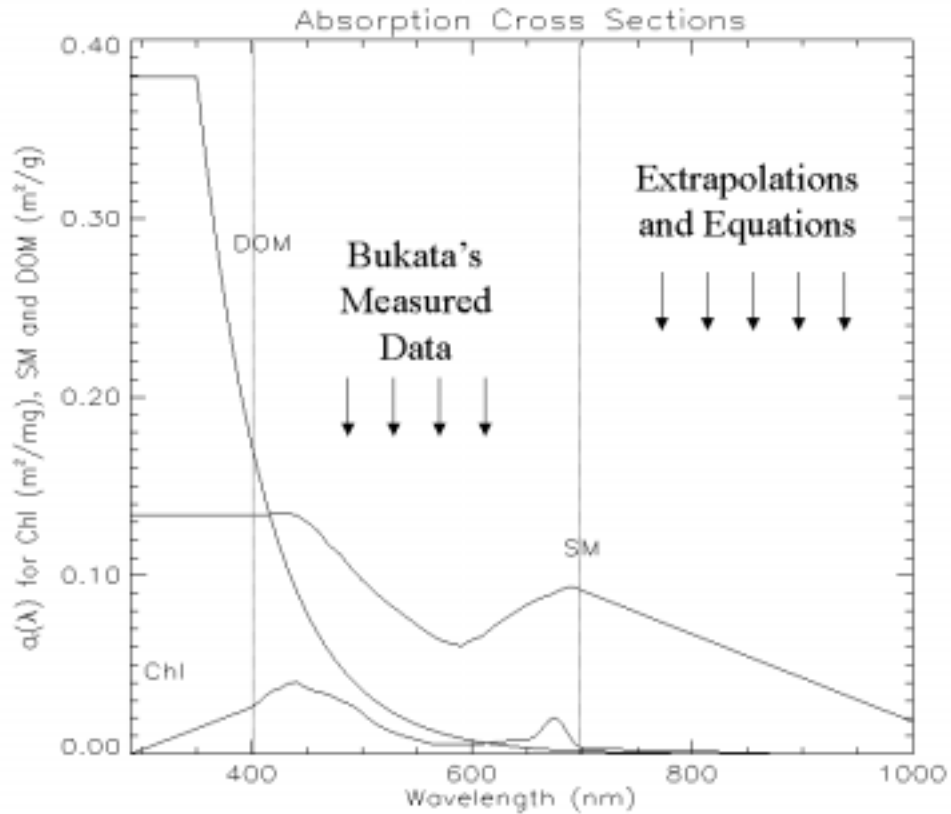


Figure 17: Absorption Cross Section curves from Bukata (1995) data (400nm to 690nm) and analytical equations (below 400nm and 700nm to 1000nm).

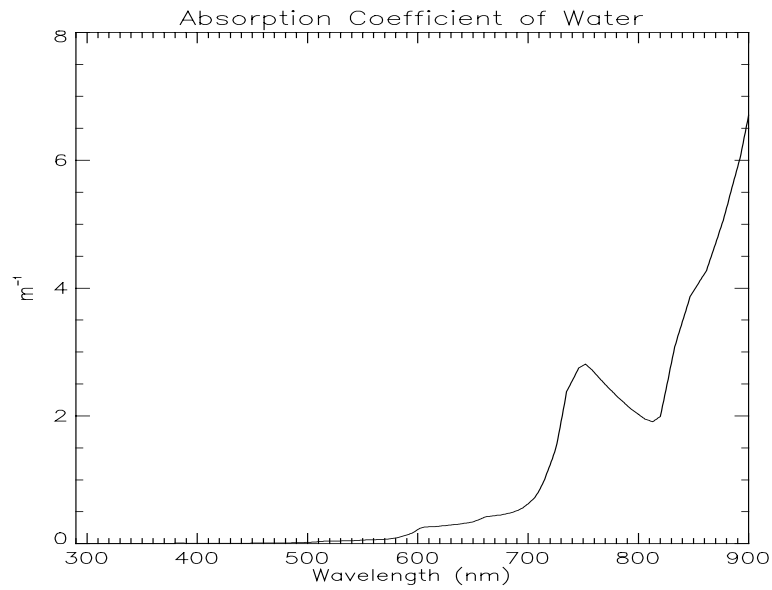


Figure 18: Absorption Coefficient for water. Note that the wavelength range is truncated at 900nm due to a peak in absorption near 914nm that would render the rest of the data non-viewable. However, we can still see large absorption coefficients above 700nm. Data from Pope (1997).

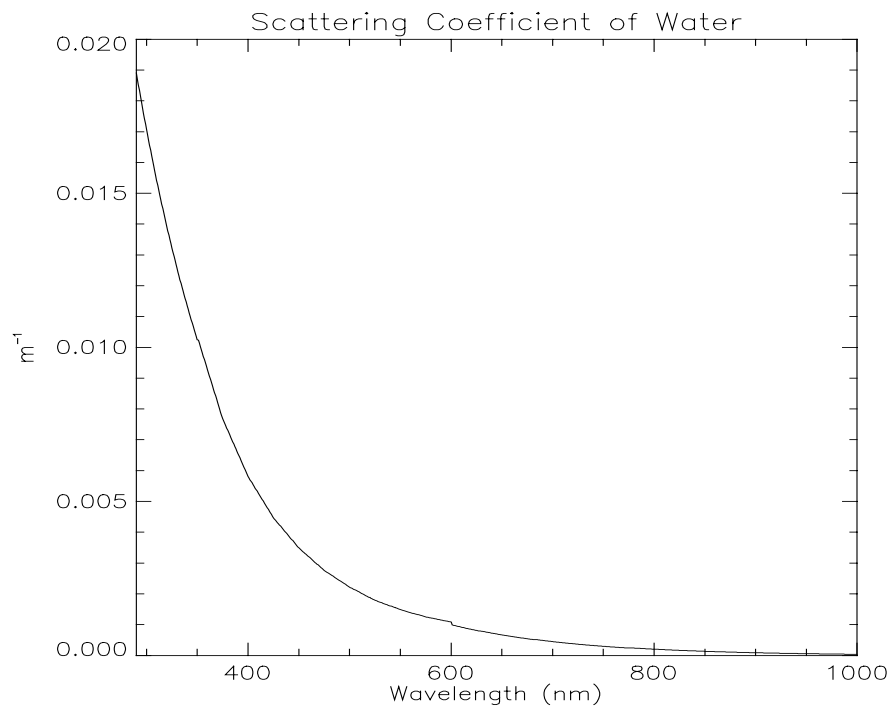


Figure 19: Scattering Coefficient for water.

## TRANSITION FROM WATER TO AIR

The model for this module is simply a reverse of the previous **Air/Water Interface** section; finding  ${}^+L_{\lambda}^{\uparrow}(\theta, \phi)$  from the radiance distribution  ${}^-L_{\lambda}^{\uparrow}(\theta, \phi)$  is a matter of applying the Cox and Munk probability distribution equations (EQ 5) and Snell's Law (EQ 6) to  ${}^-L_{\lambda}^{\uparrow}(\theta, \phi)$ . Only the angles toward the detector,  $\theta_d$  and  $\phi_d$ , are of interest, so only  ${}^+L_{\lambda}^{\uparrow}(\theta_d, \phi_d)$  is required. However, obtaining  ${}^+L_{\lambda}^{\uparrow}(\theta, \phi)$  for several angles is a simple matter at this point. Therefore, the radiance distribution above the water surface in all directions,  ${}^+L_{\lambda}^{\uparrow}(\theta, \phi)$  is calculated. The module is further simplified by the previous selection of Hydrolight as the underwater code. Hydrolight performs this calculation and provides the radiance above the water surface heading up in all directions,  ${}^+L_{\lambda}^{\uparrow}(\theta, \phi)$ .

One complication arises due to possible self-shadowing or self-hiding of the wave. If the wave is oriented such that it physically blocks part of itself from the detector, then a portion of  ${}^+L_{\lambda}^{\uparrow}(\theta_d, \phi_d)$  is lost. In fact, a *particular* portion of  ${}^+L_{\lambda}^{\uparrow}(\theta_d, \phi_d)$  is lost that comes from the particular portion of the wave that is blocked. Determining the  $\beta_{\text{block}}$  and  $\zeta_{\text{block}}$  again requires the wave slope correlation data that is not found in the Cox and Munk probability distribution given in EQ 5. Fortunately, for small sensor declination angles the shadowing is negligible (Preisendorfer, 1986)

## PROPAGATION TO THE SENSOR

The final module in the model is propagation from the water surface, through the atmosphere, to the sensor. The radiance exiting the water is combined with the radiance reflected off the water ( $L_{\text{ref}}$  in **Figure 2** found in EQ 20) and the upwelled radiance ( $L_{\text{path}}$  in **Figure 2** and  $+L_{\lambda R}^{\uparrow}(\theta, \phi) + +L_{\lambda a}^{\uparrow}(\theta, \phi)$  in our current nomenclature) found from another series of MODTRAN runs. The radiance leaving the surface must be propagated to the sensor through the attenuating atmosphere.

The attenuation of the radiance between the water surface and the sensor comes from the transmission coefficient,  $\tau$ , and can be obtained in the original MODTRAN runs that produced  $L_{\lambda}(\sigma, \phi_s)$ ,  $L_{\lambda R}(\theta, \phi)$  and  $L_{\lambda a}(\theta, \phi)$  or on the upwelled radiance series. Though both sets of transmission coefficient values are equal for a space based sensor, the appropriate  $\tau$  to use comes from the upwelled radiance series of MODTRAN runs. Obviously,  $\tau$  is a function of orientation angle and is more appropriately termed  $\tau(\theta, \phi)$ . For a given atmospheric mix of water vapor, aerosols, ..., the  $\tau(\theta, \phi)$  is invariant as a function of  $\phi$ . Therefore,  $\tau$  is only a function of the declination angle and is termed  $\tau(\theta)$ .

## RADIATIVE TRANSFER MODEL SUMMARY

The end-to-end radiative transfer model has five major modules for the five regions of radiance transfer: air, air-to-water, water, water-to-air, and air again. The first module, air, has two sub-modules for the radiance due to the sun and sky (from MODTRAN) and for the radiance due to local clouds. The inputs to this module are

the properties of the air (aerosols and water vapor present and their concentrations and distributions); the cloud location, size, and extinction coefficient distributions and scattering phase functions; and the sun location. The output from the first module is  ${}^+L_{\lambda}^{\downarrow}(\theta, \phi)$  which is the input to the subsequent modules.

A modified form of Hydrolight accomplishes all transitioning through the air/water interface and radiance transfer within the water. The input to these sections includes the radiance distribution above the water surface,  ${}^+L_{\lambda}^{\downarrow}(\theta, \phi)$ , the wind speed, and the properties of the DOM, SM, and Chlorophyll-a in the water. These properties include the concentrations, optical cross sections, and changes in concentration levels as a function of water depth. Other parameters for the water module include internal sources such as Raman scattering, DOM fluorescence, bioluminescence, and chlorophyll fluorescence.

The final propagation to the detector uses transmission coefficients and upwelling radiance calculated in another set of MODTRAN runs using the same atmospheric inputs.

The total inputs required are the sun and detector locations, the properties of the atmosphere, the type and location of the clouds, the properties of the water, and the wind speed. The final output is the radiance at the detector for the location of interest on the water surface. However, the radiance distribution at (above) the water surface and below the water surface is also available. With this modular approach,

the radiance at these locations due to each individual module is also available for study.

## Chapter 3

### SEAWIFS DERIVED CHLOROPHYLL CONTENT

Let's begin with a quick look at the SeaWiFS algorithms. The sensor senses a total radiance,  $L_{t\lambda}$ , in each of the 8 bands. The algorithms first turn this radiance into a reflectance,  $\rho_t(\lambda)$ , defined as (McClain, 1995)

$$\rho_t(\lambda) = \pi L_{t\lambda} / E_0 \cos(\sigma) \quad \text{EQ 27}$$

where  $E_0$  is the exoatmospheric solar irradiance and  $\sigma$  is the pixel centered solar zenith angle. The total reflectance is made up of several parts:

$$\rho_t(\lambda) = \rho_r(\lambda) + \rho_a(\lambda) + \rho_{ra}(\lambda) + \tau \rho_{wc}(\lambda) + T \rho_g(\lambda) + \tau \rho_w(\lambda) \quad \text{EQ 28}$$

which are the Rayleigh, Aerosol, Rayleigh/Aerosol interaction, white cap, sun glint, and water leaving components respectively. The Rayleigh and white cap components are removed via estimates of the wind speed and the surface atmospheric pressure (McClain, 1995). The sun glint component is neglected by looking away from locations that have a high sun glint (the SeaWiFS sensor tilts  $\pm 20^\circ$  to avoid sun glint). We are left with

$$\rho_t(\lambda) - \rho_r(\lambda) - \tau\rho_{wc}(\lambda) = [\rho_a(\lambda) + \rho_{ra}(\lambda)] + \tau\rho_w(\lambda)$$

EQ 29

The absorption coefficient for pure water is so high at NIR wavelengths (see Figure 18 ) that we can normally set  $\rho_w(\text{NIR})=0$ . The SeaWiFS algorithms use this to find  $\rho_a(\lambda)+\rho_{ra}(\lambda)$  at two different NIR wavelengths (765nm and 865 nm) and then use these two values with several (N) atmospheric predictions to determine the single scattering aerosol components,  $\rho_{as}(765\text{nm})$  and  $\rho_{as}(865\text{nm})$  (Gordon, 1994). There is a linear relationship, found empirically, between  $\rho_{as}$  and  $\rho_a+\rho_{ra}$ , but the linear relationship is different for each type of atmospheric makeup and each angle of observation and each wavelength (Wang, 1994). The single scattering aerosol component is needed to find

$$\varepsilon(\lambda_1, \lambda_2) = \frac{\rho_{as}(\lambda_1)}{\rho_{as}(\lambda_2)}; \quad \varepsilon(765\text{nm}, 865\text{nm}) = \frac{\rho_{as}(765\text{nm})}{\rho_{as}(865\text{nm})}$$

EQ 30

The value of  $\varepsilon(765\text{nm}, 865\text{nm})$  is used to find  $\varepsilon(\lambda, 865\text{nm})$  via another empirically derived linear relationship (Gordon, 1994), and then  $\rho_{as}(\lambda)$  is determined. Also, the value of  $\varepsilon(765\text{nm}, 865\text{nm})$  found above will fall in between two of the  $\varepsilon_i(765\text{nm}, 865\text{nm})$ s determined from the N atmospheres used in the predictions. These two atmospheres (in the same ratios) are used to find  $\rho_a(\lambda)+\rho_{ra}(\lambda)$  once  $\rho_{as}(\lambda)$  is known. Now, finally, we can subtract out  $\rho_a(\lambda)+\rho_{ra}(\lambda)$  and divide by the transmittance,  $\tau$ , to find  $\rho_w(\lambda)$ . Samples of the empirically derived curves are found in Figure 20.



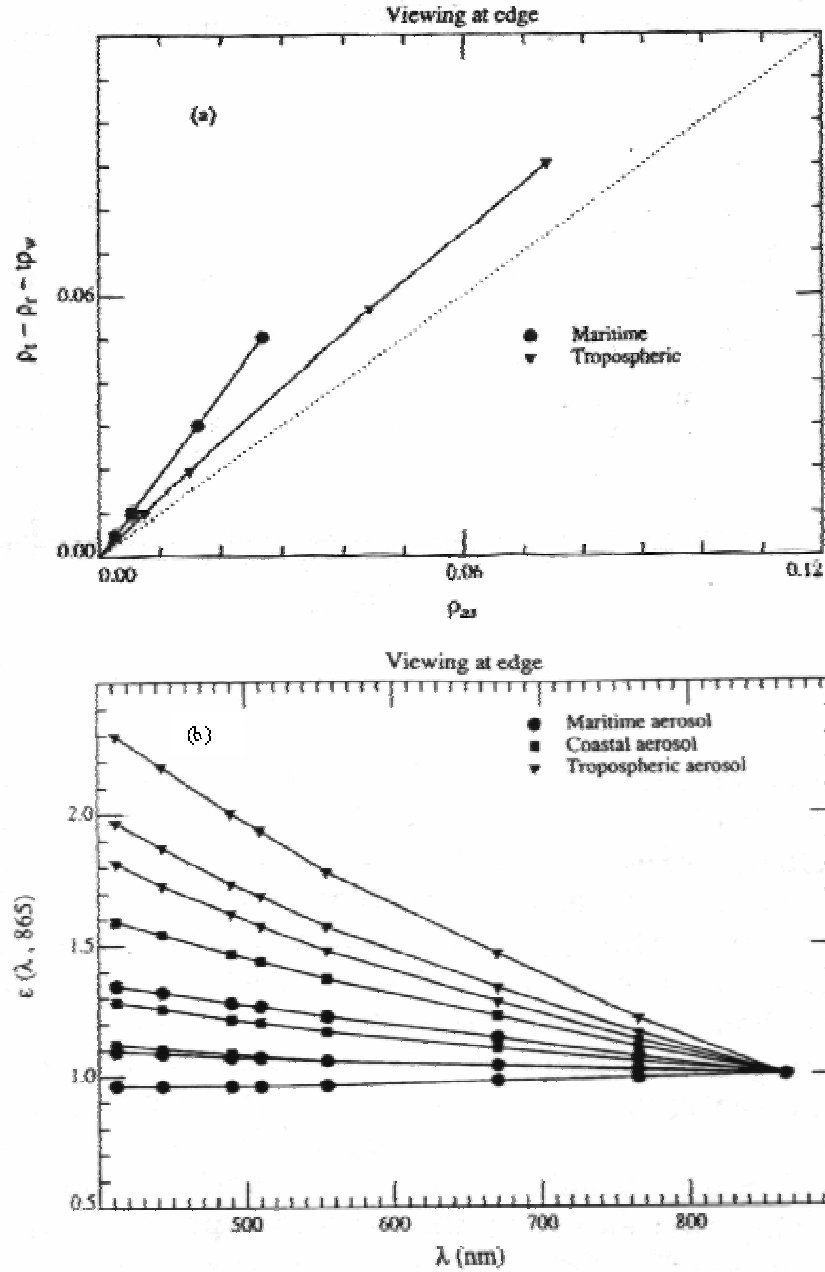


Figure 20: Two Sample Empirical Relationships Scanned from Gordon (1994). In (a) the relationship between  $\rho_a(443\text{nm}) + \rho_{Ra}(443\text{nm})$  and  $\rho_{as}(443\text{nm})$  at the edge of the SeaWiFS scan is presented for two different atmospheres. The relative humidity level for the tropospheric atmosphere was set at 70% and for the Maritime atmosphere it was set at 98%. Each SeaWiFS view angle, wavelength and atmosphere would use a different curve such as the two found in (a). In (b),  $\epsilon(\lambda, 865\text{nm})$  is plotted as function of  $\lambda$  for 9 specific atmospheres (the three listed with RH of 70%, 90%, and 98%) at the edge of the SeaWiFS scan. A separate relationship is used for each atmosphere and each look angle. Few examples such as these are found in the literature.

The chlorophyll-a content is determined from the reflectance for bands 3 and 5 (centered at 490nm and 555nm respectively) using another empirically derived formula. McClain (1995) terms the formula “Ocean Color 2” or simply OC2 and gives the chlorophyll-a content as

$$Chlor\_a = 10^{(0.3410 - 3.001R + 2.811R^2 - 2.041R^3)} - 0.40 \quad (\mu g / l) \quad \text{EQ 31}$$

$$\text{where } R = \log_{10} \left( \frac{\rho_w(\lambda = 490nm)}{\rho_w(\lambda = 555nm)} \right) \quad \text{EQ 32}$$

However, Acker (1998) reports that the SeaWiFS algorithm for chlorophyll-a content has changed. Though the exact coefficients are not published, recent correspondence indicates that the algorithm will remain the same and the coefficients in the algorithm changed to yield (Hooker and Firestone, 1999)

$$Chlor\_a = 10^{(0.2974 - 2.2429R + 0.8358R^2 - 0.0077R^3)} - 0.0929 \quad (\mu g / l) \quad \text{EQ 33}$$

We may expect that both the algorithm and the coefficients used in EQ 32 and EQ 33 will be periodically updated to reflect new ground truth data results.

Notwithstanding the uncertainties in the empirical algorithms, we note three additional possible problems with this process:

- (1) We assumed that we could look away from highly reflecting areas when we set  $\rho_g=0$ . Therefore, glint from clouds,  $\rho_{cg}$ , is not included.
- (2) We assumed that the water's high absorption coefficient for NIR overshadowed the scattering coefficient(s) of material in the water and from the surface reflection component.
- (3) The empirically derived equations do not account for source radiance spectrum flattening which may result from large "white" clouds reflecting energy to the water.

Problems (1) and (2) will most likely have the largest impact on the chlorophyll-a determination. The flatter spectral response from the clouds, however, is a very real phenomenon that must be considered. The average ratio between  $+L_{\lambda=765nm}^{\downarrow}(\theta, \phi)$  and  $+L_{\lambda=865nm}^{\downarrow}(\theta, \phi)$  for the input cloudless sky ranges from 1.23 for rural atmospheres to 1.3 for very clear tropospheric atmospheres, while the same cloud ratio is very close to 1.0. The  $+L_{\lambda=490nm}^{\downarrow}(\theta, \phi)$  and  $+L_{\lambda=555nm}^{\downarrow}(\theta, \phi)$  ratio is even worse. It ranges from 1.24 to 1.5 for the input cloudless skies and is still very close to 1.0 for the cloud spectral response. (These data are based on several MODTRAN runs and include the averages over the bands as defined by SeaWiFS.)

Problem (2) above is highly suspended matter dependent. The suspended matter problem is not studied as part of this effort. Dr. Robert Bukata and colleagues are attacking the issue directly for Lake Ontario waters. Concisely,  $\rho_w(765nm) \neq 0$

$\neq \rho_w(865\text{nm})$  as is assumed in the algorithm because substantial concentrations of suspended minerals combined with the scattering cross section cause some light to exit the water even in the NIR. Obviously, higher concentrations of suspended matter (as found in the Laurentian Great Lakes) will produce even higher scattering coefficients, which, in turn, deviates  $\rho_w$  further from 0. Until the Bukata work is complete or another study is performed, we can only speculate as to the impact of the suspended matter on  $\rho_w(765\text{nm}) \neq 0 \neq \rho_w(865\text{nm})$  and the associated atmospheric subtraction.

It is reasonable to assume that the water leaving reflectance ratio for  $\lambda=765\text{nm}$  and  $\lambda=865\text{nm}$ ,  $\rho_w(765)/\rho_w(865)$ , is greater than the atmospheric ratio,  $(\rho_a(765\text{nm})+\rho_{ra}(765\text{nm})) / (\rho_a(865\text{nm})+\rho_{ra}(865\text{nm}))$ , when suspended matter is present. That is because the spectral absorption coefficient of water increases for increasing wavelength while the spectral scattering coefficient for suspended matter tends to decrease with increasing wavelength. That means that the error in finding  $\rho_a(765\text{nm})+\rho_{ra}(765\text{nm})$  is larger than the error in finding  $\rho_a(865\text{nm})+\rho_{ra}(865\text{nm})$  by an unknown amount (due to  $\rho_w(765) > \rho_w(865)$ ). Using the SeaWiFS algorithms, the errors propagate to  $\rho_{as}(765\text{nm})$  and  $\rho_{as}(865\text{nm})$  and then to  $\epsilon(765\text{nm},865\text{nm})$ . (The error in  $\rho_{as}(765\text{nm})$  is greater than the error in  $\rho_{as}(865\text{nm})$  and both are too large. Unfortunately, it is not possible to determine whether  $\epsilon(765\text{nm},865\text{nm})$  is too large or too small.) With an inflated  $\epsilon$ , the determined atmospheric contribution for bands 3 and 5,  $\rho_a(490\text{nm})+\rho_{ra}(490\text{nm})$  and  $\rho_a(555\text{nm})+\rho_{ra}(555\text{nm})$ , will be inflated with band 3

error greater than band 5 error. This translates to calculating  $\rho_w(490\text{nm})$  and  $\rho_w(555\text{nm})$  that are too small with  $\rho_w(490\text{nm})$  having the most error. Again, unfortunately, we cannot speculate on the affect this error has on the ratio between  $\rho_w(490\text{nm})$  and  $\rho_w(555\text{nm})$  without more knowledge about both the error and the original ratio. We can say that if the ratio between  $\rho_w(490\text{nm})$  and  $\rho_w(555\text{nm})$  is reduced, then the SeaWiFS algorithms would predict more chlorophyll-a in the water than it would without the suspended matter and if the ratio is increased the opposite would occur. (See Figure 21). This speculation can be confirmed with the same computer model used in the cloud study.

Obviously, adding suspended matter to the water will not appreciably change the atmospheric contamination to the data, but the SeaWiFS algorithms will have an error in the aerosol determination due to the non-zero water leaving radiance at NIR. It is ultimately the non-zero NIR water leaving radiance that causes most of that error and we see the same error caused by clouds. Additional contributions come from the increased scattering in the visible region due to the suspended matter.

For clouds, we have two problems to worry about. The biggest expected impact is from cloud glint. SeaWiFS tilts to avoid the sun glint so that  $\rho_g = 0$ . However, it is possible for clouds to reflect sun light in non-predictable (a priori) directions, producing cloud glint that SeaWiFS does not avoid. Clouds will make  $\rho_{cg} > 0$ . In this case, the questions to be asked are: “When is  $\rho_{cg}$  increased enough to impact SeaWiFS derived volume reflectance and chlorophyll-a levels? What cloud locations,

concentrations, and distributions affect the data and by how much? How “bright” do they need to be?”

Answering these questions by varying the types, locations, concentrations, distributions, and “brightness” of clouds in a controlled way is the essence of this study. In each case, the model calculates the radiance at the sensor and the water leaving radiance in each band. From there, the SeaWiFS algorithms are employed to determine the impact of the clouds on the SeaWiFS derived products.

The sources of the impact to the SeaWiFS products are the non-zero  $\rho_{cg}$  and the flatter or “white” cloud spectral response. Both sources of error will affect both the 765nm/865nm atmospheric subtraction algorithm and the 490nm/555nm chlorophyll-a determination algorithm. In fact, for the atmospheric subtraction algorithm, the chain of events leading to errors in the SeaWiFS derived chlorophyll-a content is exactly the same as those previously discussed for the suspended matter case with one exception: the  $\rho_w(765nm)/\rho_w(865nm)$  ratio (due to clouds and the non-zero  $\rho_{cg}$ ) is often less than the atmospheric ratio. (Recall that the discussion for the suspended matter case started with a greater water leaving radiance ratio due to the suspended matter.)

The empirically derived chlorophyll-a formula (EQ 32) is affected similarly by the flattened spectrum. If we assume, for the moment, that we can find the true volume reflectance values,  $\rho_w(490nm)$  and  $\rho_w(555nm)$  then we can determine the expected impact of the clouds on the chlorophyll-a content while ignoring the affect of the atmosphere. In fact, it becomes a simple matter.

Clouds have a flatter spectrum (essentially a 1:1 ratio between 490nm and 555nm) so at lower true chlorophyll levels (when the water leaving 490nm to 555nm ratio is greater than 1:1), the ratio in EQ 32 would be smaller with clouds present then it would be without clouds present. For instance, with minimal chlorophyll and very blue water,  $\rho_w(490)/\rho_w(555)$  may be something like 1.5. Adding in a cloud to the scene with its flatter 1.0 ratio would reduce  $\rho_w(490)/\rho_w(555)$  to, say 1.45. A smaller ratio yields a higher calculation for chlorophyll content.

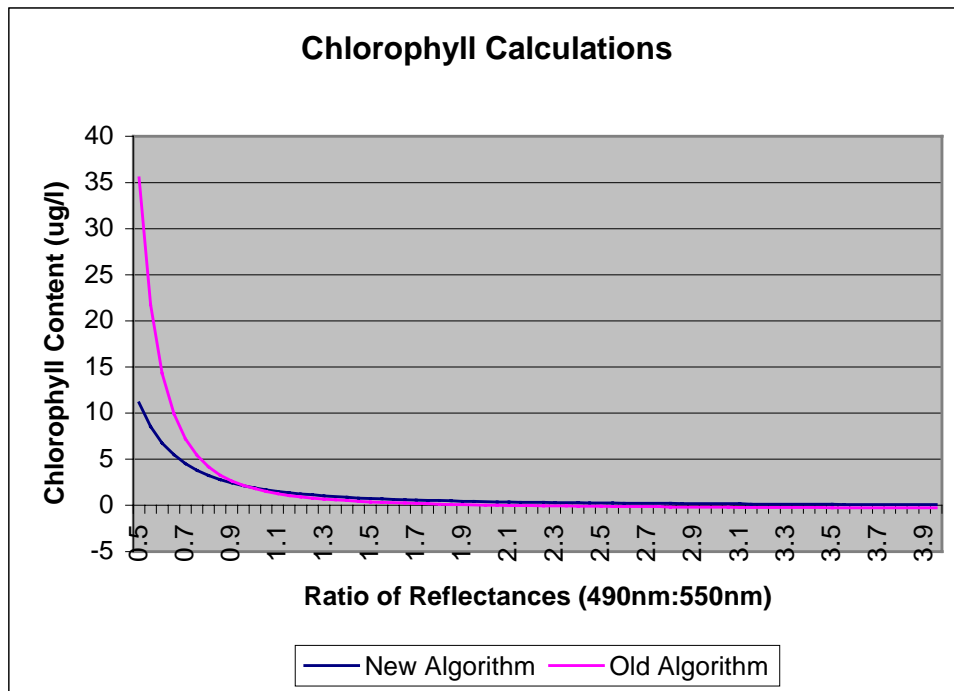


Figure 21: Affect of changing the reflectance ratio on the calculated chlorophyll content. For waters that are more blue than green, the  $\rho_w(490nm): \rho_w(555nm)$  ratio is greater than one. For waters that are more green than blue, the ratio is less than one

At higher true chlorophyll levels (green water and  $\rho_w(490)/\rho_w(555)$  around 0.8 for instance), the flatter spectrum caused by the clouds would tend to increase the  $\rho_w(490\text{nm})$  to  $\rho_w(555\text{nm})$  ratio (to, say, 0.83) and an underestimate of the chlorophyll content results. These conclusions apply using both EQ 31 and EQ 33 as illustrated in Figure 18.



## *Chapter 4*

### **SEAWIFS CLOUD STUDY SCOPE**

HydroMod is the radiative transfer code created for this effort by combining MODTRAN and Hydrolight together with other capabilities previously discussed (see Appendix I and II). The flexibility built into HydroMod makes it applicable to any water body for any wind speed and atmosphere and any sun location or any detector at any wavelength (from 290nm to 1000nm). The cloud impact characterization problem, however, can be scoped by only considering the input parameters that apply for the Laurentian Great Lakes and the SeaWiFS sensor. Physical laws also apply to further limit the scope of the study.

The reflectance of the air/water interface can be readily computed from the Fresnel Reflectance formulae repeated here

$$\rho_{\perp} = \frac{\sin^2(\theta_i - \theta_r)}{\sin^2(\theta_i + \theta_r)}$$
EQ 34

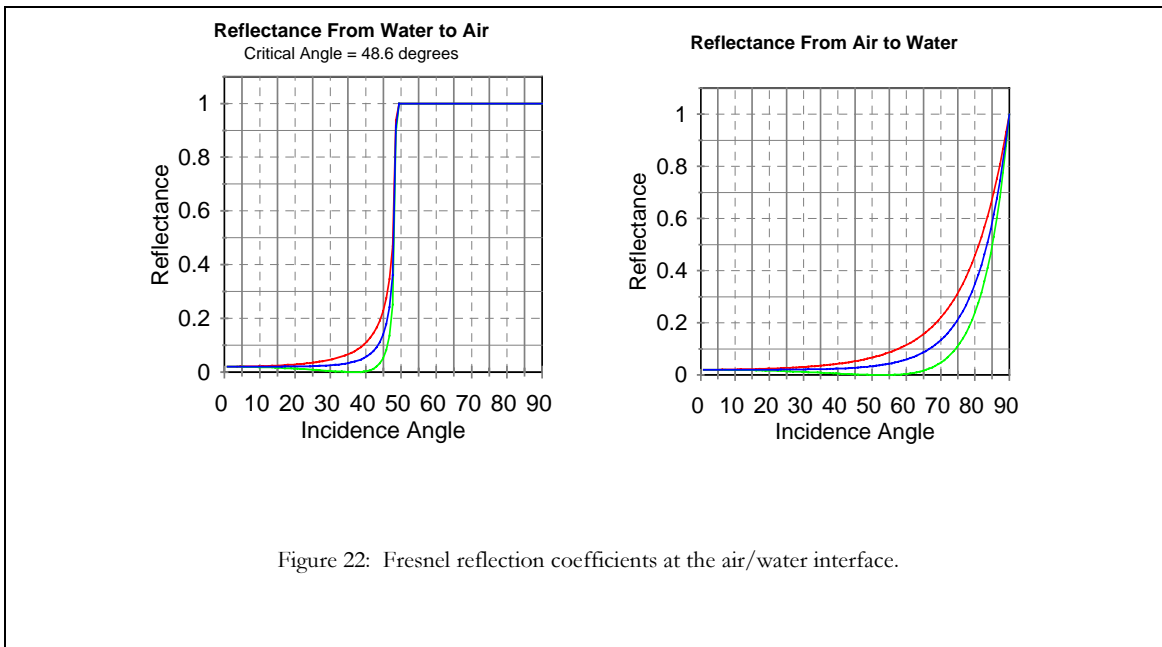
$$\rho_{||} = \frac{\tan^2(\theta_i - \theta_r)}{\tan^2(\theta_i + \theta_r)}$$
EQ 35

and

$$\rho = 0.5 \frac{\sin^2(\theta_i - \theta_r)}{\sin^2(\theta_i + \theta_r)} + 0.5 \frac{\tan^2(\theta_i - \theta_r)}{\tan^2(\theta_i + \theta_r)}$$

EQ 36

which yield the graphs found in Figure 22. The three reflection coefficients represent perpendicular polarization ( $\rho_{\perp}$ ), parallel polarization ( $\rho_{\parallel}$ ), and random polarization ( $\rho$ ).



For light hitting the air/water interface from above ( $+L_{\lambda}^{\downarrow}(\theta, \phi)$ ) the reflectance coefficient is very high (20%) for incidence angle above  $\theta = 75^{\circ}$  or so. Thus, a good upper limit for the sun location,  $\sigma$ , would be  $\sigma \leq 75^{\circ}$ .

Noting the location of the Laurentian Great Lakes relative to the earth/sun system, we see that the highest  $\sigma$  would be found at local noon at the summer solstice at or near the southern most point of the lakes. The Tropic of Cancer is at  $23^{\circ} 27'$

north latitude and the southern end of Lake Erie is at 41°22' north latitude. Ignoring the radius of the earth with respect to the sun-earth distance yields an absolute minimum  $\sigma$  of 17°55' (including the full geometry would increase  $\sigma_{\min}$  slightly). Therefore, the sun input angles are limited to  $18^\circ \leq \sigma \leq 75^\circ$ . Using an even more limited range may be prudent; for most of the time over most of the Great Lakes,  $\sigma_{\min}$  is considerably greater than 18°. The sun's azimuth angle,  $\phi_s$ , is similarly limited and is a function of location of the point of interest and the declination angle.

The atmospheric aerosol models will be limited to only those applicable over the Great Lakes region. Specifically, the Maritime, Urban and Rural atmospheres with varying visibility will be used. The "standard" atmosphere for the cloud study is the MODTRAN standard Maritime atmosphere with 23 Km visibility and a sun location at 41° declination. The Maritime atmosphere is chosen so that the results found here will apply to world-wide coastal zones in addition to the Great Lakes.

Similarly, the water quality models (including optical cross sections and concentrations) used by Bukata and Jerome (1995 through 1998) are used since they are characteristic of the Great Lakes. These data and the extensions above 700nm and below 400nm wavelengths are given in Figure 16 through Figure 19.

Nominal prevailing winds in the Great Lakes region tend toward 5 to 15 knots (2.57 to 7.72 m/sec) in an east-northeast direction (various web based sources). Wind speeds in excess of 18 knots (9.27 m/sec) introduce enough whitecaps that they impact the water's reflectance values too much (Gordon, 1997). Since the objective is to

characterize the affect of clouds, it is reasonable to minimize the expected white caps. Therefore, wind speeds are limited to 0 m/sec through 9 m/sec. This limitation has the added affect of eliminating most of the facet-to-facet scattering that occurs when the light first enters the water (Preisendorfer and Mobley, 1986).

The SeaWiFS sensor has a maximum scan angle of  $58.3^\circ$  and can tilt  $\pm 20^\circ$  from nadir to avoid the direct sun glint (Barnes, 1994). For a flat earth, this would limit  $\theta_d$  to less than  $60.4^\circ$ . Using an earth mean radius of 6371km, the limit on  $\theta_d$  for a spherical earth is  $74.95^\circ$ . The azimuth angle,  $\phi_d$ , is not limited ( $0^\circ \leq \phi_d < 360^\circ$ ).

The cloud models used in the study are described in ***Radiance from Clouds*** and Figure 9. The MODTRAN derived cloud family of spectral response curves condensed to the one cloud spectral response curve in Figure 9 is used. The brightness, size and shape, location, and cloud:(cloud+sky) ratio are also variable. The brightness values associated with the cloud spectral curve vary from 0.30 for the bright clouds down to 0.0001 for the darkest clouds. These brightness values range outside the observed range in both the MODTRAN calculations and the ASD spectroradiometer measurements and should cover all possible clouds from a magnitude perspective.

The size and shape of the clouds vary from a single cloud to a large cloudbank to a nearly fully cloudy sky. Most of the analysis is performed using the single clouds and the single cloud bank.

Cloud locations vary anywhere within the hemisphere. Specific series of data acquisitions for clouds that vary in declination angle and azimuth angle are accomplished.

Finally, clouds that are very thin (low density) to very thick (high density) are used. Specifically, a 25% cloud and 75% sky spectral set of data acquisitions and 50% cloud and 50% sky set and a 75% cloud and 25% sky set are accomplished. Most of the clouds are built using 100% cloud and 0% sky.

Of all the internal water sources, Raman scattering was the only one enabled in all of the data runs. Bioluminescence and DOM and chlorophyll fluorescence are species and activity dependent and were not included. However, Raman scattering is only dependent on the excitation wavelength and can be included without requiring specific species or agitation levels (Bartlett, 1998 and Mobley, 1994).

Another constraint is the level of spatial resolution required. Most of the equations presented thus far (actually, all except for EQ 19 and EQ 20) represent continuously varying functions. To digitally perform the calculations, we need to quantize the three dimensional space. I use the same method as Mobley (1994, 1995) to enable a smooth transition to the Hydrolight code. The unit sphere (see Figure 23) defined by  $(\theta, \phi)$  heading up and down (i.e. the two hemispheres previously discussed) is quantized into 36 elevation and 72 azimuthal “quads” (roughly  $5^\circ \times 5^\circ$  sectors with the endcaps treated separately). The Hydrolight 3.0 standard is to partition the sphere into  $20 \times 24$  quads which equates to roughly  $9^\circ \times 15^\circ$  sectors. Both quad

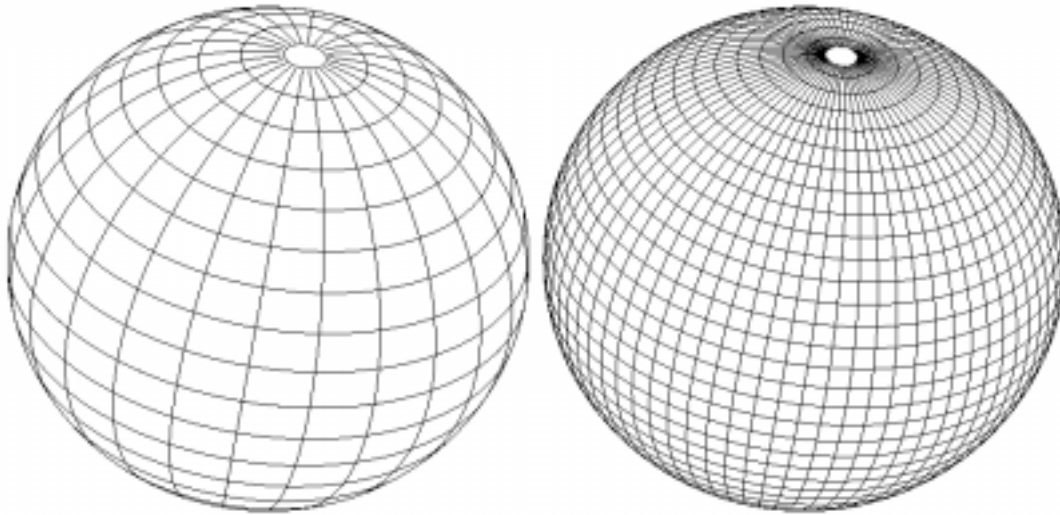


Figure 23: Two quantized spheres representing the Hydrolight 3.0 spatial resolution standardized of 20 x 24 partitions and the new higher resolution HydroMod 36 x 72 partition standard.

partitioned unit spheres are shown in Figure 23. The HydroMod standard 36 x 72 quantized unit sphere then becomes the accounting method used in the numerical solutions for the directional information. It is important to point out that the remote sensing platform will view the point in question on the water surface from one of those  $34 \times 72 + 2 = 2450$  directions. In fact, since the remote sensing platform is above the surface, we're only concerned with the upper hemisphere and one of the 1225 directions.

The final constraint is the wavelengths of interest. SeaWiFS uses 8 bands centered at 412nm, 443nm, 490nm, 510nm, 555nm, 670nm, 765nm, and 865nm with bandwidths of 20nm each except for bands 7 and 8 (765nm and 865nm) which have bandwidths of 40nm each (Barnes, 1994). These are my operating bands as well.

However, to include internal sources such as Raman Scattering, one additional band is added so that HydroMod accounts for the shorter wavelength inducing internal source radiation within the water column. The additional band is 50nm wide centered at 325nm.

These are the parameters I vary to characterize the impact of clouds to the SeaWiFS chlorophyll detection algorithms over the Laurentian Great Lakes. HydroMod is not necessarily limited to the scope provided here.





## *Chapter 5*

### **RESULTS AND ANALYSIS**

Approximately 350 HydroMod data acquisition runs were accomplished for this effort. I will not present them all here. Instead, I will walk through one set of calculations and then show the final results for several runs at once.

#### **Single Step-by-Step Analysis**

To begin, consider the two input sky radiance files in Figure 24. The data sets are displayed in decibel log format for viewing purposes. (The units on the scales are given as “dBr” for “decibels relative to a single radiance unit where, here, the radiance units are  $\mu\text{W}/\text{cm}^2 \cdot \text{sr} \cdot \text{nm}$ . For instance, the 24.9328dBr as the maximum value on the scale given in Figure 24(a) and(b) represents  $10^{2.49328} = 311.37 \mu\text{W}/\text{cm}^2 \cdot \text{sr} \cdot \text{nm}$  and the 43.1135dBr in Figure 25 represents  $10^{4.31135} = 20480.95 \mu\text{W}/\text{cm}^2 \cdot \text{sr} \cdot \text{nm}$ . The “relative to 1 radiance unit” is required because, mathematically, a logarithm’s argument must be unitless.) The geometry is the same as given previously with the center of the circle representing zenith and the edges representing the horizon with  $0^\circ$  and North at the top. Two sky inputs are shown with Figure 24(a) representing a clear sky and Figure 24 (b) representing the same sky with a single cloud at  $41^\circ$  declination angle and  $100^\circ$  azimuthal angle. The direct sun term is removed from these data so that the radiance distribution across the sky can be viewed. If we add

the direct sun radiance term to the input, data similar to that displayed in Figure 25 results and the sky distribution is not as easy to view.

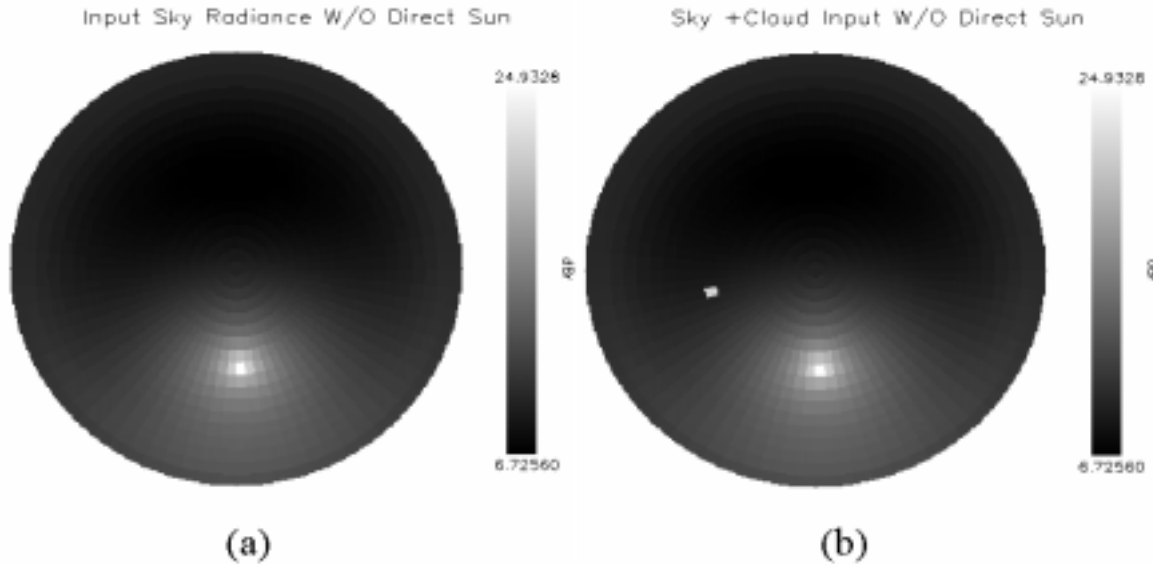


Figure 24: Two input sky radiance data sets. (a) represents a clear sky with no clouds and (b) is the same sky with one single cloud at 40° declination angle and 100° azimuth angle. The data are displayed in log format (decibels relative to a radiance unit of  $\mu\text{W}/\text{cm}^2 \cdot \text{sr} \cdot \text{nm}$ ) with the scales for each of the displays given to the right of the display. The circular region represents a hemisphere; the center is nadir (or zenith as the case may be) and the outside edges are the horizon. North is at the top. For these images, the sun is located due South at a declination angle of 41°. The data are for  $\lambda=555\text{nm}$ .

All of the data displayed in Figure 24 through Figure 32 were generated using HydroMod and nominal Lake Ontario waters of 10 $\mu\text{g}/\text{l}$  of chlorophyll, 2 $\text{g}/\text{m}^3$  dissolved organic carbon, and 6 $\text{g}/\text{m}^3$  of suspended minerals. The MODTRAN generated atmosphere is for a maritime 23Km visibility, mid-latitude summer with the sun due south in the quad centered at 41.143°. Two HydroMod sky files were used: a specially generated “direct sun term only” sky and a sky only file with no direct sun term. This

allows separating out the sky and sun as in Figure 24 and Figure 25. The output files were combined using superposition. Raman scattering was enabled starting at 300nm. Most of the data are for SeaWiFS Band 5 (centered at 555nm) with Bands 3 (centered at 490nm), 7 (centered at 765nm) and 8 (centered at 865nm) also used as noted in the individual figures.

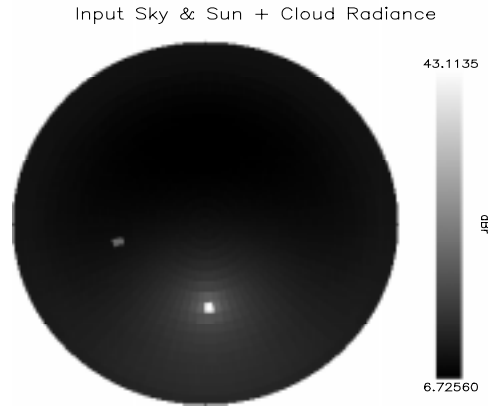


Figure 25: The direct sun radiance term has been added to Figure 24(b). Even when displayed on a decibel scale, the radiance distribution across the sky is not viewable.

Adding a 5m/sec (9.7knots) wind to roughen the surface yields the radiance reflected at the water surface,  $L_{\text{ref}}(\theta, \phi)$ , is displayed in Figure 26 (a) and (b). The total water leaving radiance,  $+L_{\lambda=555\text{nm}}^{\uparrow}(0; \theta, \phi)$ , (which includes the reflected radiance) is displayed in Figure 26 (c) and (d). The two sky input files from Figure 24 with the direct sun term included as in Figure 25 were used to generate these data. The upwelled radiance distribution for each of these cases is displayed in

Figure 27 . The only difference in the two displays is, again, the single cloud at 41° declination and 100° azimuth. Note that upwelled radiances for declination angles

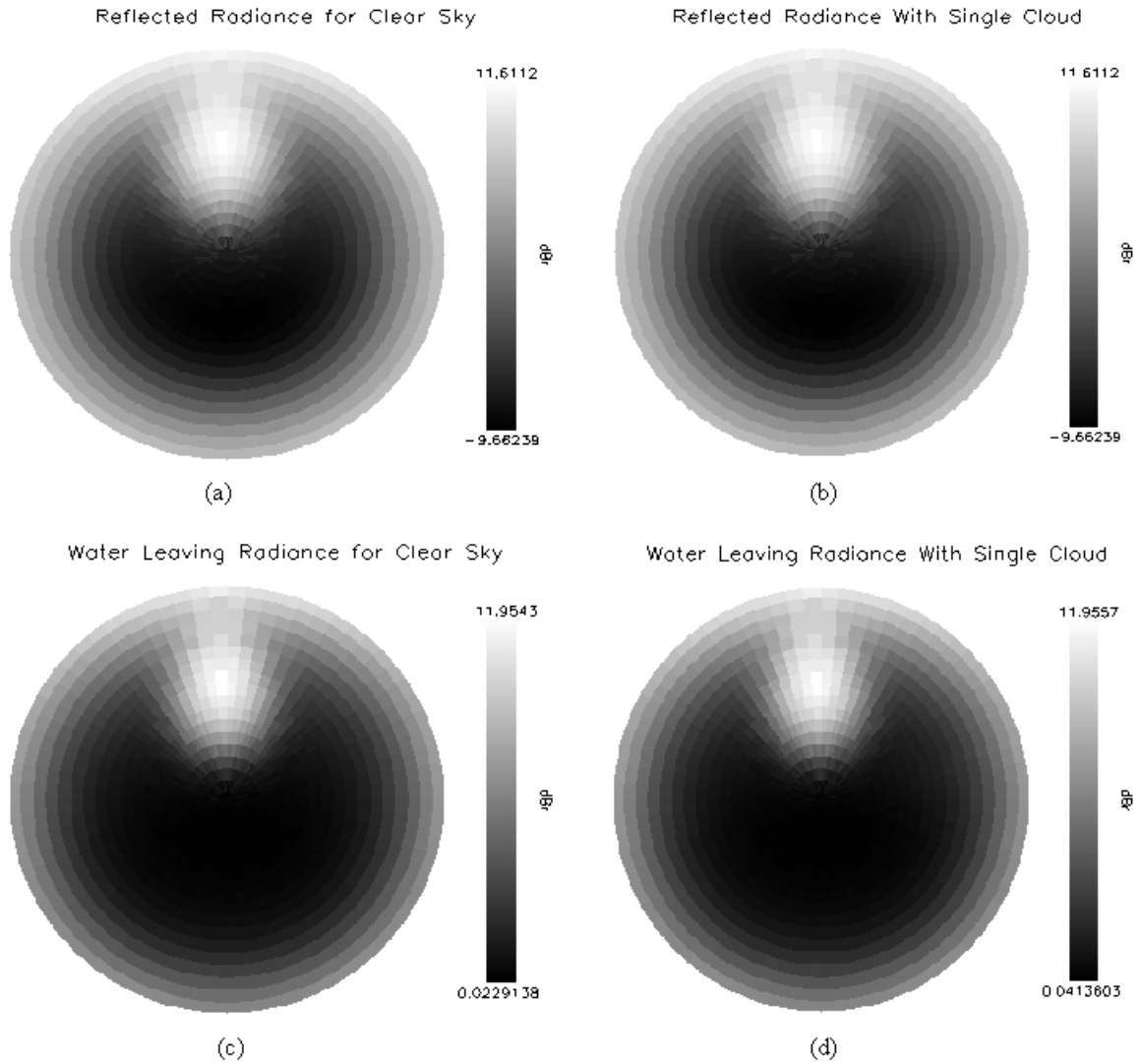


Figure 26: Surface Reflected (a and b) and total water leaving (c and d) radiance for the two input files given in Figure 24. (a) and (c) are for the clear sky only and (b) and (d) are for the single cloud in that clear sky. All four plots are for  $\lambda=555\text{nm}$  and are displayed in decibels relative to  $1 \mu\text{W}/\text{cm}^2 \cdot \text{sr} \cdot \text{nm}$ . Note very little noticeable difference in the two cases. (The atmospheric and water parameters used for these data are described at the beginning of the section.)

greater than  $75^\circ$  do not reach the SeaWiFS sensor and are not calculated or used.

The black “no data” ring remains in the displays to highlight the pre-horizon cutoff.

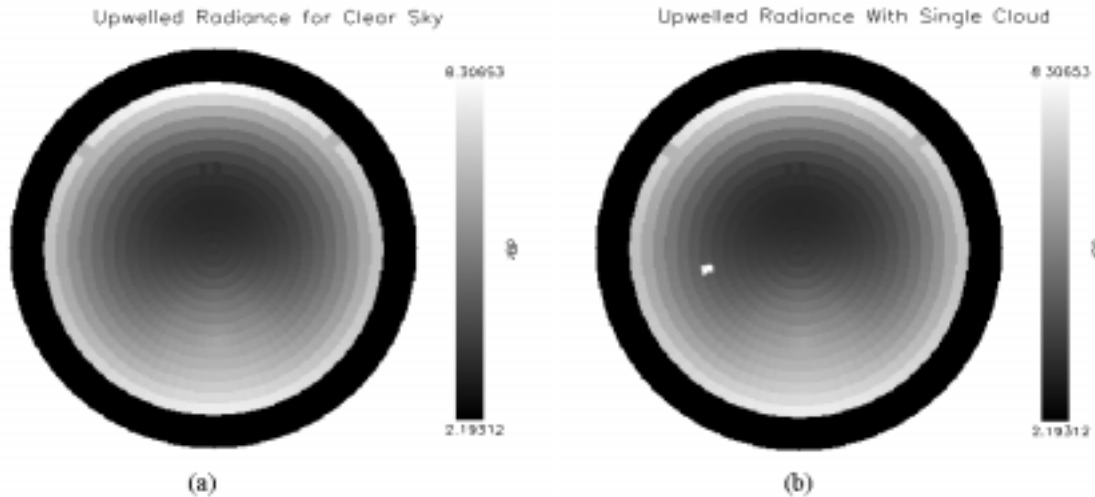


Figure 27: Two nearly identical upwelled radiance data sets. The only difference between (a) and (b) is the single quad that contains a cloud. The upwelled radiance data do not extend to the horizon because of the limited look angles for orbiting sensors. The SeaWiFS maximum pixel centered declination angle for upwelled radiance is  $74.95^\circ$ . Therefore, upwelled radiance is neither calculated nor used beyond that point. However, the black “no data” ring remains in the data displays to prevent angular confusion. (The atmospheric and water parameters used for these data are described at the beginning of the section.)

We can combine all of these data (Figure 24 through Figure 27) along with the transmission coefficient for the water leaving component propagating through the atmosphere to get the total radiance at the sensor. Figure 28 and Figure 29 show the total radiance at the sensor for the four SeaWiFS bands of interest: 490nm, 555nm, 765nm, and 865nm for these two cases. Together with the total water leaving radiance, these are the bands and the data sets that I’ll use throughout the rest of the analysis.

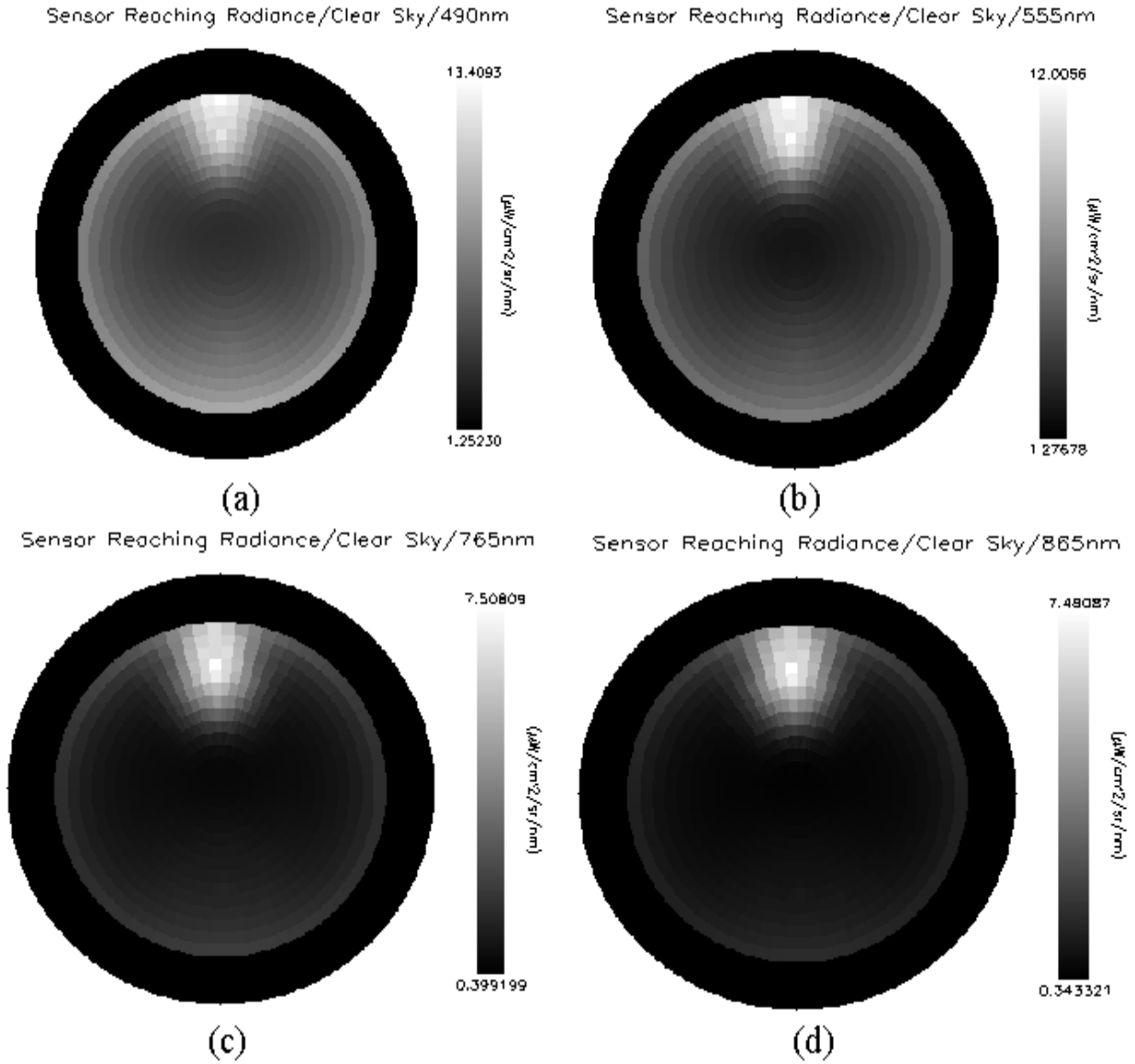


Figure 28: Total Sensor reaching radiance for the clear sky case at SeaWiFS bands 3 (a,  $\lambda=490\text{nm}$ ); 5 (b,  $\lambda=555\text{nm}$ ); 7(c,  $\lambda=765\text{nm}$ ) and 8 (d,  $\lambda=865\text{nm}$ ). The sun glint is very apparent. Also note less radiance reaching the sensor in the near IR. The blank “no data” zone from the upwelled radiance is also enabled here. (The atmospheric and water parameters used for these data are described at the beginning of the section.)

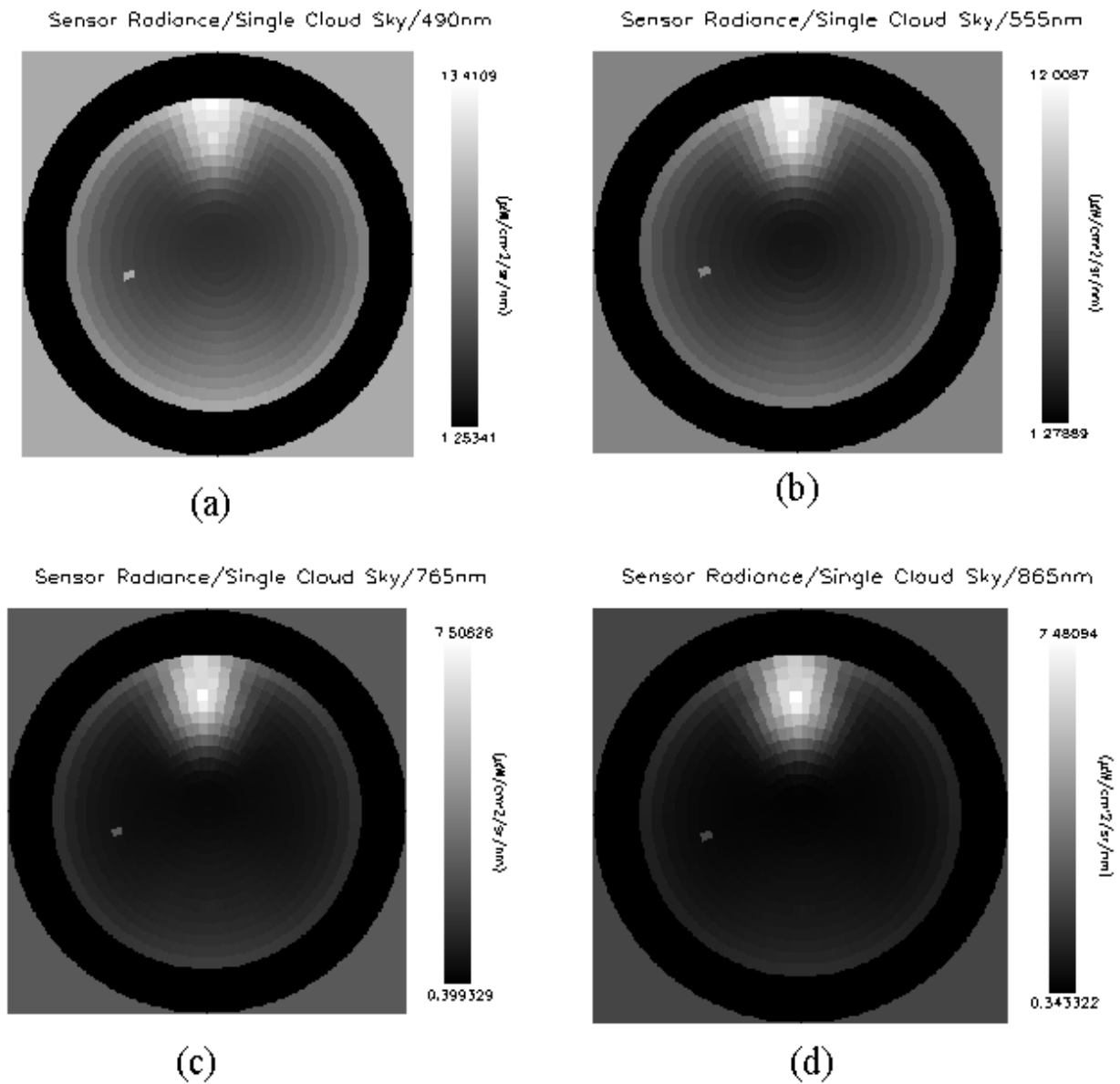


Figure 29: Total sensor reaching radiance for the single cloud case at SeaWiFS bands 3 (a,  $\lambda=490\text{nm}$ ); 5 (b,  $\lambda=555\text{nm}$ ); 7(c,  $\lambda=765\text{nm}$ ) and 8 (d,  $\lambda=865\text{nm}$ ). The sun glint is very apparent. Also note less radiance reaching the sensor in the near IR. (The atmospheric and water parameters used for these data are described at the beginning of the section.)

Looking close at Figure 26 (a) and (b) the cloud induced reflection component may be just barely noticeable. However, by the time the total water leaving radiance is calculated as in Figure 26 (c) and (d), any visual differences that may have been discernable with only the reflected component are gone. Obviously, propagating the water leaving radiance to the sensor and adding the upwelled radiance further obliterates any visual differences caused by the cloud (outside of the single quad that contains the cloud).

We can, however, calculate the differences in the total radiance at the sensor and determine a percentage error using

$$\%error = \frac{L_1 - L_2}{L_2} \bullet 100\%$$

EQ 37

where the  $L_1$  and  $L_2$  represent the single cloud and clear sky cases for each wavelength, and  $(\theta, \phi)$  direction at any location (although the two primary locations are at the sensor and at the water surface). Calculating the error at the sensor for the four bands of interest in the SeaWiFS chlorophyll determination algorithms yields the data displayed in Figure 30.

From these data, it appears as though most of the error comes from the reflected component of the water leaving radiance and that the peak error tapers to zero following a near Gaussian pattern. This conclusion is reinforced by viewing the



data in other manners such as that found in the three dimensional view of Figure 31 or the radial slice through the center and peak as in Figure 32. Both of these data sets are for the error in Band 8 as displayed in Figure 30(d).

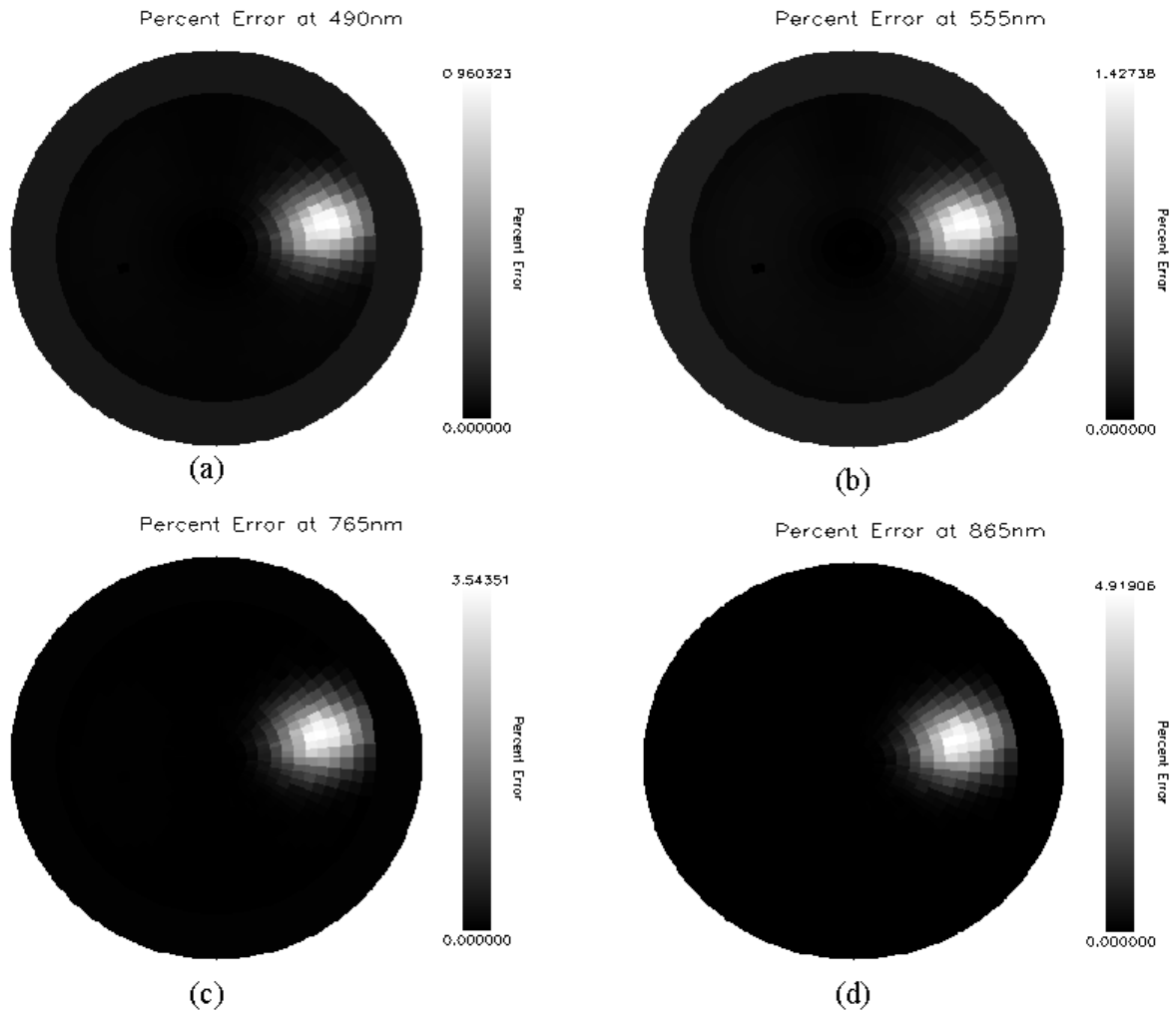


Figure 30: Error caused by a single cloud in an otherwise clear sky. The peak error ranges from less than 1% in (a) for Band 3 (490nm) to almost 5% in (d) for Band 8 (865nm). The other two percent errors displayed are for SeaWiFS Band 5

(b) and Band 7 (c). (The atmospheric and water parameters used for these data are described at the beginning of the section.)

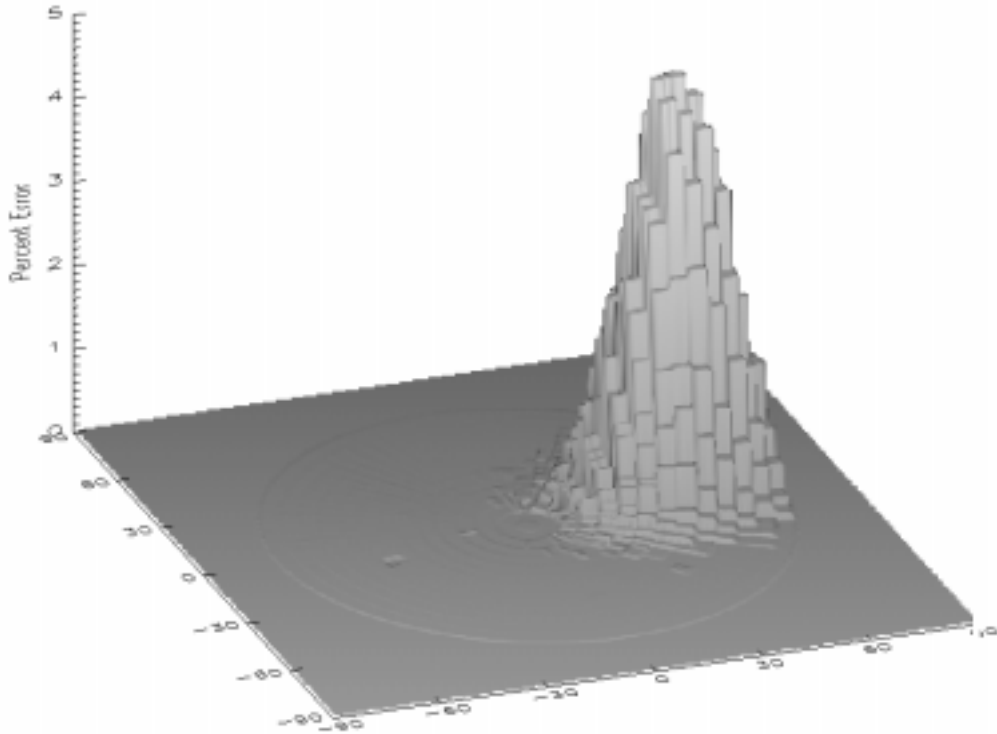


Figure 31: A 3-D view of Figure 30 (d) with the “x” and “y” axis of this plot labeled for theta angles from 0° at the center to 90° at the edges. The + and – signs on the theta angles serve to reference the quadrants of the normally circular plots. The Gaussian like shape of the data is even more apparent here than in Figure 30.

The display in Figure 32 in particular seems to call for two specifications to quantify the percent error: the peak and the full width at half the maximum (FWHM or half-width). The concept of a half-width as applied to the 3-D data, of course, would be better. Once we realize that these “widths” represent solid angles and that the widths can change by changing the input cloud solid angle (i.e. a bigger or smaller clouds), the concept of the half-width applied here requires modification. The

modification that I will employ is to use the ratio of the total solid angle with a percent error greater than half the peak percent error ( $\Omega_{FWHM}$ ) to the solid angle of the cloud that caused the error ( $\Omega_{Cloud}$ ) and call it an “normalized error width ratio” or  $\epsilon_{WR}$ .

$$\epsilon_{WR} = \frac{\Omega_{FWHM}}{\Omega_{Cloud}}$$

EQ 38

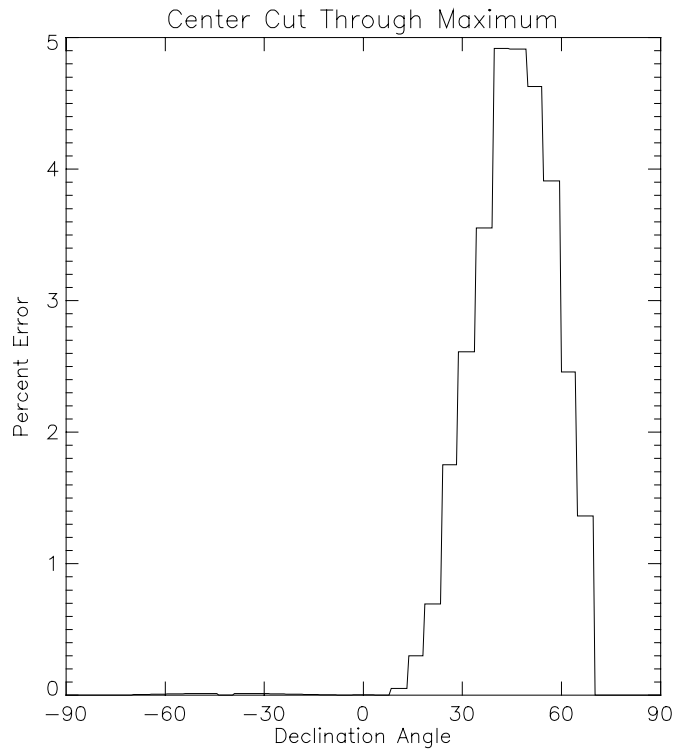


Figure 32: A diameter slice through the center of Figure 30 (d) yields the data plotted here. Both the 5° binning and the Gaussian like shape are apparent. The peak error occurs at a declination angle centered at 41.143° which is the center of the quad opposite the actual cloud. The location is consistent with the reflection angle off of the water surface.

For the Band 8 data shown in Figure 30(d), Figure 31, and Figure 32, the cloud was centered on the quad at 100° azimuth and 41.143° declination angle. It had a solid angle of 0.0051538sr [ $\sin(\theta)d\theta d\phi = \sin(41.143^\circ) \cdot (5.143^\circ)(5^\circ)(\pi/180^\circ)^2 = 0.0051538\text{sr}$ ] and the FWHM solid angle of the percent error is 0.174674sr (found by summing the quads with percent error greater than  $\epsilon_{\text{peak}}/2$ ) which yields a normalized error width ratio of  $\epsilon_{\text{WR}} = 33.892$ . The peak error,  $\epsilon_{\text{peak}}$ , is 4.912% in that band.

### **Affect on the SeaWiFS Calculations**

Now that we have our quality parameters, we can take the next step by employing some of the SeaWiFS algorithms. We first use EQ 27 to convert the radiances to reflectances and then EQ 29 to remove the Rayleigh component (if the wind speed is below 9m/sec, we don't need to worry about the whitecap component according to Gordon, 1997). With the reflectance values, we can determine the ratio for  $\rho(765\text{nm})$  and  $\rho(865\text{nm})$  and the error in that ratio due to the presence of the clouds. For this example, the peak error in the ratio between  $\rho(765\text{nm})$  and  $\rho(865\text{nm})$  is approximately 1.24% (negatively) with a normalized error width ratio of 31.6.

That error will cause an error in the atmospheric subtraction. Unfortunately, all that we can predict is that the error will most likely underestimate the chlorophyll levels. The fact that the peak error is negative means that the Band7 to Band 8 ratio is less when the cloud is present than it is when the cloud is not present (i.e. the white cloud introduces a flatter spectrum). If that is true, the lower ratio will, in turn, yield a flatter  $\epsilon$  using EQ 30. The flatter  $\epsilon$  will result in values of  $\rho_a(490\text{nm}) + \rho_{ra}(490\text{nm})$  and

$\rho_a(555\text{nm}) + \rho_{ra}(555\text{nm})$  that are too low with a larger error at 490nm than at 555nm. Taking this to the next step,  $\rho_w(490\text{nm})$  and  $\rho_w(555\text{nm})$  will be too large with, again, more error in  $\rho_w(490\text{nm})$  than  $\rho_w(555\text{nm})$ . Thus, the ratio for  $\rho_w(490\text{nm})/\rho_w(555\text{nm})$  will be too large and the chlorophyll content calculated using EQ 33 will be less than the true value. Without the actual data used to derive the atmospheric subtraction routines, we cannot determine exactly how much of an underestimate is calculated. That step is left for further study.

We can, however, analyze the effect of the water leaving reflectance ratio for bands 3 and 5. We do this by assuming that the exact atmosphere can be subtracted and then using the  $\rho_w(490\text{nm})$  and  $\rho_w(555\text{nm})$  as calculated by HydroMod for the analysis. Doing so yields a peak error in  $\rho_w(490\text{nm})/\rho_w(555\text{nm})$  of 3.49% and a normalized error width ratio of 30.82. Both of these error plots can be found in Figure 33.

The error in the derived chlorophyll content strictly due to the error in  $\rho_w(490\text{nm})/\rho_w(555\text{nm})$  of 3.49% is directly calculable. The scenario used chlorophyll content of 10 $\mu\text{g/l}$  along with some suspended minerals and dissolved organic matter. The original SeaWiFS algorithm, EQ 31, calculates the chlorophyll content of the baseline (cloudless) scene to be around 11 $\mu\text{g/l}$  and the new algorithm, EQ 33, computes the chlorophyll content to be around 5.8 $\mu\text{g/l}$ . The difference in the predicted chlorophyll content in the direction of the peak error is 1.44 $\mu\text{g/l}$  between the cloud and

no cloud case for the old algorithm and only 0.47 for the new algorithm. Both of these values predicted lower chlorophyll with the cloud than without a cloud.

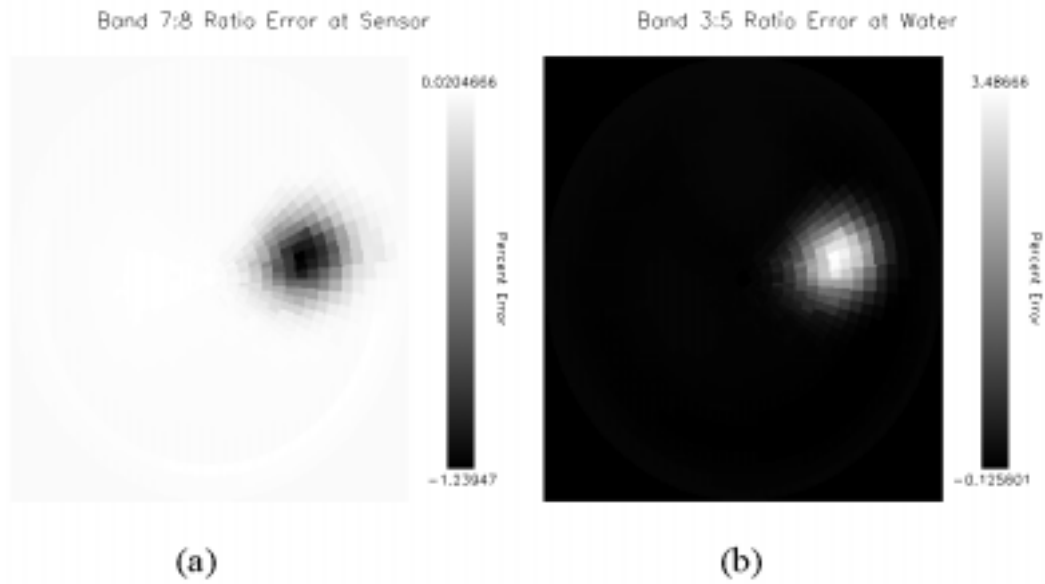


Figure 33: The error in the ratio between  $\rho_t(765)$  and  $\rho_t(865)$  (a) and between  $\rho_w(490)$  and  $\rho_w(555)$  (b) is illustrated. Note that the error in (a) has a negative “peak” due to a flatter spectrum caused by the cloud while the error in (b) has a positive peak. The ultimate impact on the derived chlorophyll content is unknown for (a) other than the tendency to underestimate the chlorophyll. For (b), the impact on the chlorophyll content is calculatable and in this case will also under-estimate the chlorophyll content.

The two most important parameters for the cloud impact are the error in the ratio for  $\rho_t(765\text{nm})$  to  $\rho_t(865\text{nm})$  and error in the ratio of  $\rho_w(490\text{nm})$  to  $\rho_w(555\text{nm})$ .

Using the same scenario and changing the brightness of the single cloud yields a series of peak errors and normalized error width ratios. The peaks are plotted in

Figure 34. The normalized error width ratios were all nearly identical around a value of 31.

As expected, as the brightness of the cloud increases, the percent error also increases. The white cloud causes the ratios of both the top of the atmosphere bands 7 and 8 and the water leaving bands 3 and 5 to move closer to 1:1 (white). However, in the Figure 34(a), the original Band 7/8 ratio was greater than 1:1 and the white cloud decreased the ratio. In Figure 34(b), the original Band 3/5 ratio was less than 1:1 and the white cloud increased the ratio.

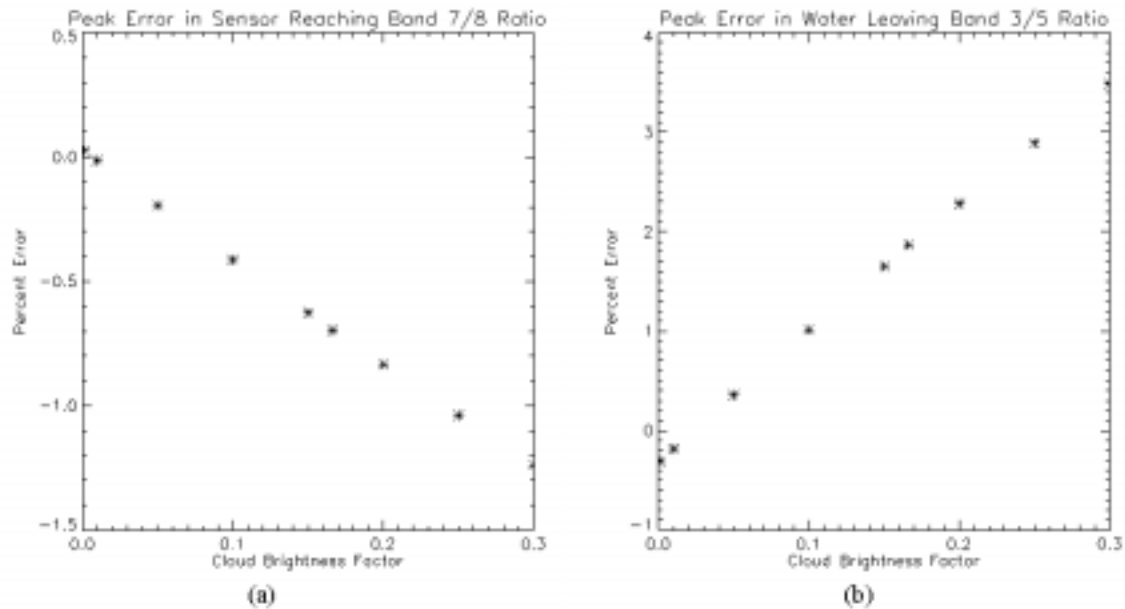


Figure 34: Change in peak percent error for varying cloud brightness levels. (a) is for the peak error in the ratio between the band 7 reflectance and the band 8 reflectance at the top of the atmosphere. In (b), the water leaving reflectance components for bands 3 and 5 were used. These are the important ratios for determination of the chlorophyll content using the SeaWiFS algorithms.

## Cloud Location Affects

Moving the single cloud with a fixed brightness level will allow the normalized error width ratio to vary. Specifically, using a bright cloud with a brightness factor of 0.30 and moving it radially from the end cap to the horizon yields the data in Figure 35.

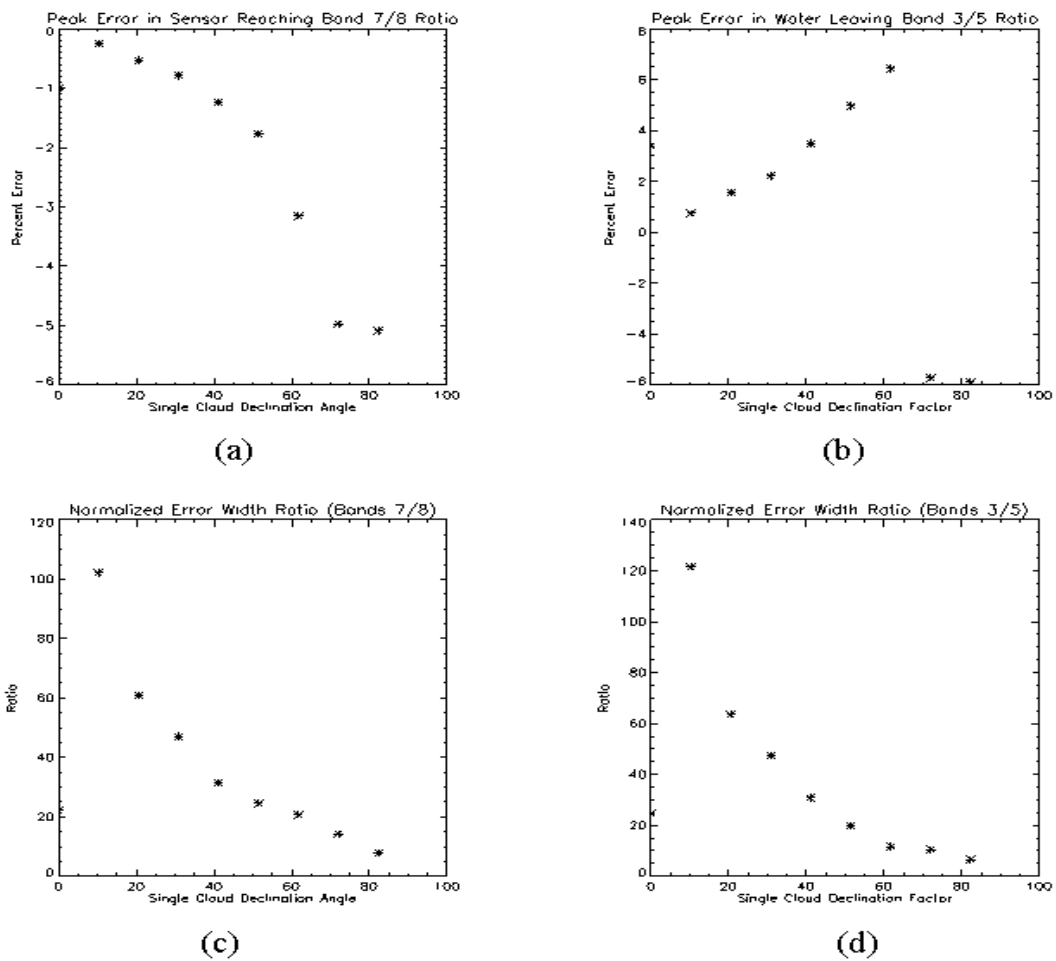


Figure 35: Effect of changing the cloud declination angle (and therefore the solid angle size of the cloud) is shown. The peak error curves of (a) for the sensor reaching Band 7 to Band 8 ratio and (b) for the water leaving Band 3 to Band 5 ratio cutoff above 70° due to the inability of remote sensors to view at higher angles. (That is, since the sensors cannot view at those angles, the HydroMod calculations do not consider them and any data outside of the 70° mark is erroneous.) Also note that the endcap cloud is fairly large, but most of the light from that cloud will enter the water and not reflect.



The Fresnel reflection coefficient increases with increasing incidence angle as in Figure 22. The increase in surface reflectance yields an increase in the error rate as the cloud's declination angle increases. The normalized error width ratio, however, decreases with increasing declination angle because the solid angle of the quad containing the cloud increases.

Note that the drastic changes in error rates beyond the  $70^\circ$  point are geometry artifacts only. Since remote-sensing systems cannot view a point on the water surface at such high declination angles, HydroMod does not account for upwelled radiance in that zone. The result is that any analysis outside of the  $70^\circ$  declination angle barrier is meaningless as is the drastic change artifacts illustrated in Figure 35.

Several other series of runs were accomplished moving the single cloud to various locations around the hemisphere with very predictable results using the data already presented. As the cloud moved, the peak error maintained a position  $180^\circ$  in azimuth away from the cloud at the same declination angle. The normalized error width ratios were comparable to those given in Figure 35 at the corresponding declination angle locations for the cloud. Other than that short summary, those data will not be presented here.

### **Introducing a Cloudbank**

The next phase of the analysis is to increase the physical size of the cloud. The input cloud sky illustrated in Figure 36 was used for a series of runs similar to the

single cloud case discussed. The single cloudbank of Figure 36 is also a slightly more realistic scenario.

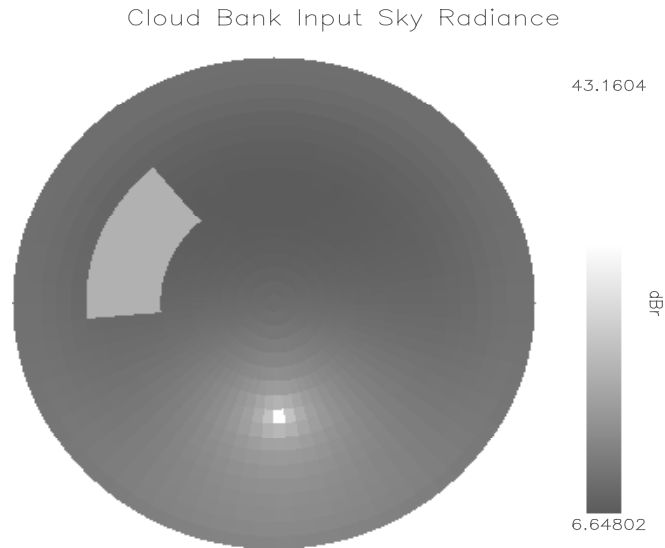


Figure 36: Cloud Bank Input Sky Data. A single cloud bank centered roughly at  $45^\circ$  declination angle between  $45^\circ$  and  $90^\circ$  in azimuth was used for input. The size of the cloud did not change for a series of data acquisitions that varied the brightness level and the cloud/(cloud+sky) ratio. The cloud shown above has a brightness scale factor of 0.075 and the displayed data are for  $\lambda=555\text{nm}$ .

A similar series of data acquisition runs were accomplished with the cloudbank as was with the single cloud. The solid angle of the cloudbank was approximately  $0.334\text{sr}$ . The normalized error width ratio stayed between 1.0 and 3.0 for cloud brightness factors between 0.3 and 0.0 (a cloud brightness factor of 0.0 equates to no radiance from the direction of the cloud reaching the water surface; i.e. a very black cloud). The error peaks for the two main parameters are shown in Figure 37.

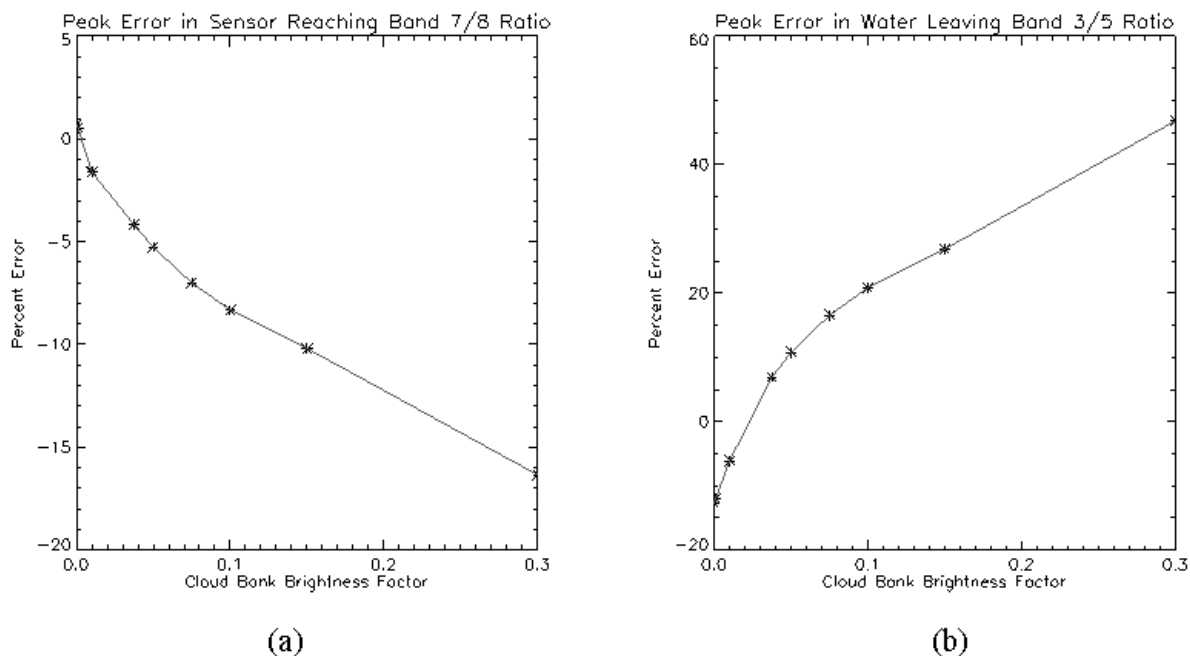


Figure 37: Percent Error for the Two Main Quality Parameters. The peak errors for the sensor reaching Band 7/8 ratio and the water leaving Band 3/5 ratio (b) are plotted as a function of the cloud bank brightness factor. These errors can be quite large for spatially large cloudbanks. The normalized error width ratio for all of these errors ranged from 1.0 to 3.0. The solid angle of the cloud causing the errors was approximately 0.334 sr.

The error in the water leaving radiance of the Band 3/5 ratio is quite high. Even for moderate clouds, the errors can be over 10%. The affect of these errors on the chlorophyll levels on an error percentage basis is even more extreme as illustrated in Figure 38. The data plotted there show that the percent error in the chlorophyll calculations can be over 50% for even moderately bright clouds. With darker clouds, the amount of chlorophyll will be overestimated as illustrated by a negative error rate.

The calculated chlorophyll levels for this case are plotted in Figure 39. Here we see that the original SeaWiFS algorithm would have reported a fairly accurate

10.14 $\mu\text{g/l}$  if no clouds were present, but the new algorithm computes only 5.55 $\mu\text{g/l}$  for the baseline level. The suspended minerals and dissolved organic material cause underestimated chlorophyll levels even without clouds (assuming perfect atmospheric

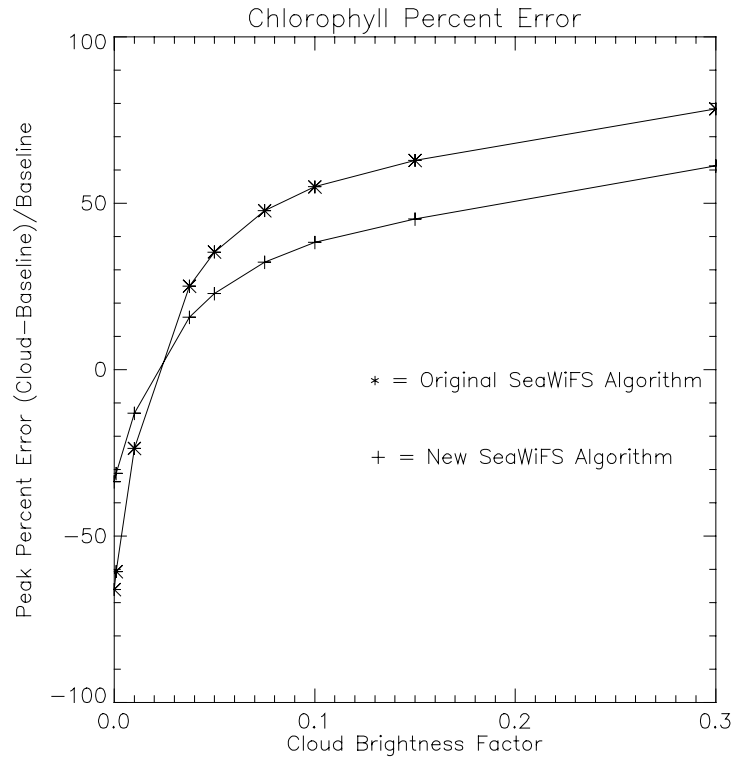


Figure 38: Peak Percent Error on the Chlorophyll content calculated using the original SeaWiFS algorithm (\*) and the new SeaWiFS algorithm (+). Errors as high as 50% for moderate clouds are predicted. The peak error occurs in the azimuth direction 180° away from the cloud at the same declination angle.

subtraction). The affect of the clouds will tend to further lower the estimate. The final analysis plot for these data is the difference in the chlorophyll level calculated with the cloud present less the chlorophyll level calculated without the cloud present. The difference data are plotted in Figure 40.

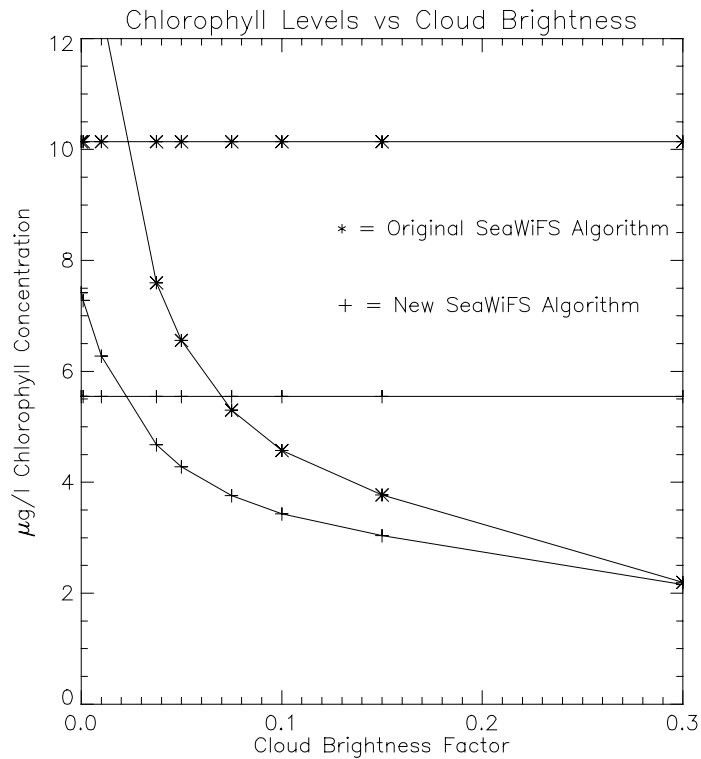


Figure 39: Calculated chlorophyll levels using the original SeaWiFS algorithm (\*) and the new SeaWiFS algorithm (+). The original algorithm would have been fairly close to the actual chlorophyll level of 10µg/l, but the new algorithm underestimates the level. The effects of the clouds tends to reduce the estimate even further.

With Figure 40 it is easy to see that the chlorophyll levels predicted with clouds in the vicinity can be higher or lower than the level predicted without the clouds. For darker clouds and a true chlorophyll level of 10 µg/l, the cloud will induce an overestimate. Brighter clouds at the same true chlorophyll level will induce an underestimate.

The values calculated in Figure 38 and Figure 40 represent error of cloud versus no clouds and NOT cloud case versus true levels. The errors plotted and analyzed here represent the cloud impact only; referencing the cloud impact to the true levels would confuse the impact due to the SM and DOM with the cloud results.

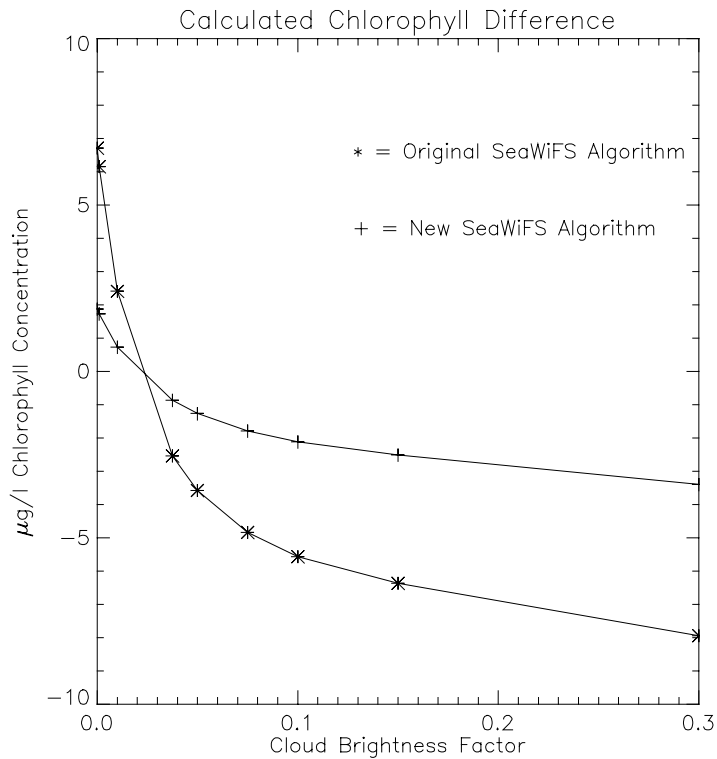


Figure 40: Calculated chlorophyll differences between the cloud case and the no cloud case using the original (\*) and the new (+) SeaWiFS algorithms

The next step is to look at cloud density levels. While doing that, I want to show the affect of continually darkening clouds. Instead of plotting cloud brightness factors ranging from 0.3 to 0.0, we'll reduce the range to 0.15 to 0.0 to see some of the effects at very dark cloud brightness levels.

### Cloud Density Level Impact

With this series of data acquisition runs, the cloud density changed from quads with 100% clouds to quads with 50% cloud and 50% sky to quads with 25% clouds and 75% sky. The cloud brightness factors were left intact, but the predominance of data

presented here are for the lower brightness factors to show the aforementioned affects at darker cloud regions.

Refer to Figure 41 which shows the three cloud/(cloud+sky) density levels plotted as the error in the Band 7/8 ratio at the sensor versus the cloud brightness factor. We see from these data that the denser clouds always have more error than the less dense clouds.

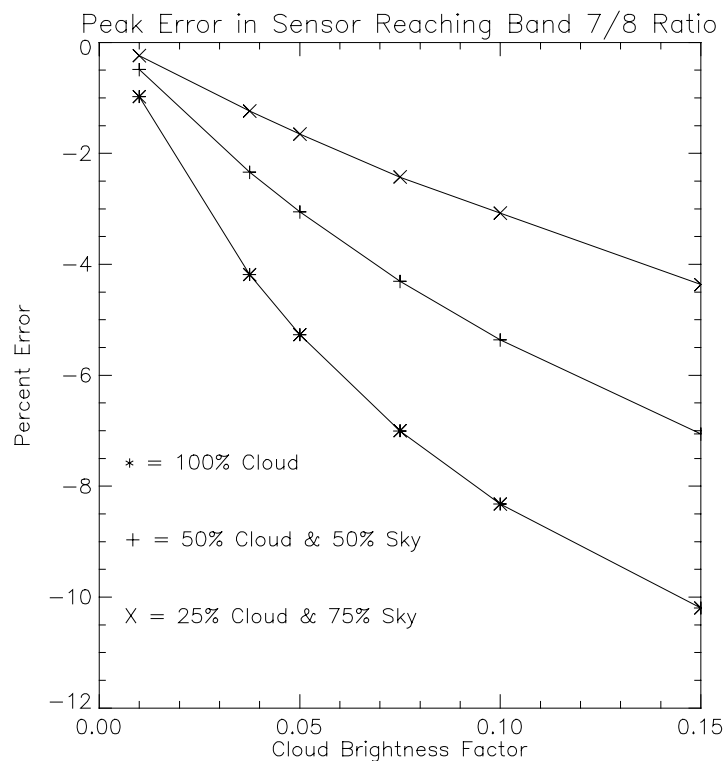


Figure 41: Peak Error in the sensor reaching reflectance Band 7/8 ratio values for varying cloud brightness levels and different cloud densities. There is more error in the Band 7/8 ratio at all brightness factors for denser clouds than for thinner clouds. The three scenarios plotted here are for a cloud representing 100% of each of the quads, 50% of each of the quads, and 25% of each of the quads in the cloud sector displayed in Figure 36

The same type of phenomenon occurs with the water leaving Band 3/5 ratio error as shown in Figure 42. Here we see that the error caused by the cloud cross the zero point somewhere between a brightness factor of 0.05 and 0.01. For clouds brighter than a factor of 0.05, the denser clouds clearly have a larger positive percent error in the Band 3/5 water leaving reflectance ratio. This results in an underestimate of the chlorophyll content using both of the SeaWiFS algorithms (see Figure 43 and Figure 44).

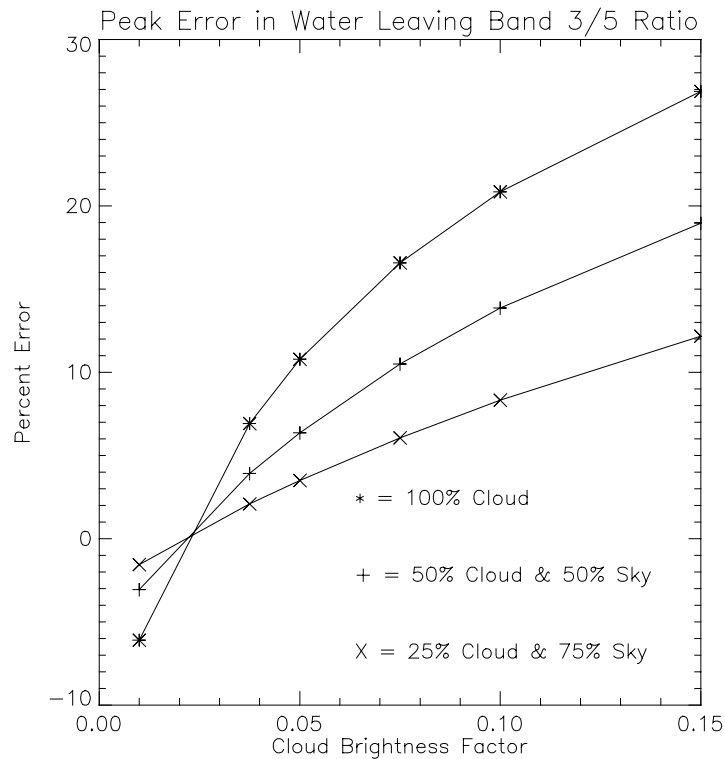


Figure 42: Peak Error in the water leaving Band 3/5 Ratio for varying cloud brightness levels for different cloud densities. The cross over between brightness factors of 0.05 and 0.01 occurs at the point where the cloud reflected component is on the same order of magnitude as the water leaving component. In is also where the calculated chlorophyll levels are inflated using either the original SeaWiFS algorithm (see Figure 43) or the new SeaWiFS algorithm (see Figure 44).



However, somewhere between a cloud brightness factor of 0.05 and 0.01, the calculated chlorophyll content using either the original SeaWiFS algorithm (see Figure 43) or the new SeaWiFS algorithm (see Figure 44) is actually overestimated given the cloud bank and water parameters in the scenario.

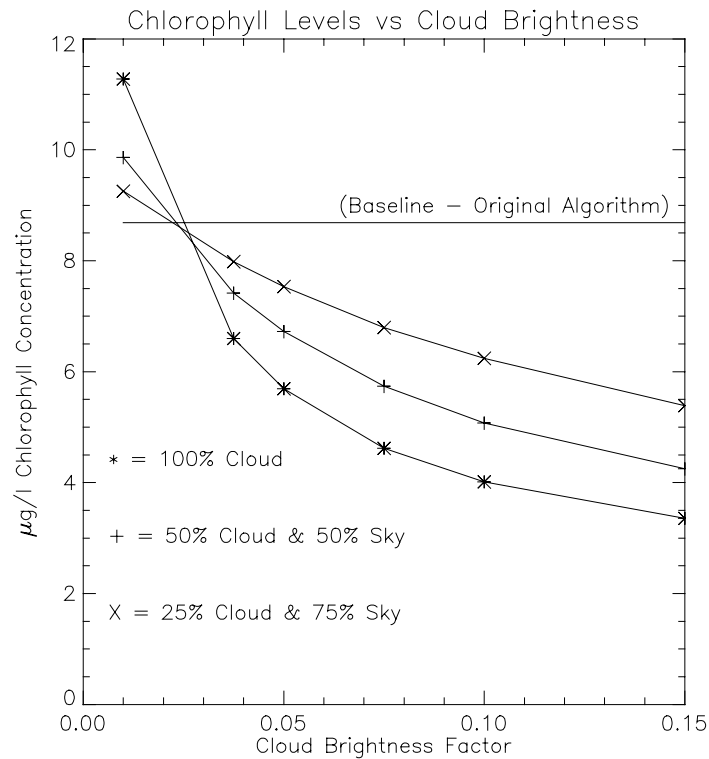


Figure 43: Changes in the Chlorophyll level for the varying cloud brightness for different cloud densities. These calculations were made using the original SeaWiFS algorithm. In most cases, the cloud density level that is higher results in a larger underestimate of the chlorophyll content, but in some limited cases, the chlorophyll content is overestimated.

## The Wind Speed Impact

With that anomaly exposed, we can turn to the impact of varying wind speeds on the important parameters and derived chlorophyll content. The following data represent several data acquisition runs at varying wind speeds and cloudbank

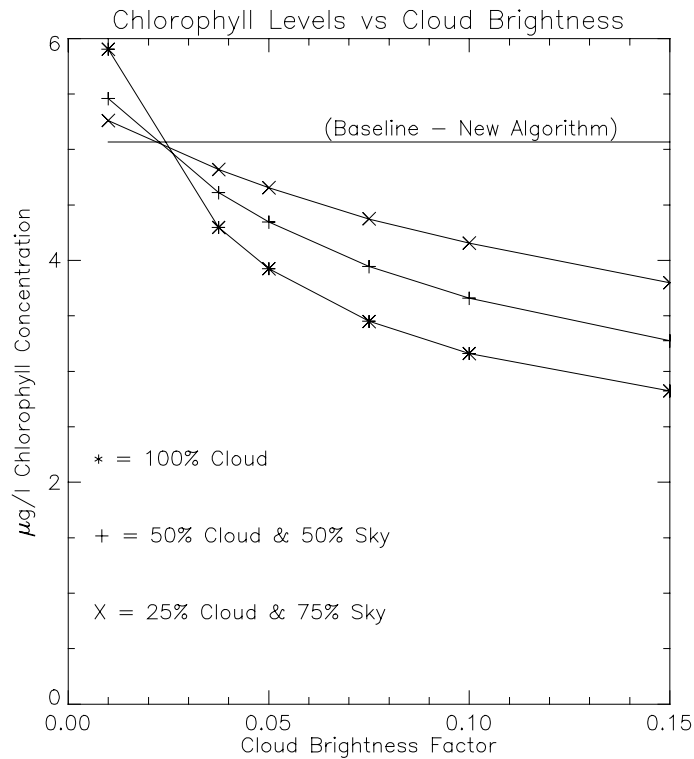


Figure 44: Changes in the Chlorophyll level for the varying cloud brightness for different cloud densities. These calculations were made using the new SeaWiFS algorithm. In most cases, the cloud density level that is higher results in a larger underestimate of the chlorophyll content, but in some limited cases, the chlorophyll content is overestimated.

brightness factors. The cloudbank used in this set of runs was slightly different than in previous data runs. The cloudbank was smaller (spatially) and closer to the endcap quad. Four (and sometimes five) cloud brightness levels were used at wind speeds varying from 0.0m/sec to 10.0 m/sec in 1.0m/sec steps.

Referring to Figure 45, we see little variation in the peak error of the sensor reaching Band 7/8 ratio for wind speeds above 3m/sec or so; certainly, the cloud brightness level seems to have more impact.

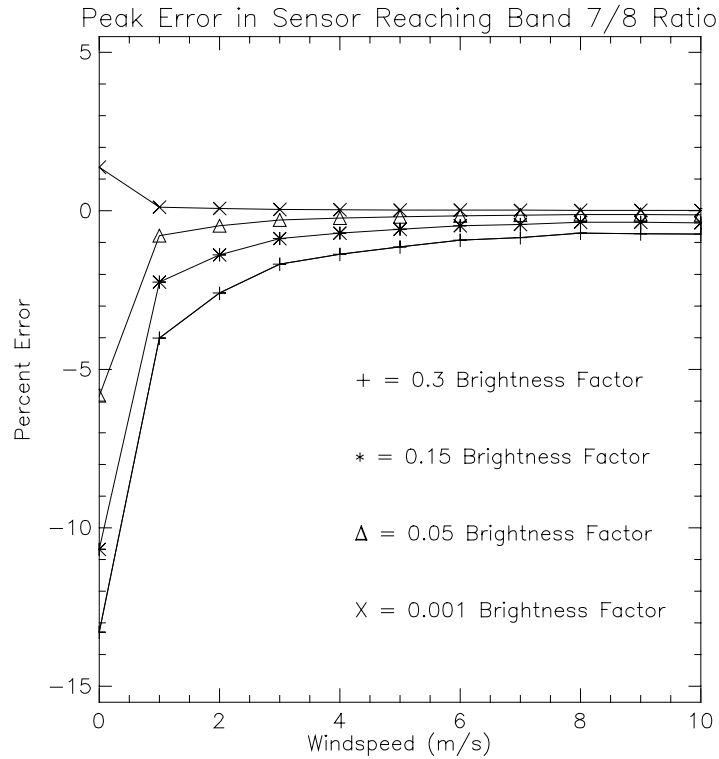


Figure 45: Percent error in Band 7/8 ratio with respect to wind speed for different brightness factor levels.

However, below 3m/sec, the variation in the peak error due to wind speed accelerates to extreme values. Further, we can see in both Figure 45 and Figure 46 that dark cloud affects and bright cloud affects diverge. In Figure 46 the impact of wind speed on the water leaving Band 3/5 ratio is plotted for cloud brightness factor levels ranging from 0.3 to 0.001. Here again, the variation with wind speed is minimal above 3m/sec or so and the variation accelerates for lower wind speeds. One saving grace for the very large errors below 1m/sec is that they correspond to very low normalized error width ratios (close to 1.0).

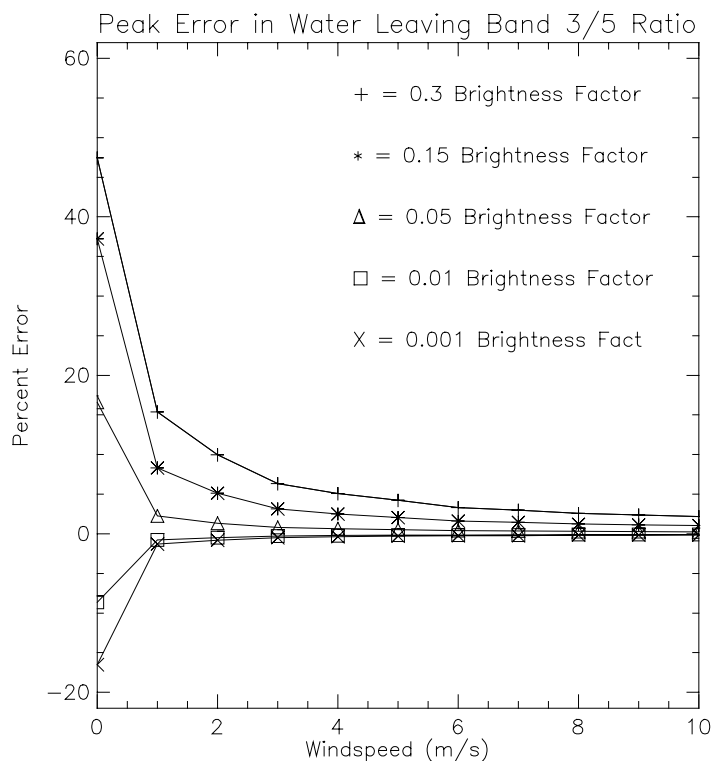


Figure 46: Percent Error in the Band 3/5 ratio as a function of wind speed at different cloud brightness factor levels

That is very intuitive. At very low wind speeds, there are very little surface waves and most of the cloud radiance reflects specularly into one quad (or at least a very limited set of quads). Since all of that radiance will reflect into one direction (tempered by Fresnel's reflection coefficient) we would expect to see a large error in a very few directions, and minimal error elsewhere.

Extending that same argument, we would expect the opposite for larger winds: minimal error spread over a larger spatial extent. Figure 47 clearly shows the increase in the normalized error width ratio with increasing wind speed (i.e. the radiance from the cloud is spread due to the increasing surface waves).

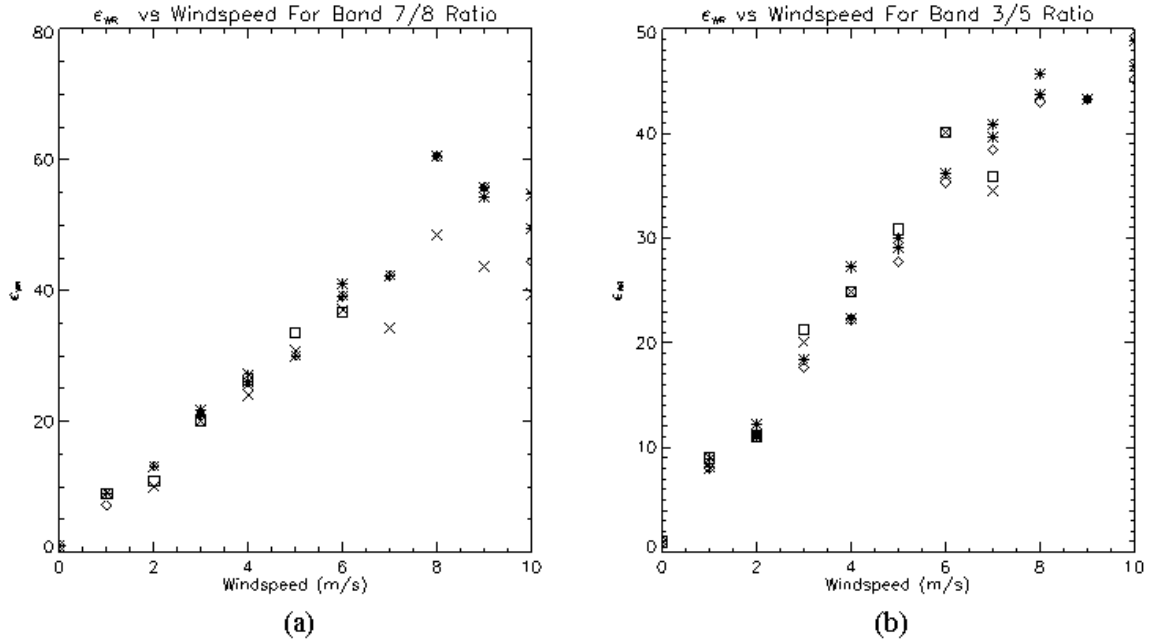


Figure 47: Normalized Error Width Ratio for the error in both the Bands 7/8 ratio at the sensor and the water leaving Band 3/5 ratio. Note the increase with wind speed indicative of the spread in the wave facet slope probability density function.

Note that from wind speeds of roughly 5m/sec to 10m/sec, the normalized error width ratio doubles. That means that twice the solid angle has an error value of at least half the peak error value. Yet, the peak error values for both the sensor reaching Band 7/8 ratio and the water leaving Band 3/5 ratio (Figure 45 and Figure 46 respectively) show very little change between wind speeds of 5m/sec and 10m/sec.

Finally, the chlorophyll content that would be calculated given perfect atmospheric subtraction is given in Figure 48 (a) for the original SeaWiFS algorithm and Figure 48 (b) for the new algorithm. In almost all cases, the chlorophyll content is underestimated from the no cloud case (solid lines).

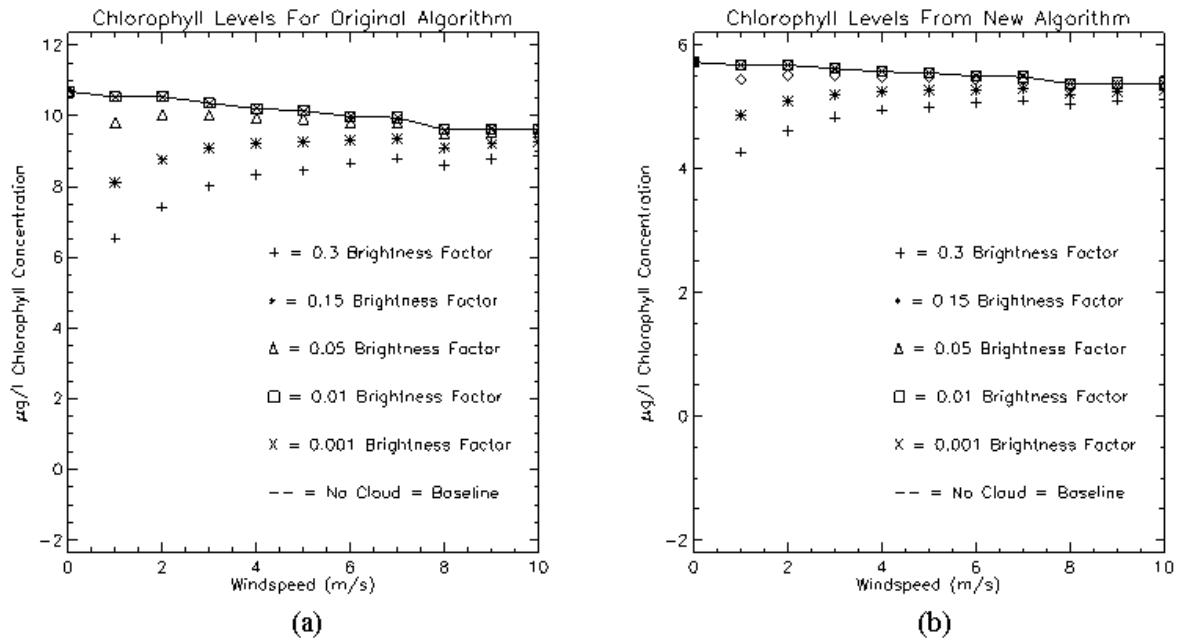


Figure 48: Calculated Chlorophyll levels using the original (a) SeaWiFS algorithm and the new (b) SeaWiFS algorithm for wind speeds ranging from 0.0m/sec and 10.0m/sec and cloud brightness factors ranging from 0.3 to 0.001. The solid line is the no cloud or baseline that each of the SeaWiFS algorithms would calculate in the absence of clouds.

Further, in almost all cases, the chlorophyll content is underestimated from the true value as well. In fact, the new SeaWiFS algorithm underestimates the chlorophyll content in this scenario 100% of the time by at least 4  $\mu\text{g/l}$  which is 40% of the true simulated value.

### The Impact With Respect to Water Quality

A few limited runs using different water quality parameters were performed. Specifically, pure water, moderately clear water (4  $\mu\text{g/l}$  chlorophyll concentration, 2g/m<sup>3</sup> of suspended mineral concentration, and 1g/m<sup>3</sup> of DOM), and more turbid water

(10 $\mu$ g/l chlorophyll concentration, 12g/m<sup>3</sup> of suspended mineral concentration, and 4g/m<sup>3</sup> of DOM) cases were used. The results of the peak error as a function of cloud brightness are presented in Figure 49 for the  $\rho_t(765\text{nm})/\rho_t(865\text{nm})$  and  $\rho_w(490\text{nm})/\rho_w(555\text{nm})$  error parameters.

We see that the affect of the cloud on the two error parameters is a function of what is in the water. High DOM, chlorophyll, and SM will allow the clouds to have a higher impact evidenced by the larger error values in both the water leaving Band 3/5 ratio (as high as 40% error) and the sensor reaching Band 7/8 ratio. Since the cloud impact for high DOM and SM levels is to overestimate the chlorophyll and the high

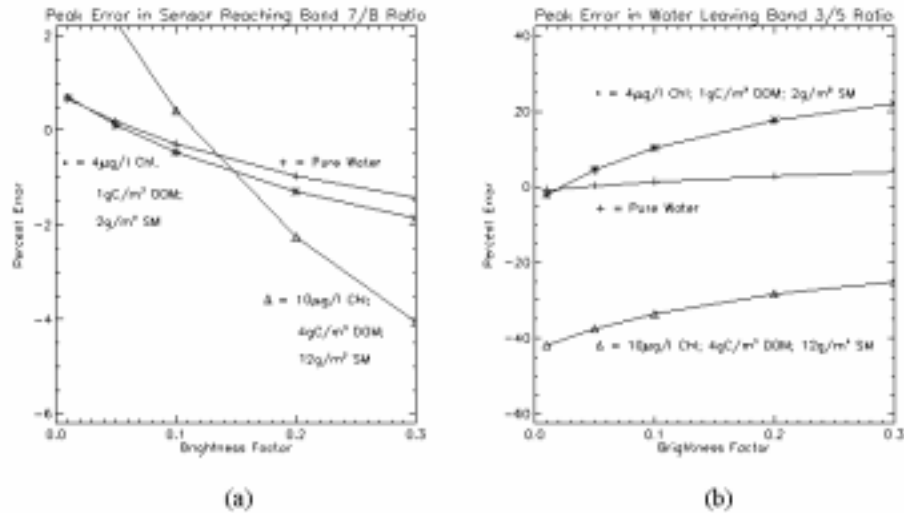


Figure 49: Percent Error both the sensor reaching Band 7/8 ratio and the water leaving Band 3/5 ratio for pure water, semi-clean water, and more turbid water. The pure water (+) is the least affected by the clouds; the semi-clean water (\*) had 4 $\mu$ g/l of chlorophyll, 2g/m<sup>3</sup> of suspended material, and 1gC/m<sup>3</sup> of dissolved organic matter. Higher levels of SM (12g/m<sup>3</sup>) and DOM (4gC/m<sup>3</sup>) are found in the third data set ( $\Delta$ ) (along with 10 $\mu$ g/l of chlorophyll) to allow the clouds to have a higher impact on the percent error for both the ratio parameters.

DOM and SM themselves cause an underestimate in the true chlorophyll levels (if the atmosphere is determined and correctly subtracted) then the errors may cancel each other out. That conclusion is drawn from Figure 50.

The baseline calculated chlorophyll content for the three cases are plotted in Figure 50 with solid lines and the appropriate symbols representing the case. The impact of the cloud for each of the cases is also plotted without the solid line. For the pure water case, the cloud had such a minimal impact on the calculation, that the two lines (+) nearly overlay. The water with higher levels of chlorophyll, DOM, and SM ( $\Delta$ ) shows the largest difference in the calculated chlorophyll content between the baseline and the cloud impacting data. However, both the original SeaWiFS algorithm and the new SeaWiFS algorithm underestimated the true levels (baseline) for the more turbid water. For the moderately clean water, both SeaWiFS algorithms were fairly close to the true levels, but the original algorithm caused an overestimate. The clouds served to lower the chlorophyll estimates in both algorithms for the moderately clear water.

However, we still have the matter of subtracting out the atmospheric affects and the data show much larger Band7/8 ratios for the water with higher levels of SM and DOM. In the earlier analysis and throughout the literature review presented earlier, we determined that more SM in the water would negate the assumption of  $\rho_w(765\text{nm})$  and  $\rho_w(865\text{nm})$  equal to zero. In my error analysis presented here, I'm removing that error from consideration by comparing the cloud data to the data



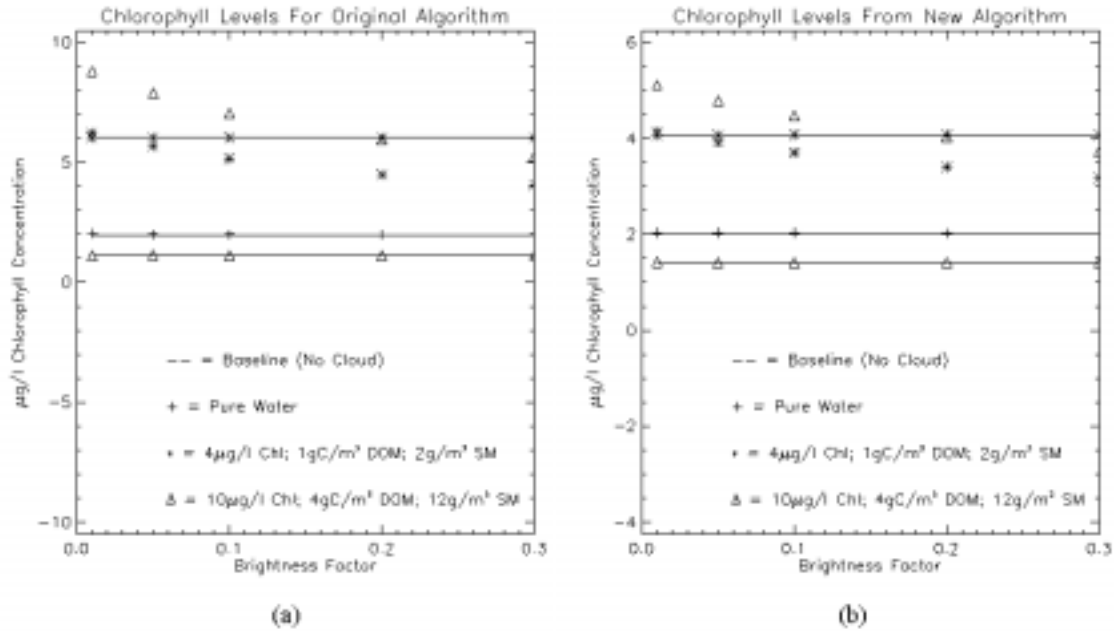


Figure 50: Calculated chlorophyll content for the three water cases used in Figure 49. To make these calculations, the assumption is made that the exact atmosphere can be removed to get to the water leaving radiance (and reflectance) values. We see from these data that the higher levels of SM, DOM, and Chlorophyll ( $\Delta$ ) allow the clouds to impact the estimates more than the lower levels.

without a cloud. The fact that the baseline (the data without a cloud) has non-zero  $\rho_w(765\text{nm})$  and  $\rho_w(865\text{nm})$  is not considered as part of the cloud impact study. I will address that later in a limited sense (see “SM Or Clouds” on page 125).

Another limited case was run with a single cloud brightness factor (0.20) and several levels of chlorophyll content. Chlorophyll levels from  $20\mu\text{g/l}$  to  $0\mu\text{g/l}$  with a low DOM level of  $1.0\text{gC/m}^3$  and a low SM level of  $0.1\text{g/m}^3$  were used. The results are plotted in Figure 51 and Figure 52.

In Figure 51 we see the error in the Band 7/8 ratio at the sensor and the water leaving Band 3/5 ratio can get quite high on a percent error basis. However, in Figure 52 we see that that does not greatly impact the actual chlorophyll calculations. Note

that in Figure 52(b) the new SeaWiFS algorithm quite accurately predicts the true chlorophyll level in the no-cloud case. That conclusion is reasonable considering that the algorithms were derived for Case I waters and the water used in this scenario is roughly Case I.

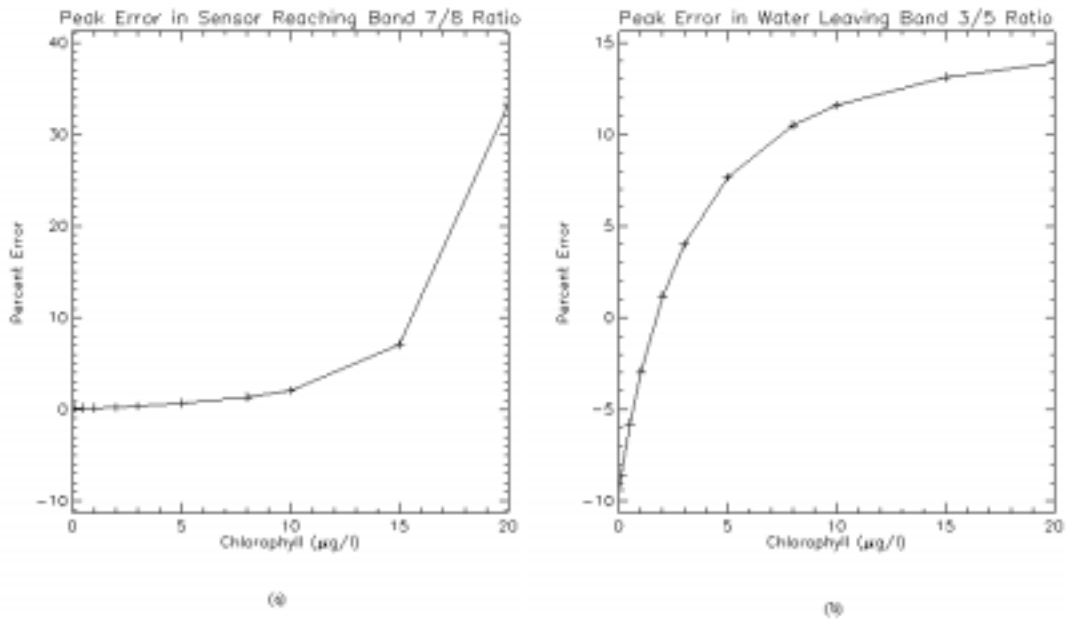


Figure 51: Percent Error for the Band 7/8 ratio (at the sensor) and the Band 3/5 ratio (at the water surface). These apparently large errors caused by the cloud imply an under estimation of chlorophyll if the error is positive and an over estimation if the error is negative. However, when the actual ratios are used to calculate the chlorophyll levels, we see very little error in the final result.

## The Impact With Respect to Atmosphere Model

The final impact area concerns varying the atmospheric aerosols. For this analysis, I used several MODTRAN generated atmospheres and varied the cloud brightness factor. The error in the Band 7/8 ratio at the sensor and error in the water

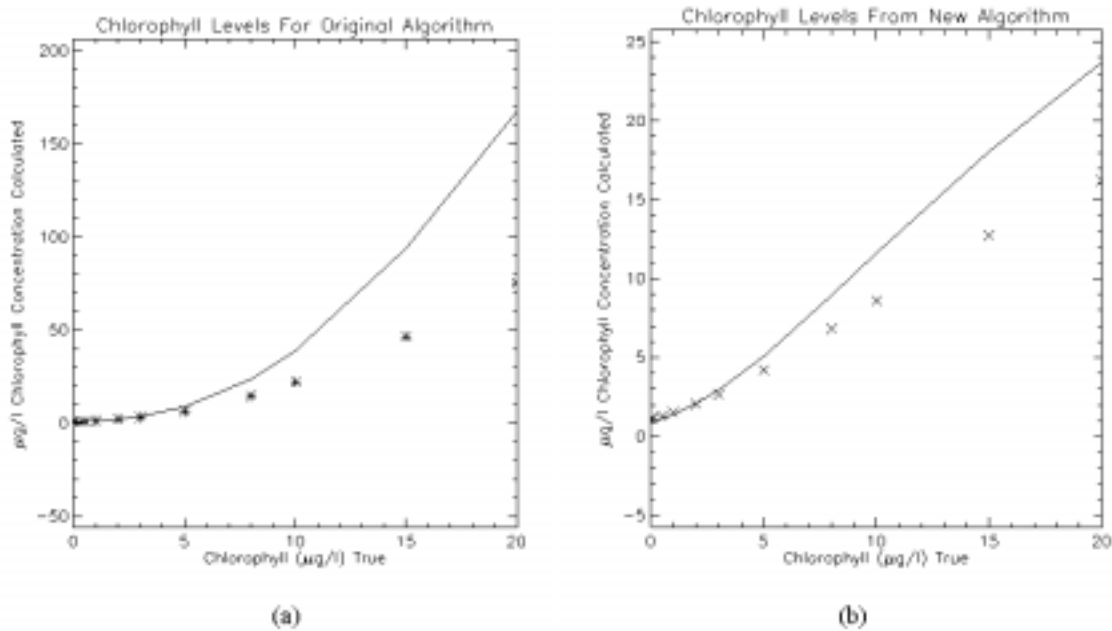


Figure 52: Calculated Chlorophyll content using the original (a) and the new (b) SeaWiFS algorithms. Given the errors plotted in Figure 51, we might expect larger error here. That is not the case for these relatively clean waters. (DOM=1.0gC/m<sup>3</sup> and SM=0.1g/m<sup>3</sup>). The maximum miss-calculation is 1.4  $\mu\text{g/l}$  in the original algorithm and 0.12 in the new algorithm. (NOTE: The data and the words don't match—I'm double checking which is wrong and which is right)

leaving Band 3/5 ratio are shown in Figure 53 for five IHAZE values. The cloud used for the data in Figure 53 occupied a solid angle of 0.083 sr beginning at a 10° declination angle and extending from 45° azimuth to 90° azimuth with a brightness factor ranging from 0.3 to 0.01. We expect to view the largest impact due to this cloud between 10° and 30° in declination angle and between 225° and 270° in azimuth. That expectation is met.

The atmospheres used to generate the data in Figure 53 differed only in the MODTRAN “IHAZE” parameter. Three IHAZE values were for fairly clear conditions and two represented hazier conditions (5km visibility). The three clear atmospheres

used an IHAZE value of 1 which equates to a rural extinction with 23 Km visibility, an IHAZE value of 4 which equates to a Maritime extinction with 23 KM visibility, and an IHAZE value of 6 which equates to a tropospheric extinction with 50 Km visibility. The two hazier atmospheres used an IHAZE of 2 which equates to a rural

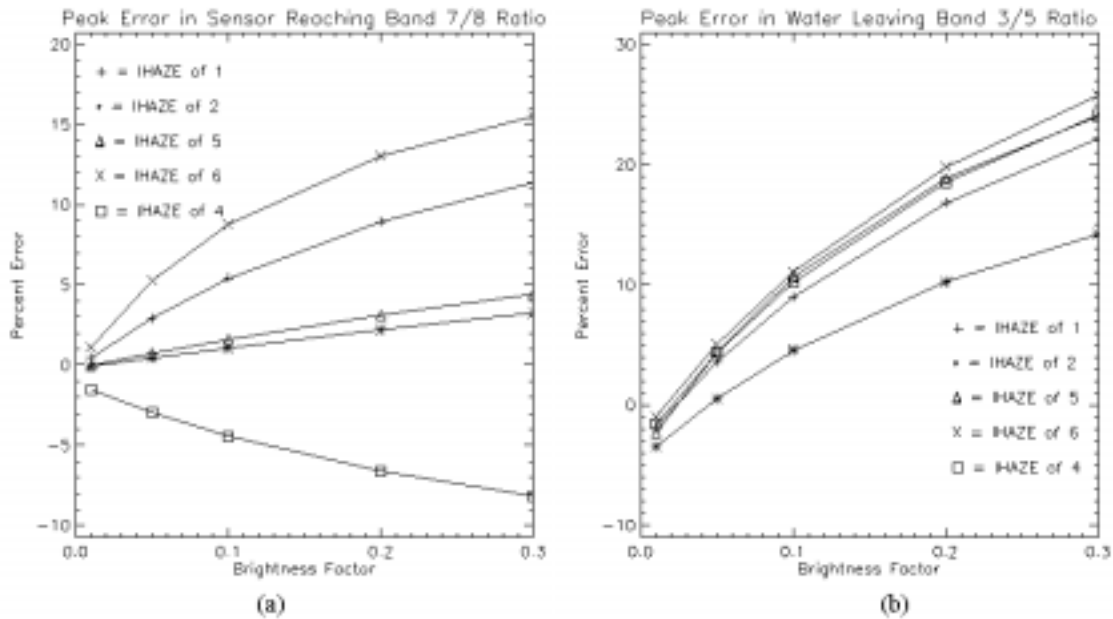


Figure 53: The sensor Reaching Band 7/8 ratio error and Water Leaving Band 3/5 Ratio Error. The cloud occupied a solid angle of 0.083 sr beginning at 10° declination angle and extending from 45° azimuth to 90° azimuth. The largest impact due to the cloud is between 10° and 30° in declination angle and between 225° and 270° in azimuth as expected. The four curves in each of (a) and (b) represent four different IHAZE parameters. An IHAZE of 1 (+) represents a rural extinction with 23Km visibility. An IHAZE of 2 (\*) represents a rural extinction with 5Km visibility. An IHAZE of 4 (□) represents a Maritime extinction with 23 KM visibility. An IHAZE of 5 (Δ) represents an urban extinction with 5Km visibility. Finally, an IHAZE of 6 (X) represents a tropospheric extinction with 50Km visibility. In (a) the two hazier atmospheres (IHAZE of 2 and 5) show less impact due to the cloud on the ratio between bands 7 and 8 at the sensor than do the clearer atmospheres (IHAZE 1, 4, and 6). No such separation is apparent in the water-leaving Band 3/5 ratio data found in (b).

extinction with 5km visibility and an IHAZE of 5 which equates to an urban extinction with 5km visibility. The two hazier atmospheres allow the cloud to impact the sensor reaching Band 7/8 ratio much less than the two clear atmospheres as seen in Figure 53(a). This results from lower transmission coefficients and higher overall

upwelled radiance from the hazier atmospheres. Even though the cloud has less impact, the atmosphere itself more than compensates because there is more of it to remove.

That means that even though I've shown that there is less error in the parameter used to determine the amount of atmosphere to subtract [via  $\rho_a(490\text{nm}) + \rho_{Ra}(490\text{nm})$  and  $\rho_a(555\text{nm}) + \rho_{Ra}(555\text{nm})$ ], there is still more overall atmosphere. Secondly, with the upwelled radiance occupying a larger share of the total sensor reaching radiance, the error in chlorophyll content determination generated by the incorrect Band 7/8 ratio is still unknown. Therefore, we can not conclude that a cloud in the hazier atmosphere will have less impact nor can we conclude that it will have more impact.

We can, however, proceed as before and assume that the correct atmosphere was subtracted in each case and assess the impact on the water leaving Band 3/5 ratio as in Figure 53(b). Here we see no specific distinction between the hazier atmospheres and the clear atmospheres. These error rates equate to chlorophyll content as calculated and displayed in Figure 54(a) and (b).

The water leaving Band 3/5 ratio error is generally positive for all four atmospheres used for Figure 54 which equates to, again, an underestimate of the chlorophyll content. That conclusion is supported by the data in Figure 54 for both the original SeaWiFS algorithm (a) and the new SeaWiFS algorithm (b). Note again

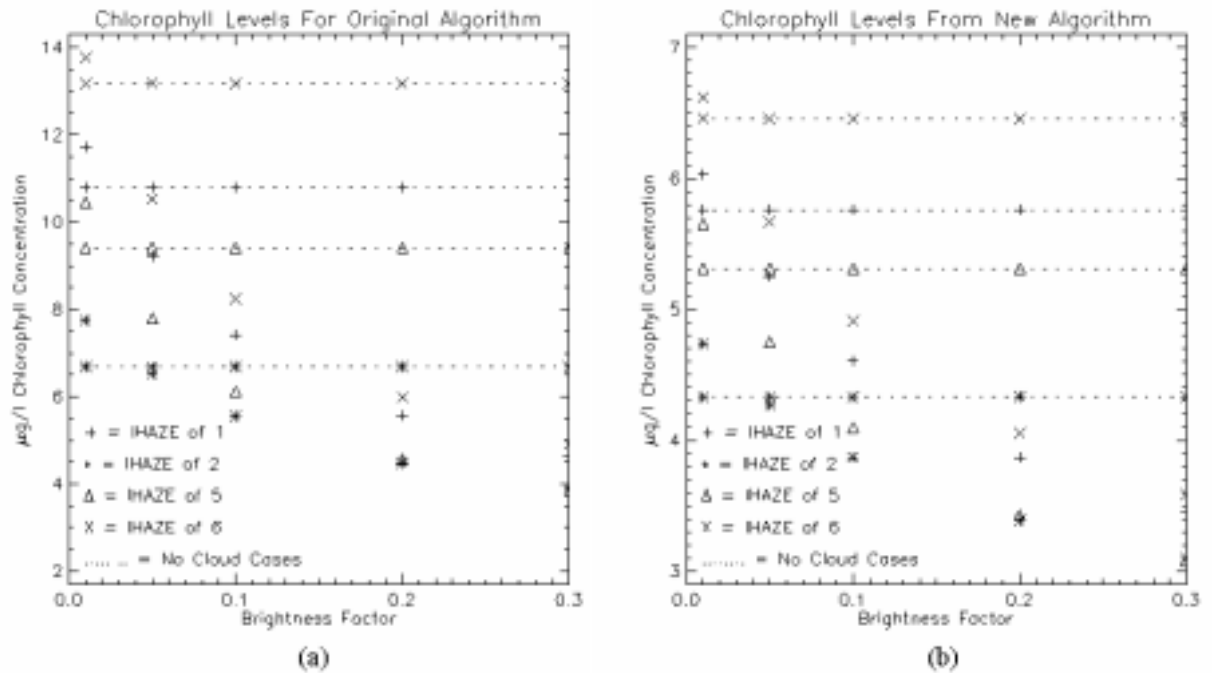


Figure 54: The Calculated Chlorophyll Content with Varying Atmospheres. The chlorophyll content that would be calculated from the Band 3/5 ratios in Figure 53(b) is plotted for both the original SeaWiFS algorithm (a) and the new SeaWiFS algorithm (b). The different atmospheres represent four different MODTRAN IHAZE parameters. An IHAZE of 1 (+) represents a rural extinction with 23Km visibility. An IHAZE of 2 (\*) represents a rural extinction with 5Km visibility. An IHAZE of 5 (Δ) represents an urban extinction with 5Km visibility. Finally, an IHAZE of 6 (X) represents a tropospheric extinction with 50Km visibility. In (a) the two hazier atmospheres (IHAZE of 2 and 5) show less impact due to the cloud on the ratio between bands 7 and 8 at the sensor than do the clearer atmospheres (IHAZE of 1 and 6).

that even without the clouds, the chlorophyll content is underestimated from the true content (10µg/l) in all cases using the new algorithm. The original algorithm would sometimes overestimate and sometimes underestimate the chlorophyll without the cloud impact. (The clearer atmospheres induced an overestimate and the hazier atmospheres induce an underestimate.)

## **SM Or Clouds**

The data review and cloud impact analyses are complete. The major question that remains to be answered is: “Which is a bigger problem, suspended minerals or clouds?” With the existence of the end-to-end radiative transfer tool created here, we can try to answer this question.

Using the current algorithms, the ultimate impact comparison would be in calculated chlorophyll content versus changes in “normal” SM concentrations and “normal” clouds for different levels of chlorophyll. Using this method we could easily compare the chlorophyll estimates with the “true” values to derive the impact. However, we expect that suspended minerals will have the largest impact on the atmospheric subtraction routines and the empirical database for those routines is not available. The first attempt, then, failed due to the lack of the database. My second attempt at the comparison met with more disastrous results.

Without the atmospheric subtraction database I could not use the current algorithm, so I reverted to the older CZCS algorithms. With anything in the water other than 0.25  $\mu\text{g/l}$  of chlorophyll or less this method failed miserably and it was not possible to answer the SM versus clouds question. Attempt number three fared much better.

The sensor reaching Band 7/8 ratios and the water leaving Band 3/5 ratios themselves can be compared. (Comparing the error rates would not be helpful in this case. Only the actual ratios will help answer the question.) As SM concentrations

change and as cloud brightness factors change, the two key ratios will change. The highest change will provide the highest impact. Though this method seems to imply that a series of derivatives should be used, I did not compute them. However, we can still answer the questions using the ratios and the apparent derivatives as in Figure 55.

In Figure 55 I've plotted the means of the two key ratios for chlorophyll content of  $1.0\mu\text{g/l}$  at several SM concentrations (0, 1, 5, 10, and  $15\text{ g/m}^3$ ) and four cloud brightness factors: baseline (i.e. no cloud); 0.2; 0.1; and 0.05. The means were computed for two sections. In (a) and (b) the means are over all directions outside of the sun glint and cloud glint regions and in (c) and (d) the means are over the cloud glint region alone.

We can see from these data that outside of the cloud specular region, (a) and (b) in Figure 55, the largest changes occur when the suspended minerals change. In Figure 55(a), the sensor-reaching Band 7/8 ratio change is relatively constant over the range of SM concentrations used no matter what the cloud brightness factor was. However, in Figure 55(b) we see that the water leaving Band 3/5 ratio has the largest change for low SM concentrations and minimal changes once the concentration is above  $1.0\text{g/m}^3$  or so. Again, these changes are roughly the same for all of the cloud brightness values used.



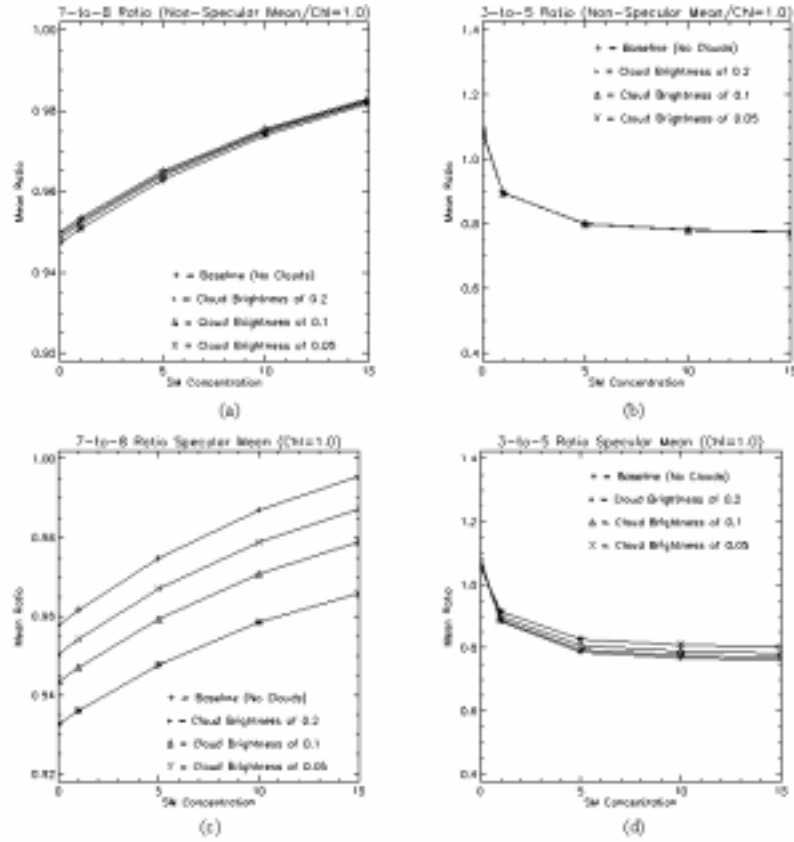


Figure 55: Suspended Mineral and Cloud Changes at a Chlorophyll level of  $1.0 \mu\text{g/l}$ . The means of the two key ratios for chlorophyll content of  $1.0 \mu\text{g/l}$  at several SM concentrations (0, 1, 5, 10, and  $15 \text{ g/m}^3$ ) and four cloud brightness factors: baseline (i.e. no cloud); 0.2; 0.1; and 0.05. The means were computed for two sections. In (a) and (b) the means are over all directions outside of the sun glint and cloud glint regions and in (c) and (d) the means are over the cloud glint region alone.

In Figure 55(c) and (d), that is not the case. In the cloud specular region, the cloud could impact the two key ratios as much or more than the suspended minerals. In fact, above  $5 \text{ g/m}^3$ , the largest variation in the water leaving Band 3/5 ratio comes from the changes in the cloud brightness factor. (As the SM concentration rises from  $5 \text{ g/m}^3$  to  $15 \text{ g/m}^3$  the water leaving Band 3/5 ratio stays nearly constant. Yet, over the same range, as the cloud brightness factor changes, large changes occur in the water

leaving Band 3/5 ratio.) Similar data and results are obtained for chlorophyll levels of 0.1 $\mu$ g/l and 10.0 $\mu$ g/l and at different levels of DOM concentration.

These results are consistent with the cloud analysis performed here and the SM studies in the literature. Bukata (1997) has indicated that any appreciable concentrations will greatly impact the water's chromaticity (and, thus, the ratios of the volume reflectance for two different wavelengths). He further states that after the initial fast changes, the chromatic behavior asymptotically approaches a constant value. Such a behavior is found in Figure 55(b) and (d).

### **Summary of Results**

With the exception of the one section on varying water conditions, all of the analysis used nominal Lake Ontario waters of 10  $\mu$ g/l of chlorophyll content, 2.0gC/m<sup>3</sup> of Dissolved Organic Matter, and 6.0g/m<sup>3</sup> of Suspended Materials. Also, Maritime, Rural, Urban, and Tropospheric aerosol extinctions were used with visibilities ranging from 5 km to 50km. Cloud impacts were derived for varying the cloud brightness factor, the cloud location, the cloud to cloud+sky ratio, the shape of the clouds, the water conditions, the wind speed, and the atmospheric aerosol IHAZE parameter.

We showed that varying the cloud brightness factor impacts both of the key SeaWiFS parameters, the sensor reaching  $\rho_t(765\text{nm})/\rho_t(865\text{nm})$  and the water leaving  $\rho_w(490\text{nm})/\rho_w(555\text{nm})$ . However, the impact was localized to the viewing angle 180° in azimuth away from the cloud at roughly the same declination angle. The only

spread outside that quad (parameterized with the normalized error width ratio) was due to the surface wave orientation changes with wind speed. The overall affect of the white clouds was to underestimate the chlorophyll content for the water conditions used.

The location of a single cloud affects the estimated chlorophyll content similarly, but the larger Fresnel reflectance (i.e. cloud glint) of high declination angle clouds cause a larger impact. Further affects were shown in the normalized error width ratio. With the quad partitioning used by HydroMod, larger declination angles would necessarily have larger solid angles and a correspondingly smaller  $\epsilon_{WR}$ .

The size of the cloud was shown to effect the peak error in both  $\rho_t(765nm)/\rho_t(865nm)$  and  $\rho_w(490nm)/\rho_w(555nm)$ . Larger clouds provide correspondingly more radiance to the water surface and affect the error parameters similarly. Larger cloudbanks also helped keep the normalized error width ratio close to 1.0.

Wind speed was shown to affect both the peak errors and the normalized error width ratio. As the wind speed increased, the peak error decreased slightly and spread to more quads. This was evidenced as a steadily increasing normalized error width ratio. The peak error did not decrease at the same rate as  $\epsilon_{WR}$  increased for any of the cloud brightness factors shown. The exception to that conclusion is at very low wind speeds (less than 2m/sec). In that case, the peak decreased rapidly from the

specular case (0m/sec and  $\epsilon_{WR}=1.0$ ) to cases similar to the PDF's given by Cox and Munk in EQ 5.

The analysis carried further than just the impact on the key parameters,  $\rho_t(765nm)/\rho_t(865nm)$  and  $\rho_w(490nm)/\rho_w(555nm)$ , and into the actual calculation of the chlorophyll content using both the original SeaWiFS algorithm (EQ 31) and the new SeaWiFS algorithm (EQ 33). In all of those calculations, perfect atmospheric subtraction is assumed. In almost all of those chlorophyll predictions, the impact of the clouds is to underestimate the chlorophyll content.

The water content was also changed and the brightness factor variation was presented. For clearer water, the overestimate of chlorophyll caused by the cloud was evident. For less clear water, the reverse was true.

Finally, different atmospheres were selected and the affects on the key parameters were derived. It was demonstrated that hazy atmospheres have less error in the  $\rho_t(765nm)/\rho_t(865nm)$  atmospheric correction parameter, but they also have more atmosphere for which to correct. The hazier atmospheres also resulted in an underestimate of the chlorophyll content using  $\rho_w(490nm)/\rho_w(555nm)$ ; this was consistent with normal results using a clear atmosphere with the standard water conditions.

## **Operational Impact of Results**

Future algorithms for monitoring water quality parameters via remote sensing may wish to consider the impact of clouds on the remotely sensed data. From the results and cloud impact analysis performed and presented here, we can determine some of the operational considerations that should be included in those future algorithms.

I've shown in the analysis that the clouds' specular direction is the direction of peak error due to clouds. Further, the "width" of the error depends on wind speed and, to a lesser extent, on the clouds' declination angle. Therefore, operationally we may want to look for clouds in the scene that are at or near the specular direction of the sensor's look angle. The term "near" would be largely a function of the wind speed. Outside of the specular direction and "near" the specular direction, the cloud impact seems to be minimal. Also, the amount of impact (other than direction) is not affected by the wind speed for speeds greater than about 2m/sec.

Since the cloud brightness factor plays a large roll in the cloud impact, a method is required to determine that relative factor at the point of interest on the water surface. This method would most likely account for the sun and cloud location, the type of cloud in question, the size and shape of the cloud, and the number of clouds in the scene. A (currently non-existing) database of cloud brightness factors with respect to those variables is required to derive such a method.

Another operational impact concerns the atmosphere itself. The wide variation in impact due to the changes in IHAZE parameters suggests separate atmospheric correction algorithms for different operational regimes. That is, over the Laurentian Great Lakes we would never have a Maritime atmosphere (since it contains a salt content) so why use an algorithm that was derived primarily for the Maritime conditions? A new algorithm (or perhaps the same algorithm with different parameters) is required to take advantage of this non-Maritime fact.

The atmosphere and its subtraction from the data remain the key component in monitoring the water quality parameters. As such, most of the effort should be spent in this area. A new algorithm specifically derived for use over the Laurentian Great Lakes would be a major step in improving the estimates of water quality parameters. The specular region once again is the only area of concern when correcting for clouds as part of the atmospheric subtraction routines. Once the atmospheric component is correctly removed from the data, the water leaving component can be effectively addressed.

Specifically, new algorithms are again required for deriving the water quality parameters in the presence of high suspended mineral concentrations. (In fact, they are required in the presence of *any* suspended mineral concentrations.) The same applies for higher chlorophyll concentrations; however, the new SeaWiFS algorithm is much better than the original SeaWiFS algorithm. It was also shown that the higher concentrations of suspended minerals and/or chlorophyll will impact the key ratios

much more than clouds for directions other than near the cloud specular direction. Since that can be a larger number of directions (depending on the amount of cloud cover and the wind speed), more accurate algorithms are needed. Further, even near the specular direction the algorithms need to work for the higher concentrations before we even consider the clouds.

Therefore, operationally we need to worry about and correct for clouds at or near the specular direction only and only after better atmospheric correction algorithms and better water-quality-parameter-algorithms are created. HydroMod can help create such algorithms.





## *Chapter 6*

### **CONCLUSIONS**

#### **Summary of Contributions**

The major contributions from this work to the field of remote sensing over water include:

1. The creation of the entire end-to-end model;
2. The incorporation of a realistic cloud model in the study of radiative transfer over water; and
3. The characterization of the impact of clouds to the radiance reaching the SeaWiFS sensor along with the derived chlorophyll content.

HydroMod, the end-to-end radiative transfer model created for this study, is an extremely valuable tool for developing and evaluating algorithms for retrieval of water parameters. Even for a cloud free sky, such a model has not been reported in the literature. This report does not cover HydroMod in and of itself. Appendix I contains a Users Manual for HydroMod and Appendix II contains some additional information concerning HydroMod. All of the decisions and conclusion drawn in the body of this work were incorporated into HydroMod as part of the end to end model. (Other items,

such as radiance sources internal to the water body were also included in HydroMod, but were not discussed here.)

MODTRAN has become the industry standard for many atmospheric and/or land based radiative transfer derivations due to its accuracy. However, using MODTRAN to provide the input to an underwater module is unique. Further, using the MODTRAN radiance values along with the Cox and Munk water surface orientation to get the true downward radiance distribution below the surface,  $L_{\lambda}^{\downarrow}(\theta, \phi)$ , allows accuracy that is rarely achieved for such a complex problem. The model is very valuable if it were only used to study water quality algorithms or water quality detection schemes. Adding cloud inputs makes the model even more valuable.

The cloud model is both simple and elegant. Instead of endeavoring to accurately model these complex and nebulous blobs of water and ice, calculate a BDRF, determine the total input radiance from all directions, and then calculate the radiance to the point of interest, we chose to simply model the radiance to the point of interest. The key bit of good luck with the cloud model is that the spectral response curves for all of the MODTRAN generated clouds were extremely similar. Instead of having a family of cloud spectral response curves, a single curve could be used. HydroMod, however, allows for that curve to be changed at the users' discretion. This allows the advantage of

being able to model an exact scene using spectralradiometer measurements from the true clouds in the vicinity. Without the cloud model, the cloud impact analysis could not have been completed.

The cloud impact analysis is required so that we may know when and how clouds impact (or could impact) the conclusions drawn from the remotely sensed data. The failures noted in the introduction concerning SeaWiFS calculated chlorophyll levels (i.e. the reason that generated the requirement to study the impact of clouds) tended to be when SeaWiFS predicted too much chlorophyll. However, one of the main findings here is that for most normal Lake Ontario waters, the impact of clouds should be a lower chlorophyll prediction. The main exception to that finding occurs in the presence of hazier atmospheres.

A full summary of all of the results from the cloud impact study can be found at the end of that chapter.

## **Recommendations**

Though all requirements set forth in the proposal were met (and exceeded in most cases), there are some other areas of interest that should be pursued. Many such recommended pursuits center on the use and future improvements for HydroMod.

Other recommendations are in the area of further cloud impact studies and SeaWiFS chlorophyll content derivations and failures.

With the remote sensing over water end-to-end radiative transfer tool in hand, we can begin to build large databases of look up tables for various water and atmospheric conditions. This will most likely occur. However, we could take full advantage of the linearity of the results by using a “sky” input of only a single component from one declination angle. A series of these single cases for each declination angle is required. For the HydroMod high-resolution data, there are 18 declination angles to consider; in the low-resolution mode there are 10. Using the results of each one of these 10 (or 18) cases, we can artificially create the results from any sky input. Linearly scaling, rotating, and summing copies of results from the original 10 (or 18) runs can do this.

I highly recommend performing a few simple test cases that include all of the functionality of HydroMod. There will be some cases where it works very well and exact results are obtained. Yet, there may be some cases (like when using radiance sources internal to the water body as a possibility) that are not practical.

Another set of look up tables can be generated that uses only the total absorption coefficient and total scattering coefficient as variables. From this set of look up tables, whenever chlorophyll, DOM, and SM concentrations and cross sectional data are selected, a new set of look up tables can be easily generated. When using this recommendation, we need to note three caveats: (1) that it would not apply

if internal sources were included; (2) it only applies if the bottom is not a factor; and (3) the water body is assumed homogeneous. A major advantage to this approach is that the data do not need to be run spectrally. The spectral content only applies when we use an absorption or scattering cross section. That means that the spectral character comes out when generating the specific results for the selected concentrations and cross sections.

If HydroMod is going to be around for a long time, I recommend vectorizing the Hydrolight Fortran code to speed up processing. We could also replace the method used for the Riccati equation integration; the Hydrolight method of a fourth order Runge-Kutta algorithm is the normally recommended method for solving differential equations, but simpler and faster methods are available that should provide just as much accuracy a lot faster. (Since the attenuation and scattering of light underwater are well-behaved smooth functions, we shouldn't need the fourth order Runge-Kutta method used by Hydrolight.)

Concerning further analysis of the cloud impact study, the next phase should be to clean up some of the missing components. For instance, more analysis should be done with different atmospheres and different water content with the goal of creating new and improved algorithms for use over the Great Lakes and/or coastal regions. The limited range presented here was both more than originally planned and far from completing the whole job. It did, however, point to the need for more work in those areas.

Notwithstanding the need for the improved algorithms, correcting for the cloud impact on the chlorophyll content can be attacked starting now. All of the tools are in place to perform the required analysis. However, based on the results here and until we get more data from different water content and different atmospheres, there may not be a need to correct the SeaWiFS algorithms. We may be trading one bad estimate for another bad estimate.

## **APPENDIX I**

### **A HydroMod Users Manual**





## APPENDIX II

### HydroMod Additional Information







## BIBLIOGRAPHY

Barker, H. W. and J. A. Davies, "Solar radiative fluxes for stochastic, scale-invariant broken cloud fields", *Journal of the Atmospheric Sciences*, Vol. 49, pp. 1115-1126, 1992

Barker, H. W. and J. A. Davies, "Cumulus cloud radiative properties and the characteristic of satellite radiance wavenumber spectra", *Remote Sensing of the Environment*, Vol. 42, pp. 51-64, 1992

Barnes, Robert A., William L. Barnes, Wayne E. Esaias, and Charles R. McClain, "Volume 22, Prelaunch Acceptance Report for the SeaWiFS Radiometer", September 1994

Barnes, Robert A. , Alan W. Holmes, William L. Barnes, Wayne E. Esaias, Charles R. McClain, and Tomas Svitek, "Volume 23, SeaWiFS Pre-launch Radiometric Calibration and Spectral Characterization", October 1994.

Bartlett, Jasmine S., Kenneth J. Voss, Shubha Sathyendranath, and Anthony Vodacek, "Raman scattering by pure water and seawater", *Applied Optics*, Vol.37, No. 15, pp 3324-3332, 20 May 1998.

Bird, R. E., and C. Riordan, "Simple solar spectral model for direct and diffuse irradiance on horizontal and tilted planes at the earth's surface for cloudless atmospheres", *Journal of Climatology and Applied Meteorology*, Vol 25 p 87-97, January 1986.

Bukata, R. P. , J.H. Jerome, J. E. Bruton, and S. C. Jain,, "Nonzero subserface irradiance reflectance at 670nm from Lake Ontario water masses", *Applied Optics*, Vol. 19, pp. 2487-2488, 1980

Bukata, R. P. , J. E. Bruton, J.H. Jerome, S. C. Jain, and H. H. Zwick, "Optical water quality model of Lake Ontario. 1: Determination of the optical cross sections of organic and inorganic particulates in Lake Ontario", *Applied Optics*, Vol. 20, No. 9, pp. 1696-1703, 1 May 1981

Bukata, R. P. , J. E. Bruton, J.H. Jerome, S. C. Jain, and H. H. Zwick, "Optical water quality model of Lake Ontario. 2: Determination of chlorophyll-a and suspended mineral concentrations of natural waters from submersible and low altitude optical sensors", *Applied Optics*, Vol. 20, No. 9, pp. 1704-1714, 1 May 1981

Bukata, Robert P., John H. Jerome, Kirill Ya. Kondratyev, and Dimitry V. Pozdnyakov, "*Optical Properties and Remote Sensing of Inland and Coastal Waters*", New York: CRC Press, ISBN 0-8493-4754-8, 362 pages, 1995.

Bukata, Robert P; John H. Jerome, Kirill Ya Kondratyev, Dimitry V Pozdnyakov, and Alexander A. Kotykhov, "Modelling the radiometric color of inland waters: implications to a) remote sensing and b) limnological color scales", *Journal of Great Lakes research*. Volume 23, Number 3, pp. 254-269, 1997

- Bukata, Robert P. and John H. Jerome, "Extracting Concentrations of Water Colorants from Remotely-Sensed Data", presentation to International Association of Great Lakes Research, McMaster University, Hamilton, ON, 19 May 1998. Contact authors at National Water Research Institute, 867 Lakeshore Road, ON L7R 4A6.
- Carder, K. L., R.G. Steward, G.R. Harvey, and P.B. Ortner, "Marine humic and fulvic acids: Their effects on remote sensing of chlorophyll-a", *Limnology and Oceanography*, Volume 3, pp. 68-81, January 1989.
- Cox, Charles and Walter Munk, "Measurement of the Roughness of the Sea Surface from Photographs of the Sun's Glitter", *Journal of the Optical Society of America*, Vol. 44, No. 11, pp. 838-850, November 1954
- Cox, Charles and Walter Munk, "Some Problems in Optical Oceanography", *Journal of Marine Research*, Vol. 14, No. 1, pp. 63-78, 1955
- Cox, Charles and Walter Munk, "Slopes of the Sea Surface Deduced from Photographs of Sun Glitter", *Bulletin Scripps Institute of Oceanography of the University of California*, Vol. 6, No. 6, pp. 401-488, 1956
- Duntley, Seibert Q., "Measurements of the Distribution of Water Wave Slopes", *Journal of the Optical Society of America*, Vol 44(7), pp. 574-575, July, 1954.
- Duntley, Seibert Q., "Light in the sea", *Journal of the Optical Society of America*, Vol 53, pp. 214-233, February, 1963
- Gordon, Howard R., Otis B. Brown, and Michael M. Jacobs, "Computed relationships between the inherent and apparent optical properties of a flat homogeneous ocean", *Applied Optics* Vol. 14 No.2, pp. 417 - 427, February 1975.
- Gordon, Howard R., Menghua Wang, "Retrieval of water-leaving radiance and aerosol optical thickness over the oceans with SeaWiFS: a preliminary algorithm", *Applied Optics* Vol. 33 No.3, pp. 443 - 452, January 1994.
- Gordon, Howard R., "Atmospheric correction of ocean color imagery in the Earth Observing System era", *Journal of Geophysical Research*, Vol. 102, No. D14, pp. 17,081 - 17,106, July 27, 1997
- Gregg, Watson W. and K. L. Carder, "A simple spectral solar irradiance model for cloudless maritime atmospheres", *Limnology and Oceanography*, Vol 35, No. 8, pp 1657-1675, December 1990.
- Jerlov, N.G., "*Marine Optics, Elsevier Oceanography Series 14*", Elsevier Publishing Co., Amsterdam, 231 pp. 1976.
- Jerome, J. H., R. P. Bukata, and J. E. Burton, "Utilizing the components of vector irradiance to estimate the scalar irradiance in natural waters", *Applied Optics* Vol. 27, No. 19, pp. 4012-4018, 1 October 1988
- Jerome, J. H., R. P. Bukata, and J. R. Miller, "Remote sensing reflectance and its relationship to optical properties of natural waters", *International Journal of Remote Sensing* pp. 3135-3155, Taylor and Francis Ltd., November 1996.
- Kattawar, George W. and Charles N. Adams, "Errors induced when polarization is neglected in radiance calculations for an atmosphere-ocean system", SPIE Vol. 1749 "*Optics of the Air-Sea Interface*", 1992

Khristoforov, G. N., A. S. Zapevalov, and M.V. Babi, "Statistical Characteristics of Sea Surface Slopes at Different Wind Speeds", *Oceanology*, Vol. 32, No. 3, pp. 300-304, 1992

Kirk, John T.O. "Dependence of relationship between inherent and apparent optical properties of water on solar altitude", *Limnology and Oceanography* Vol. 29 (2), pp. 350-356, 1991

Kirk, John T.O. "Volume scattering function, average cosines and the underwater light field", *Limnology and Oceanography* Vol. 36 (3), pp. 455-467, 1991

Kneizys, F. X., E.P. Shettle, W. O. Gallery, J.H. Chetwynd, Jr., L.W. Abreu, J.E.A. Selby, R.W. Fenn, and R.A. McClatchey, "Atmospheric Transmittance/Radiance: Computer Code LOWTRAN 5", AFGL-TR-80-0067, Air Force Geophysics Laboratory, Hanscom AFB, MA, Optical Physics Division Project 7670, 21 February 1980.

Leckner, B. "The spectral distribution of solar radiation at the earth's surface—elements of a model", *Solar Energy*, Vol 20, pages 143-150, January 1978

Maffione, R.A. 1997. "Theoretical developments on the optical properties of highly turbid waters", to be published in *Limnology. and Oceanography.*,

Maffione, R.A., and D.R. Dana 1997. "Instruments and methods for measuring the backward-scattering coefficient of ocean waters", to be published in *Applied. Optics*

McClain, Charles R., Kevin Arrigo, Wayne E. Esaias, Michael Darzi, Frederick S. Patt, Robert H. Evans, James W. Brown, Christopher W. Brown, Robert A. Barnes, and Lakshmi Kumar, "Volume 28, SeaWiFS Algorithms, Part 1", SeaWiFS Technical Report Series edited by Stanford B. Hooker, Elaine R. Firestone, and James G. Acker. NASA Technical Memorandum 104566, Vol 28, 38 pages plus color plates, June 1995.

Maul, G. A., "Introduction to Satellite Oceanography", Martinus Nijhoff Publishers, Dordrecht, The Netherlands, ISBN 90-247-3096-1, 606 pages, 1985

Mobley, Curtis D. "Light and Water: Radiative Transfer in Natural Waters", Boston, Academic Press, ISBN 0-12-502750-8, 592 pages, 1994

Mobley, Curtis D. "Hydrolight 3.0 User's Guide", SRI International, SRI Project Number 5632 Final Report, Office of Naval Research Contract number N00014-94-C-0062, Menlo Park, CA, 65 pages, March 1995

Mobley, Curtis D., HYDROLIGHT Fortran Computer Code, Version 3.1, March 1995.

Mobley, Curtis D. "Hydrolight 3.1 User's Guide", SRI International, SRI Project Number 6583 Final Report, Office of Naval Research Contract number N00014-95-C-0238, Menlo Park, CA, 65 pages, April 1996

Morel, Andre and Bernard Gentili, "Diffuse reflectance of oceanic waters. II. Bidirectional Aspects", *Applied Optics*, Vol. 32, No. 33, pp. 6864-6879, 20 November 1993

Moon, Parry and Domina Spencer, "Illumination from a Non-Uniform Sky", *Illuminating Engineering*, Vol 37, pp 707-726, December 1942

Pegau, W.S., J.S. Cleveland, W. Doss, C.D. Kennedy, R.A. Maffione, J.L. Mueller, R. Stone, C.C. Trees, A.D. Weidemann, W.H. Wells, and J.R.V. Zaneveld, 1995. "A comparison of methods for the measurement of the absorption coefficient in natural waters", *Journal of Geophysics Research.*, Vol 100, pp. 13,201-13,220,.

Plass, Gilbert N. and George Kattawar, "Monte Carlo Calculations of Light Scattering from Clouds", *Applied Optics*, Vol. 7, No. 3, pp. 415-419, March 1968

Plass, Gilbert N. and George Kattawar, "Radiative Transfer in an Atmosphere-Ocean System", *Applied Optics*, Vol. 8, No. 2, pp. 455-466, February 1969

Preisendorfer, R. W. "*Hydrologic Optics*" in six volumes: *Volume 1: Introduction*, 218 pages, (NTIS PB-259 793/8ST); *Volume 2: Foundations*, 400 pages, (NTIS PB-259 794/6ST); *Volume 3: Solutions*, 246 pages, (NTIS PB-259 795/3ST); *Volume 4: Imbeddings*, 207 pages, (NTIS PB-259 796/1ST); *Volume 5: Properties*, 296 pages, (NTIS PB-259 797/9ST); *Volume 6: Surfaces*, 390 pages, (NTIS PB-268 704/4ST); Pacific Marine Environmental Laboratory/NOAA, Seattle, WA, via National Technical Information Services, 1976.

Preisendorfer, R. W. and C. D. Mobley, "Direct and inverse irradiance models in hydrologic optics", *Limnology and Oceanography*, Vol 29(5), pp 903-929, September, 1984.

Preisendorfer, R. W. and C. D. Mobley, "Albedos and glitter patterns of a wind roughened sea surface", *Journal of Physical Oceanography*, Vol 16(7), pp 1293-1316, July, 1986.

Quan, Xiaohong and Edward S. Fry, "Empirical equation for the index of refraction of seawater", *Applied Optics*, Vol 34, No. 18, pp 3477-3480, 20 June 1995.

Schott, John R., "*Remote Sensing The Image Chain Approach*", New York: Oxford University Press, ISBN 0-19-508726-7, 394 pages, 1997.

Schott, John R., Anthony Vodacek, Harvey Rhody, and John Waud, Verbal direction from the Dissertation Research Committee at the Proposal Presentation, Rochester Institute of Technology, Rochester, New York, October, 1998.

Selby, J.E.A. and R.A. McClatchey, "Atmospheric Transmittance from 0.25 to 28.5  $\mu\text{m}$ : Computer Code LOWTRAN 2", AFCRL-TR-72-0745, AD 763 721, Air Force Geophysics Laboratory, Hanscom AFB, MA, 1972.

Várnai, Tamás, and Roger Davies, "A Monte Carlo Model To Calculate Shortwave Radiative Transfer in Inhomogeneous Atmospheres Version 1.0", Institute of Atmospheric Physics, University of Arizona, Internal Document (*To be published*), 28 pages, January 1998

Várnai, Tamás, and Roger Davies, "Effects of cloud heterogeneities on shortwave radiation. Part II: Comparison of cloud top variability and internal heterogeneity", Institute of Atmospheric Physics, University of Arizona, Internal Document (*Submitted to the Journal of the Atmospheric Sciences*), 35 pages, March 1998

Wolfe, W. L., "Properties of optical materials", Chapter 7 in *Handbook of Optics*, W.G. Driscoll and W. Vaughan, Editors, McGraw-Hill, New York, 1978.

Wyatt, C. L. "*Radiometric Calibration: Theory and Methods*", Boston, Academic Press, 200 pages, 1978.





